

INAUGURAL - DISSERTATION

zur

Erlangung der Doktorwürde

der

Naturwissenschaftlich - Mathematischen

Gesamtfakultät

der Ruprecht - Karls - Universität

Heidelberg

vorgelegt von

Dipl.-Phys. Michael Henke

aus Wuppertal (Nordrhein - Westfalen)

Tag der mündlichen Prüfung: 25. Mai 2011

**Search for Microscopic Black Holes
in Early Data with
the ATLAS Detector at the LHC**

Gutachter: Prof. Dr. Hans-Christian Schultz-Coulon
Prof. Dr. André Schöning

Kurzfassung

Durch den Start des LHC im Jahr 2010 wurde eine neue Ära der Teilchenphysik eingeläutet. Das Standardmodell kann in bisher unerforschten Energieregionen untersucht werden. Dort eröffnen sich auch Möglichkeiten zur Entdeckung von neuer Physik. Beides sind Ziele des ATLAS-Experiments.

Diese Arbeit beschäftigt sich mit der Suche nach mikroskopischen schwarzen Löchern am LHC. Eine solche Entdeckung wäre ein eindeutiger Hinweis auf die Existenz von niederskaliger Gravitation, vorhergesagt von Theorien mit großen räumlichen Extradimensionen. Diese sind eine mögliche Lösung des Hierarchieproblems im Standardmodell. Verschiedene Suchstrategien für schwarze Löcher werden präsentiert, die für unterschiedliche Schwerpunktsenergien am LHC entwickelt wurden. Sie nutzen charakteristische Eigenschaften solcher Ereignisse zur Selektion. Vorhergesagt sind Endzustände mit hoher Masse und einer großen Anzahl von Objekten mit hohem Transversalimpuls.

Für die ersten 297 nb^{-1} an Daten, aufgezeichnet bei $\sqrt{s} = 7 \text{ TeV}$, wird eine Suche nach neuer Physik vorgestellt. Da keine Abweichungen von den Standardmodellvorhersagen gefunden wurden, kann eine obere Grenze auf den Wirkungsquerschnitt mal der Akzeptanz von $\sigma \times A < 0.46 \text{ nb}$ gesetzt werden. Da dies deutlich unter den Theorievorhersagen für Wirkungsquerschnitte liegt, welche bis zu einer Größenordnung von $\mathcal{O}(10 - 100 \text{ pb})$ reichen, ist dieses Ergebnis relevant für Modelle niederskaliger Gravitation.

Abstract

With the start of the LHC in 2010 a new era in Particle Physics has begun. In a yet unexplored kinematic regime, the Standard Model can be probed and new physics can be discovered with the ATLAS detector.

In this work the search for microscopic black holes at the LHC is presented. Their discovery would unveil the existence of large extra dimensions. Theories of such, establishing low-scale gravity, address problems of the Standard Model like the hierarchy problem. Different search strategies are discussed, which are aimed at an early discovery with the centre-of-mass energies provided by the LHC. They exploit key features of the decay of black holes, namely high mass final states with a large multiplicity of objects with high p_T .

With the first 297 nb^{-1} of $\sqrt{s} = 7 \text{ TeV}$ data, a search for such new physics is conducted. No deviations from Standard Model predictions are found, and consequently a limit on the cross section times acceptance of $\sigma \times A < 0.46 \text{ nb}$ at 95% CL is set. Theory predictions for the cross section are of the order $\mathcal{O}(10 - 100 \text{ pb})$, hence this result has an impact on theories of low-scale gravity.

Contents

1. Introduction	9
2. Standard Model and Beyond	11
2.1. The Standard Model of Particle Physics	11
2.2. Physics beyond the Standard Model	12
2.2.1. ADD Model	14
2.2.2. Extra Dimensions and Black Holes	18
2.2.3. Semi-classical Black Holes	21
2.2.4. Decay of Black Holes	21
3. LHC and ATLAS	25
3.1. Large Hadron Collider	25
3.2. ATLAS Detector	26
3.2.1. Magnet System	29
3.2.2. Inner Detector	30
3.2.3. Calorimetry	32
3.2.4. Muon System	34
3.2.5. Trigger	35
3.2.6. Luminosity Measurement	37
3.3. Reconstruction and Performance with Early Data	37
3.3.1. Jets	38
3.3.2. Electrons and Photons	40
3.3.3. Muons	42
3.3.4. Missing Transverse Energy	43
3.3.5. Trigger	44
3.3.6. Luminosity	48
3.4. Monte Carlo Simulation	48
3.5. BlackMax	49
4. Search Strategies	55
4.1. Signal Properties	55
4.2. Selection Strategies with Leptons	55
4.3. 5-Object Selection Strategy	60
4.4. Adaptation for $\sqrt{s} = 7$ TeV	69
4.5. Summary	76
5. Search for Multi-Object Final States	77
5.1. Early Data Taking in 2010	77

5.2. Signal and Backgrounds	78
5.3. Search Strategy	79
5.4. Kinematic Properties	84
5.5. Systematic Studies	85
5.6. Results	97
5.7. Acceptance	99
5.8. Summary	102
6. Conclusion and Outlook	109
A. Production of a Black Hole	111
B. Blackmax Parameters	113

1. Introduction

The history of mankind shows that new technologies and curious men are able to disturb the comforting feeling of basically having understood the foundations of the world. The invention of the telescope in 1608 allowed soon afterwards interesting findings by Galileo Galilei, which despite strong pressure from church finally led to a change from a geocentric to a heliocentric view of our planetary system. This is only one example of many in the history of science which should encourage people to use new technology and to probe the validity of our understanding.

The world of a high energy particle physicist is soundly based on the Standard Model of particle physics. This theory as elaborated in Chapter 2 describes three of the four fundamental forces in a very successful way. Until now no convincing experimental evidence has been found disturbing this picture. Partly due to its 18 free parameters and its intrinsic flexibility the theory is able to accommodate effects like CP violation. The Higgs mechanism can provide masses to particles. The still to be discovered Higgs boson seems to be the one missing piece in the particle zoo and is searched for by past and existing particle collider experiments. Nevertheless scientists are confident to find it and strongly believe in the Standard Model.

But there are already small holes and cracks in the foundations which lead to a slight discomfort and give room for new ideas. The fourth fundamental interaction, gravity, is difficult to implement into Standard Model theories. The big scale difference of the electroweak and gravitational interaction raises the so called hierarchy problem. Connected to this is the problem of fine tuning to give the Higgs boson the light mass as favoured by most theorists and present experimental data. These are no reasons for a serious breakdown of the model, but open room for new ideas.

In November 2009 the world's largest machine, the Large Hadron Collider (LHC) at CERN, started its operation and since March 2010 it is collecting data with world record breaking centre-of-mass energies and unprecedented instantaneous luminosities. It is a synchrotron accelerator based in an underground tunnel with a circumference of 27 km. Running at design parameters it will provide proton-proton collisions with $\sqrt{s} = 14$ TeV at a peak luminosity of $10^{34} \text{ cm}^{-2} \text{ s}^{-1}$. As a safety measure the centre-of-mass energy was lowered to 7 TeV for the data taking period in 2010/2011. Nevertheless this allows particle physicists to work in a yet unexplored energy regime with high statistics to look for undiscovered phenomena.

The ATLAS experiment is the largest detector at the LHC with a big collaboration of scientists. As one of the four major experiments at the LHC, it is a general purpose detector. The design goals are the search for the Higgs boson and different kinds of new physics scenarios like supersymmetry and, of special interest for this work, signs of low-scale gravity. For this the detector comprises an efficient tracking system, highly granular electromagnetic and hadronic calorimeters enclosed by a muon system with a dedicated air toroidal magnet system. Details on both the LHC and the detector can be found in Chapter 3. The detector

is operated and used by the ATLAS collaboration involving more than 3000 scientists and engineers from 174 institutions.

With impressive technology and eager scientists new physics scenarios can be probed. Problems like the hierarchy problem are addressed by theories with large spatial extra dimensions. One popular concept is the ADD model, described in detail in Chapter 2. First published in 1998 these theories predict a strong rise of the gravitational force at small distances. Closing the gap between the scales of gravity and the other forces would naturally solve the hierarchy problem.

These interesting models allow for surprising phenomena with fascinating properties. Once gravity becomes comparable with the other fundamental forces on the length scales accessible with particle colliders, gravitational effects are expected. One very prominent signal is the production of black holes in particle collisions. They are produced instantly if two partons come closer than the corresponding event horizon. If this horizon is sufficiently large due to low-scale gravity, high cross sections are expected. The decay is dominated by Hawking radiation. The democratic distribution of decay products according to their degrees of freedom is a key feature for such a signal.

Black holes would show up as spectacular signatures at the LHC. Due to its generation at high masses and its unique way of decaying via Hawking radiation the reconstruction of such an event should strongly deviate from standard QCD processes. With Monte Carlo simulations describing the production and decay of such final states it is possible to study these properties. The prediction shows a high multiplicity of particles with high transverse momenta. In Chapter 4 a possible search strategy is presented which exploits these features. The significance of the method as well as the expected required integrated luminosity is estimated for different scenarios.

With the early data of the LHC a first search for signs of new physics beyond the Standard Model is conducted. As described in Chapter 5 a dataset recorded with $\sqrt{s} = 7$ TeV and an integrated luminosity of $\mathcal{L} = 297 \text{ nb}^{-1}$ is used. In the absence of a reliable signal physics model for the energy regime accessible with these statistics the analysis aims at a very inclusive signature. The selection criteria for the signal region are at least 3 objects, a scalar sum of transverse momenta of $\Sigma p_{\text{T}} = 700$ GeV and an invariant mass larger than $M_{\text{inv}} = 800$ GeV. The number of events in the signal region can be compared with the prediction from Standard Model background processes. An extensive study of influences from detector understanding and Standard Model uncertainties is performed. The data quality and the uncertainties of the background expectations is conducted. Using a Bayesian approach a limit on the cross section times acceptance for signal models is derived, with an impact especially on theories of low scale gravity.

The history of mankind shows that it is in times like these when new technology and curious searchers open up a whole new world, so don't get too comfortable in the already established world of high energy particle physics.

2. Standard Model and Beyond

2.1. The Standard Model of Particle Physics

The Standard Model of Particle Physics (SM) is a successful theory developed in the second half of the 20th century. It describes the properties and interactions of fundamental particles in a coherent way down to the smallest probed scales ($\mathcal{O}(10^{-18}$ m)) and up to energies of $\mathcal{O}(200$ GeV). Only a short introduction is given in this chapter, a comprehensive overview can be found elsewhere [1].

It is a quantum gauge theory based on the gauge symmetry $SU(3)_C \otimes SU(2)_L \otimes SU(1)_Y$, where C denotes color charge, L the weak isospin and Y the weak hypercharge. It describes the interactions of point-like particles with half-integer spin, called *fermions*¹. The interactions are mediated by integer spin gauge *bosons*².

The Standard Model contains two types of fermions, so called *leptons* and *quarks*. Both can be organised in three families. Leptons interact by the electroweak force only. There are three particles carrying an electric charge of $(-1q)$ ³, called *electron* (e), *muon* (μ) and *tau* (τ), and three corresponding electrically neutral particles, the *neutrinos* (ν_e, ν_μ, ν_τ). Quarks additionally carry *colour* charge, to which the strong force couples. There are three quarks with electric charge $(+2/3q)$, namely the *up* (u), *charm* (c), *top* (t) quark, and three with electric charge $(-1/3q)$, called *down* (d), *strange* (s), *bottom* (b) quark. Only leptons and quarks of the first family (e, ν_e, u, d) are found in ordinary matter. Table 2.1 summarises the properties of the fermions.

Fermions				Q	Interaction
Quarks	u	c	t	$+2/3$	em, weak, strong
	d	s	b	$-1/3$	em, weak, strong
Leptons	ν_e	ν_μ	ν_τ	0	weak
	e^-	μ^-	τ^-	-1	em, weak

Table 2.1.: Fermions in the Standard Model with electromagnetic charge Q in units of the elementary charge and their interaction capabilities.

There are four fundamental interactions between the particles of the SM, *electromagnetism*, *weak* force, *strong* force and *gravitation*, mediated by five boson types. The first three are incorporated in the Standard Model. The electromagnetic force couples to electric

¹Fermions obey Fermi-Dirac statistics

²Bosons obey Bose-Einstein statistics

³ q is the charge of the elementary electron

Bosons	Mass	Interaction	Effective Coupling	Range
Photon (γ)	-	electromagnetic (em)	1/137	∞
W bosons (W^\pm) Z boson (Z)	80.4 GeV 91.2 GeV	weak	10^{-5}	10^{-18} m
Gluons (g_i)	-	strong	1	10^{-15} m
Higgs (H^0)	> 114.4 GeV	Higgs mechanism		
Graviton (G)	-	gravitational	10^{-39}	∞

Table 2.2.: Bosons in the Standard Model with their masses [2], type of interaction, coupling strength and approx. range.

charge and is mediated by the massless *photon* (γ). The theoretical approach to electromagnetism is the quantum electrodynamics theory (QED). Since the photon is massless, the electromagnetic force has infinite range, and its strength is proportional to r^{-2} . The weak force is mediated by W and Z bosons and couples to the weak hypercharge carried by all fermions. It is responsible for radioactive decays. Since the weak gauge bosons are very massive ($m_W \approx 80$ GeV and $m_Z \approx 91$ GeV), its strength is reduced and its range is very limited to $\mathcal{O}(10^{-16} - 10^{-17}$ m). The weak force is unified with electromagnetism in the electroweak theory (EW).

The strong force is described by the quantum chromodynamics theory (QCD). It couples to color charge and is mediated by gluons. The strong force is responsible for the formation of *hadrons*, which can be divided into *baryons* (qqq) and *mesons* ($q\bar{q}$). Since gluons also carry color charge themselves, they are the only gauge bosons with self-coupling. On very short distances the coupling is small and thus quarks and gluons behave as quasi-free particles within a hadron (asymptotic freedom). But the self-coupling of gluons leads to an increase of the strong coupling constant α_s on large distances, and thus the so called color confinement. It reduces the range of the strong force to a range of $\mathcal{O}(10^{-15}$ m). The color connection and the increase of the force strength on larger distances forbids the existence of free quarks or gluons outside a hadron. A high momentum quark or gluon can produce a whole set of additional hadrons, which develop as a shower and are called *jets*.

Gravitational interactions are not incorporated into the Standard Model due to the lack of a consistent theory of quantum gravity. It is much weaker than the other forces, has an infinite range and is proportional to r^{-2} . Therefore its hypothetical force mediator, the *graviton* (G) has to be massless. The gravitational force and its impact on fundamental particles will be discussed later in more detail. The fundamental properties of the bosons and the corresponding forces are summarised in Table 2.2.

2.2. Physics beyond the Standard Model

The Standard Model is extremely successful in describing the data from modern particle physics experiments. However, there are remaining open questions. They support the exis-

tence of physics beyond the Standard Model. An incomplete list of such questions is:

- Why are there three families of leptons and quarks?
- Why are the differences in mass between the families so large?
- Is there an unification of all forces?
- Can gravity be incorporated into the theory?
- Why are the strengths of the fundamental forces so different, reaching over many orders of magnitude?

In the following the focus will be on the last two points. Gravity becomes comparably strong to the other fundamental forces at the *Planck scale*, $M_{\text{Pl}} = G_{\text{N}}^{-0.5} \approx 1.3 \times 10^{-19} \text{ GeV}$, with G_{N} representing Newton's gravitational constant. The distance to the electroweak scale ($\mathcal{O}(100 \text{ GeV})$) is significant. This is called the *Hierarchy problem*. It seems unnatural that there is no bridging theory between these two scales. From the influence of the Planck scale on the Higgs boson mass arises a parallel problem. The observable Higgs mass $M_{\text{H}_{\text{obs}}}$ is composed from a bare mass (M_{H_0}) and radiative corrections (ΔM_{H}).

$$M_{\text{H}_{\text{obs}}} = M_{\text{H}_0} + \Delta M_{\text{H}}$$

The coupling of a fermion to the Higgs field is given by the Yukawa coupling λ_f . Radiative corrections to the bare Higgs mass result from higher order loop corrections. They can be written as

$$\Delta M_{\text{H}} = -\frac{|\lambda_f|^2}{8\pi^2} \Lambda_{\text{UV}}^2 + \dots, \quad (2.1)$$

where Λ is the ultraviolet cut-off scale, up to which the Standard Model is trusted to be valid. Assuming an observable Higgs boson mass of $\mathcal{O}(100 \text{ GeV})$ and no new physics up to the Planck scale, i.e. $\Lambda_{\text{UV}} \approx M_{\text{Pl}}$, the radiative corrections are very large compared to the observable mass. Therefore the bare mass has to be extremely *fine-tuned* to the radiative corrections to result in a mass of $\mathcal{O}(100 \text{ GeV})$. Although not impossible, the extreme fine-tuning seems to be unnatural. Attempts to avoid it motivate ideas of physics beyond the SM close to the EM scale.

Both the hierarchy and the fine-tuning problem are addressed by different concepts. One popular theory is *Supersymmetry* (SUSY), which aims to solve the issues of the Standard Model. Every fermionic SM particle has a bosonic supersymmetric partner and vice versa. The scalar partners of the Standard Model fermions produce radiative corrections, which cancel with the fermionic corrections due to different spin statistics for fermions and bosons. This may resolve the fine-tuning problem. Supersymmetry is not further covered in this work. For a detailed description comprehensive reviews of SUSY are available [3].

In this work concepts based on the existence of spatial extra dimensions are investigated. The idea was first brought forward in 1914, when Nordström published a paper on the possibility of unifying the Einstein equations for gravity and the Maxwell equations for electromagnetism in a five dimensional space-time [4]. After the introduction of general

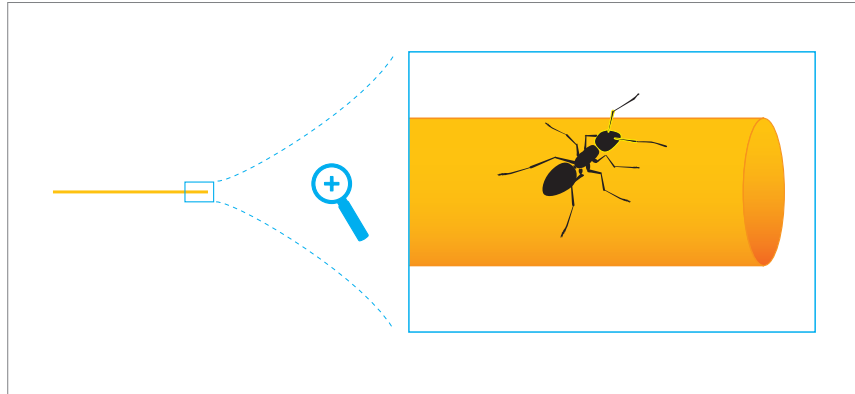


Figure 2.1.: Illustration of a compactified dimension. The one dimensional object on the left becomes two dimensional on distances in the order of the compactification radius.

relativity by Einstein, the idea was revived by Kaluza in 1921, who proposed to extend general relativity to the five-dimensional space-time [5]. Five years later, Klein supported the concept by explaining the mechanism with a fourth space dimension which must be compactified on a very small circle of the size of the Planck length ($\mathcal{O}(10^{-35} \text{ m})$) [6]. The combination of these concepts is called Kaluza-Klein theory. This was the first introduction of the idea of extra dimensions, which later on allowed e.g. the development of string theory.

The principle of compactification is illustrated in Figure 2.1. An one dimensional object becomes higher dimensional for objects with a size in the order of the compactification radius. Due to the small and inaccessible scale of compactification, the original theory made no prediction, which could be tested with experimental data. Therefore it was ignored for a long time period. This changed with the introduction of the concept of large compactified extra dimensions, as in e.g. the ADD model.

2.2.1. ADD Model

The ADD model was formulated in 1998 by Arkani-Hamed, Dimopoulos and Dvali [7, 8]. It addresses the hierarchy problem by postulating large compactified extra dimensions, which are only accessible for the mediators of gravity. A schematic view of this concept is shown in Figure 2.2. The Standard Model particles, represented by green balls, are confined on the SM brane (green volume), our four dimensional world. Only gravitons (blue balls) can propagate in the whole bulk (green+blue volume), including the extra dimensions.

This concept is consistent with a picture from string theory. SM particles are represented by open strings and must be attached to a brane, while gravitons as spin-2 particles are closed strings and thus can propagate freely. In a world with n extra dimensions, the additional available volume for gravity leads to a much lower $(n + 4)$ dimensional fundamental Planck scale, and thus to a higher strength of gravity. The fundamental energy scale associated with quantum gravity is allowed to be in the TeV range, in the same order as the electroweak scale.

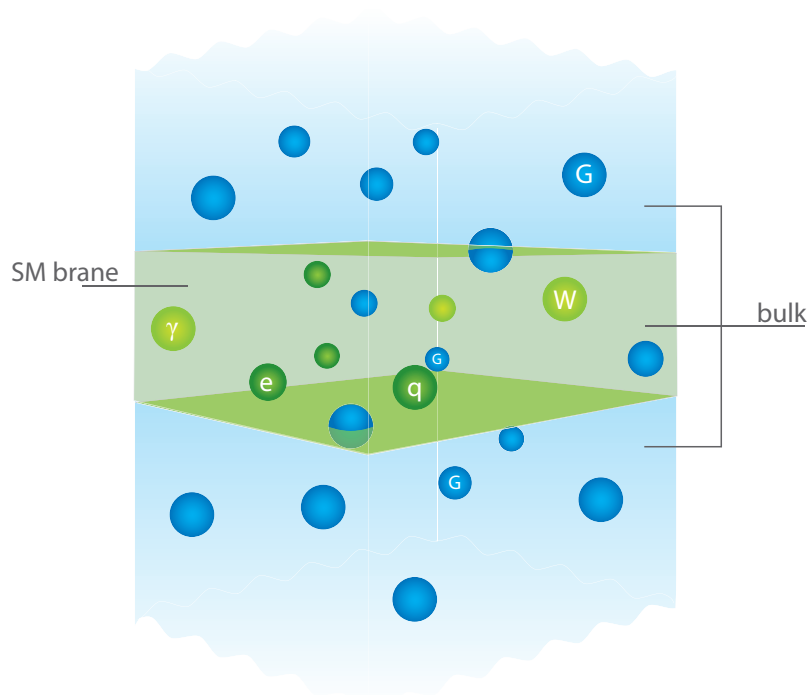


Figure 2.2.: Schematic view of the ADD model. Standard Model particles (green) are confined to the SM brane (green volume), while gravity, mediated by gravitons (blue), is allowed to propagate to the bulk (green+blue volume).

In three space dimensions, two test masses m_1 and m_2 placed at a distance r are subject to a gravitational potential dictated by Gauss' law:

$$V(r) \sim -G_N \frac{m_1 m_2}{r}, \quad (2.2)$$

where G_N is Newton's constant in four dimensions. If there are n extra dimensions, and thus a D dimensional space time ($D = n + 4$), the gravitational potential changes, if the distance r is smaller than the radius R of the compactified extra dimensions. For simplicity it is assumed that all extra dimensions have the same compactification radius, which is not a necessary requirement. In the simplest compactification form, a torus, the additional volume factor from extra dimensions is $(2\pi R)^n$. Following Gauss' law, the gravitational potential is in this case modified to

$$V(r) \sim -G_D \frac{m_1 m_2}{r^{n+1}} \quad (r < R). \quad (2.3)$$

Here G_D is Newton's constant in D dimensions. From Eq. (2.3) it is clear that for small values of the distance r the absolute value of the potential with n extra dimensions grows much faster compared to four dimensions.

The fundamental Planck scale M_D is defined in the literature in several different ways. This work uses the *Particle Data Group* (PDG) definition, first formulated in [9]:

$$M_D^{n+2} = \frac{(2\pi)^n}{8\pi G_D} \quad (2.4)$$

Other commonly used definitions are by Giddings and Thomas [10]: $M_{GT}^{n+2} = (2\pi)^n / (4\pi G_D)$ and by Dimopoulos and Landsberg [11]: $M_{DL}^{n+2} = G_D^{-1}$.

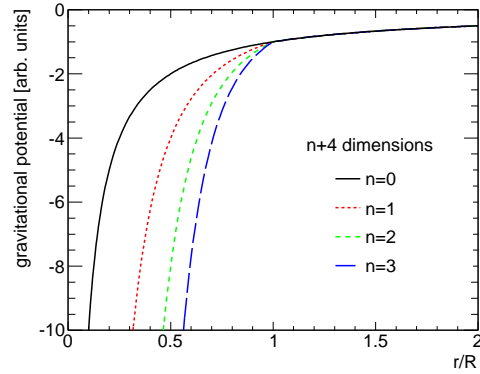
For a continuous transition from equation (2.2) to (2.3) at $r = R$ the following relation between M_{Pl} and M_D can be derived:

$$M_{Pl}^2 = 8\pi R^n M_D^{n+2}. \quad (2.5)$$

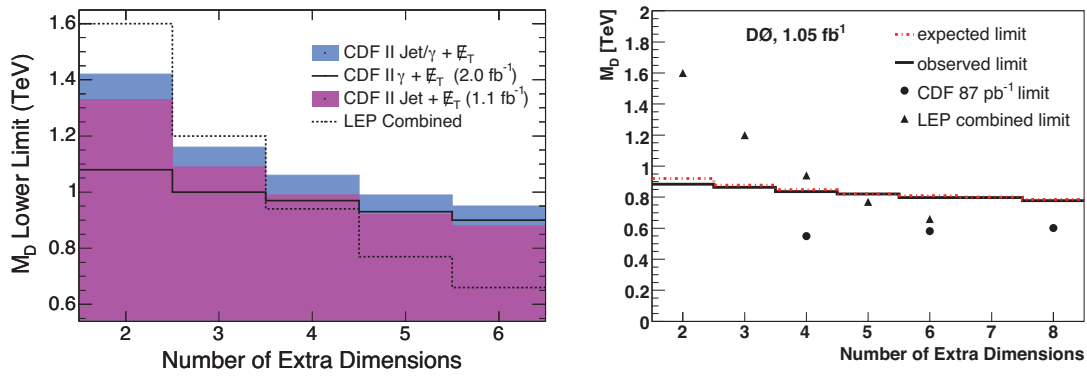
Figure 2.3 shows the gravitational potential for four dimensional space-time and with n extra dimensions. The steeper behaviour for higher n and $r/R < 1$ illustrates the faster growth of the gravitational force for small distances in a world with extra dimensions.

The compactification radii for different number of extra dimensions, which are listed in Table 2.3, can be calculated using Eq. (2.5). Since the radius for $n = 1$ with $R = \mathcal{O}(10^{12} \text{ m})$ is of the order of the size of our solar system, this case can clearly be excluded. Any alteration of the gravitational force on this distance scale would have been observed a long time ago. The radii for all other numbers of extra dimensions are in a range which was not excluded at the time of publication of the ADD model. Precision measurements of the gravitational interaction can test the model. If a deviation from the three-dimensional gravitational law is found on small distance scales, this could suggest the existence of extra dimensions. Experiments with a *torsion-pendulum* have measured the gravitational force in the sub-millimetre range without any deviation from the predictions. A limit for $n = 2$ is set at $R < 37 \mu\text{m}$, $M_D > 3.6 \text{ TeV}$ at 95% CL [12].

The direct search for *Kaluza-Klein (KK) gravitons* is another way to study large extra dimensions at a high-energy collider experiment. A massless graviton in $n+4$ dimensions with

Figure 2.3.: Gravitational potential for $n + 4$ dimensions in the ADD model.

n	R [m]
1	1×10^{12}
2	5×10^{-4}
3	4×10^{-9}
4	1×10^{-11}
5	3×10^{-13}
6	3×10^{-14}
7	5×10^{-15}

Table 2.3.: Compactification radii R for different number n of extra dimensions and a fundamental Planck scale $M_D = 1$ TeV.Figure 2.4.: Current limits on M_D as a function of the number of extra dimensions from the two Tevatron experiments CDF [13] (left) and DØ [14] (right).

n	M_D^{\min} [TeV]	experiment
2	1.60	LEP
3	1.20	LEP
4	1.04	CDF
5	0.98	CDF
6	0.94	CDF
7	0.80	DØ
8	0.78	DØ

Table 2.4.: Current best limits on M_D [TeV] at 95 % CL from LEP and Tevatron experiments [15, 13, 14].

momentum into the bulk would manifest itself as massive state in four dimensions. Due to the compactification a series of excitations should be visible, called KK gravitons. Since gravitons only interact gravitationally, they are hardly detectable in the detector and thus would be visible as missing energy. A search for direct production of gravitons was conducted at LEP in electron-positron collisions in the signature $e^+e^- \rightarrow \gamma/Z + \text{missing energy}$ [15]. Another signature searched for is the virtual graviton exchange in the $e^+e^- \rightarrow \gamma\gamma$ signature [15]. Since in proton-antiproton collisions the momentum of the colliding partons along the beam axis is unknown, only the transverse missing energy E_T^{miss} can be evaluated. The Tevatron experiments CDF and DØ searched for KK gravitons in $p\bar{p} \rightarrow \text{jet} + E_T^{\text{miss}}$ and $p\bar{p} \rightarrow \gamma + E_T^{\text{miss}}$ signatures [13, 14]. There are no signal events found in any of the searches, so limits on M_D are set. The current best limits at 95 % CL from all particle collider experiments are shown in Figure 2.4 for CDF (a) and DØ (b) and summarised in Table 2.4. They range from $M_D > 1.60 - 0.78$ TeV for $n = 2, \dots, 8$ extra dimensions.

Also astrophysics experiments search for signs of large extra dimensions. If KK gravitons existed, they would carry a significant amount of energy in supernovae explosions. This would change the energy spectrum [16]. Radiative decays of this graviton flux should be visible as diffuse cosmic γ -ray background [17]. KK gravitons could be retained in a halo around a neutron star formed by a supernova. Their decay into photons should be measurable [18]. The strongest bounds on M_D come from the halo search. The limit is M_D [TeV] $> 1760, 76.8, 9.43, 2.12, 0.67, 0.29$ for $n = 2, \dots, 7$ respectively [18].

Another possible signal from large extra dimensions should be visible in the atmosphere. Black holes could be produced by the interaction of highly energetic neutrinos with nuclei from the atmosphere. The decay of the black hole should initiate quasi-horizontal showers. The lack of observed events results in limits on $M_D > 1.0 - 1.4$ TeV for $n \geq 5$ [19].

2.2.2. Extra Dimensions and Black Holes

One of the most striking effects of gravity are the existence of black holes. Known from astrophysics, they theoretically can also be formed in a particle collision. The formation of a black hole in a two particle collision is illustrated in Figure 2.5. Two colliding particles with impact parameter b form an event horizon with radius r_h according to their centre-of-mass energy. If b is smaller than twice the event horizon radius r_h , a black hole will form (d).

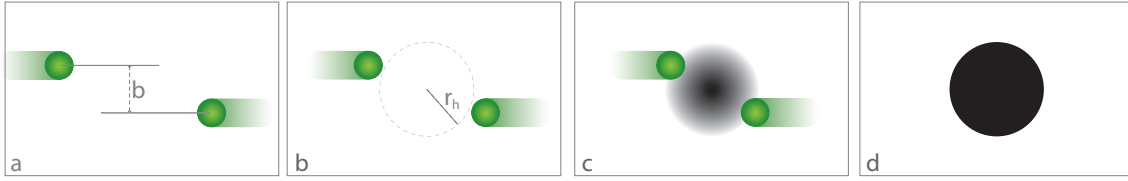


Figure 2.5.: Illustration of a black hole formation in a two particle collision.

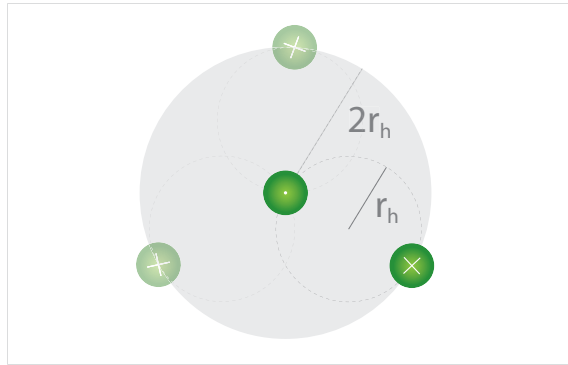


Figure 2.6.: Illustration of the cross section for black hole production in a two particle collision.

The cross section of such a collision is simply that of a black disk with radius $2r_h$:

$$\sigma = \pi(2r_h)^2. \quad (2.6)$$

This can be derived from Figure 2.6. The radius of the area perpendicular to the flight direction, centred around one particle (\odot), is twice the event horizon radius from the perspective of the other particle (\otimes). If the second particle traverses this area, a black hole is formed.

If the effective Planck scale M_{Pl} is the only fundamental scale for gravity, then the event horizon is given by:

$$r_h \propto \frac{1}{M_{\text{Pl}}} \frac{M_{\text{BH}}}{M_{\text{Pl}}}. \quad (2.7)$$

The black hole mass M_{BH} is determined by the centre-of-mass energy of the two colliding particles. For $M_{\text{BH}} = \mathcal{O}(1 \text{ TeV})$, the event horizon is $\mathcal{O}(10^{-35} \text{ m})$, the scale of the Planck length. This results in a cross section of $\mathcal{O}(10^{-41} \text{ b})$, which is many orders of magnitude too small to be accessible by any earthbound particle collider.

However, if there exist extra dimensions like proposed in the ADD model, and their compactification radius is large enough to influence gravity on the distance of fundamental particles, the event horizon can be written as [20]

$$r_h \propto \frac{1}{M_{\text{D}}} \left(\frac{M_{\text{BH}}}{M_{\text{D}}} \right)^{\frac{1}{n+1}}. \quad (2.8)$$

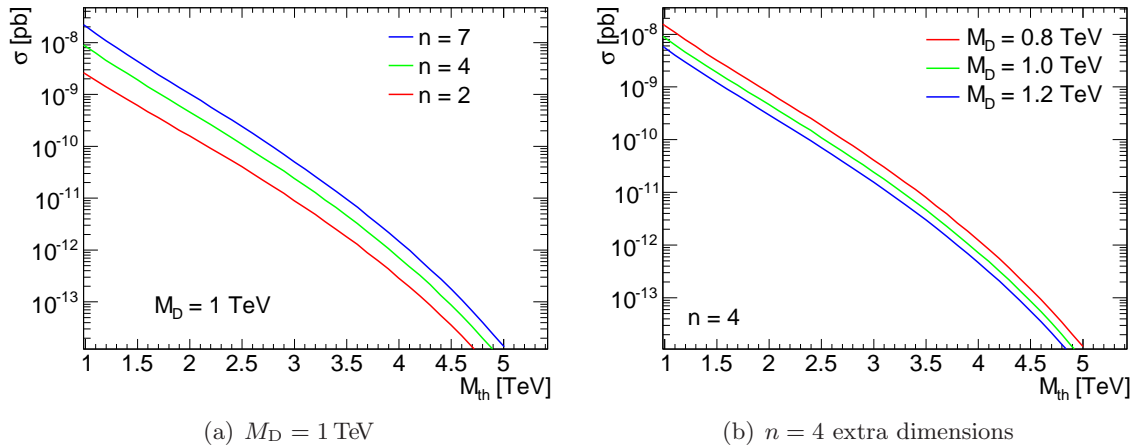


Figure 2.7.: Production cross section for microscopic black holes at $\sqrt{s} = 7$ TeV for different numbers n of extra dimensions (a) and different values for the fundamental Planck scale M_D (b).

In this case, for $M_D \sim M_{\text{BH}} \sim \mathcal{O}(1 \text{ TeV})$, the cross section is $\mathcal{O}(100 \text{ pb})$. This cross section is large enough to create the possibility of the formation of black holes at a particle collider like the LHC.

The cross section σ for the production of rotating black holes depending on the Schwarzschild radius r_s and the number n of extra dimensions can be calculated from the metric. This is shown in Appendix A. Here the result is given:

$$\sigma = 4\pi r_h^2 = 4\pi r_s^2 \left[1 + \left(\frac{n+2}{2} \right)^2 \right]^{-\frac{2}{n+1}}. \quad (2.9)$$

At the LHC the colliding particles are partons of protons, that is quarks and gluons. To calculate a differential cross section, the *parton distribution functions* (PDFs) inside the proton have to be considered. The differential cross section $\frac{d\sigma}{dM_{\text{BH}}}$ is given as

$$\frac{d\sigma(pp \rightarrow \text{BH} + X)}{dM_{\text{BH}}} = \frac{dL}{dM_{\text{BH}}} \hat{\sigma}(ab \rightarrow \text{BH}) \Big|_{\sqrt{s}=M_{\text{BH}}}, \quad (2.10)$$

where $\hat{\sigma}$ are the partial cross sections of partons a, b to form a black hole and dL/dM_{BH} is the parton luminosity. It is defined as the sum over all parton possibilities. With the parton distribution function $f_i(x_i)$, depending on Bjorken x , the parton luminosity can be written as [21]

$$\frac{dL}{dM_{\text{BH}}} = \frac{2M_{\text{BH}}}{s} \sum_{a,b} \int_{M_{\text{BH}}/s}^1 \frac{dx_a}{x_a} f_a(x_a) f_b\left(\frac{M_{\text{BH}}^2}{sx_a}\right). \quad (2.11)$$

Black holes form with a continuous mass spectrum. The initial mass is only dependent on the centre-of-mass energy of the two partons. To ensure that black holes behave and especially decay semi-classically, as described in Section 2.2.4, the requirement of a minimum

threshold mass $M_{\text{th}}(n, M_{\text{D}})$ is necessary. Possible criteria for a semi-classical regime are explained in Section 2.2.3. Figure 2.7 shows the production cross section at $\sqrt{s} = 7 \text{ TeV}$ of rotating black holes for different numbers n (a) of extra dimensions and different values for the fundamental Planck scale M_{D} (b) as a function of the threshold mass M_{th} . Models with a higher number of extra dimensions predict a higher BH production cross section for identical M_{D} and M_{th} . A higher fundamental Planck mass M_{D} leads to a lower production cross section. Requiring a higher threshold mass M_{th} also results in a decreased cross section. A typical cross section for a black hole threshold mass of $M_{\text{th}} = 3 \text{ TeV}$ is $\mathcal{O}(10 \text{ pb})$, allowing for a possible discovery with early data of the LHC experiments.

2.2.3. Semi-classical Black Holes

Most of the black hole models in the context of low-scale gravity assume, that microscopic black holes basically obey the same mechanisms as classical black holes. In this case they are called semi-classical black holes. The necessities for black hole formation at particle colliders are subject to different studies. In the classical picture [22], the Compton wavelength λ of the black hole mass M_{BH} needs to be smaller than the Schwarzschild radius.

$$\lambda = \frac{2\pi}{E} = \frac{2\pi}{M_{\text{BH}}} < r_{\text{s}}(n, M_{\text{D}}, M_{\text{BH}}) \quad (2.12)$$

This leads to a condition for the minimum black hole mass M_{th} . For example, for $M_{\text{D}} = 1 \text{ TeV}$ the threshold mass is $M_{\text{th}} = 4.26 \text{ TeV}$ (2.08 TeV) for $n = 2$ (7) extra dimensions.

Other studies focus on a different assumption: A black hole must be thermal to evaporate via Hawking radiation (see Section 2.2.4).

Therefore different requirements can be formulated:

- The entropy of the black hole should be large [23]. The entropy S of a black hole is defined as [24]:

$$S = \frac{4\pi M_{\text{BH}} r_{\text{s}}}{n+2} \gg 1 \quad (2.13)$$

- The lifetime τ of the black hole should be large compared to $1/M_{\text{BH}}$ [10]. In this case, it can be assumed that the black hole is a well defined resonance and acts as an intermediate state in the s -channel. This requires $M_{\text{th}}/M_{\text{D}} \gtrsim 1.3$ [24].

Taking all requirements it can be assumed that a threshold mass of $M_{\text{th}} = 5 \text{ TeV}$ is a safe choice for $M_{\text{D}} = 1 \text{ TeV}$ and all numbers of extra dimensions, to ensure that the produced black holes behave semi-classically.

2.2.4. Decay of Black Holes

A microscopic black hole with a mass of $\mathcal{O}(1 \text{ TeV})$ evaporates immediately. This decay can, in the semi-classical picture, be divided in three stages [25].

- Balding phase: During this phase, immediately after the formation, the black hole loses all multipole and dipole momenta via the emission of gravitons.

- Evaporation phase: This phase can be treated semi-classically, and the black hole emits particles via Hawking radiation until it reaches the fundamental Planck scale. Most of the the energy is emitted during this phase. It is the main phase to be considered in a particle collider experiment.
- Planck phase: When the black hole mass comes to the Planck scale after the evaporation phase, the decay enters the final stage. Different model approaches for this phase are explained later.

There are no well modelled theories for the first decay stage. Since in this phase only gravitons are emitted it is usually represented by an energy loss of the black hole without visible decay products. The best modelled part of the black hole decay is the evaporation phase. The energy spectrum of the particles emitted via Hawking radiation [26] is determined by the Hawking temperature T_H , defined as

$$T_H = \frac{n+1}{4\pi r_h} \quad (2.14)$$

for $n+4$ dimensions. The flux of emitted particles is given by [27]:

$$\frac{d^2 N}{dt d\omega} = \frac{1}{2\pi} \sum_{j=|h|}^{\infty} \sum_{m=-j}^j \left(\exp\left(\frac{\omega - m\Omega}{T_H}\right) + c \right)^{-1} \Gamma_{(h,j,m,\omega)}^{(n)}(\omega, a_*), \quad (2.15)$$

where ω is the energy of the emitted particle, h the helicity, and Ω the horizon angular velocity. The angular velocity Ω defined as:

$$\Omega = \frac{a_*}{(1+a_*^2)r_h}, \quad a_* = \frac{a}{r_h}.$$

The value c is -1 for bosons and $+1$ for fermions. The term $\left(\exp\left(\frac{\omega - m\Omega}{T_H}\right) + c\right)^{-1}$ determines the main feature, namely a higher energy for emitted particles at a higher Hawking temperature. $\Gamma_{(h,j,m,\omega)}^{(n)}$ represents the *grey body factors* [28, 29, 30, 31, 32]. These factors represent the deviation from a perfect black body radiation. They depend on e.g. properties of the extra dimensional models in a non-trivial way and are not discussed here.

The composition and ratio of different particle types is dependent on their degrees of freedom (d.o.f.), and is called *democratic decay*. As an example, the number of degrees of freedom for a quark is six due to the three colours and two spin states per particle. For different particle types of the Standard Model this is summarised in Table 2.5 Quarks and gluons dominate, but also a significant lepton fraction in the decay is expected.

Additional parameters for the scenarios of extra dimensions may also influence the production and decay of microscopic black holes. Split-branes [33] address the following problem of the ADD model: The democratic mechanism leads to the problem of possible baryon and lepton number violating decays. Especially the proton decay via a virtual black hole lowers the proton lifetime significantly. This would lead to striking bounds on the fundamental gravity scale M_D . A possible solution is a split-brane scenario [33]. In this case the thick SM brane is split into separate fermion branes. Leptons and quarks are separated on different

Particle type	number	spin	(anti-)particle	colour	d.o.f.
quarks	6	2	2	3	72
leptons	6	2	2		24
gluons	8	2	1		16
photon	1	2	1		2
Z boson	1	3	1		3
W boson	1	3	2		6
Higgs boson	1	1	1		1

Table 2.5.: Degrees of freedom (d.o.f.) of the SM particle types.

branes. Due to a reduced overlap of the wave functions a decay from a proton, situated on the quark brane, to leptons is strongly suppressed according to the separation of the branes. If this scenario is realised in nature, black holes produced in a hadron collider would also be situated on the quark brane. This would suppress the decay into leptons, altering the composition of black hole decay particles.

Brane tension λ is a characteristic brane property in string theory. It determines the vacuum energy density. Its effect on black hole production and decay is studied in Ref. [34]. The metric for rotating black holes and thus the grey body factors are not known, so only non-rotating black holes can be studied. With the deficit parameter $B \equiv 1 - \lambda(2\pi M_{\text{D}}^{n+1})^{-1}$ the radius of the event horizon changes to

$$r_{\text{h}} = \frac{r_{\text{s}}}{B^{1/3}} \quad (2.16)$$

Hence, a positive brane tension increases the horizon radius and, following Eq. (2.14), lowers the Hawking temperature and thus leads to a softer emission spectrum of particles.

The last stage of the black hole decay, close to M_{D} , is governed by quantum gravity. Lacking a consistent theory, three different possibilities for this stage are considered:

- Burst model: In this model the final stage of the black hole is a multi-body decay. Both decays into a fixed or variable number of particles are considered [35]. Usually, the democratic decay mechanism is used to determine the decay particles. Possible methods to determine the variable number of final decay particles include Poisson distributions [36] or the minimal number of particles [27].
- Boiling model: In this case the decay via Hawking radiation is continued beyond M_{D} down to a fixed threshold. Then a multi-body decay as described for the burst model is applied.
- Stable remnant model: Another possibility is that the black hole remains stable once reaching M_{D} [37, 38, 39]. The remnant does not further interact within the brane, except for gravity. It might thus be a candidate for dark matter.

The described properties of formation and decay of a black hole are implemented in Monte Carlo generators, e.g. BLACKMAX [27] and CHARYBDIS [35]. The basic principles and available parameters are described in Section 3.4.

3. LHC and ATLAS

3.1. Large Hadron Collider

The Large Hadron Collider (LHC) is built into the former LEP tunnel at the European Centre for Nuclear Research (CERN) near Geneva, Switzerland. It is an accelerator designed to bring protons to head-on-collisions at unprecedented energies. Additionally there is the possibility of a heavy-ion setup, colliding lead atoms instead of protons.

With a circumference of 27 km it accelerates two counter-rotating beams of particles. The beams are not continuous but the particles are organised in bunches. Each bunch contains up to 10^{11} particles and can be accelerated to an energy of up to 7 TeV. After the incident during the first start up period in September 2008 the maximum energy was lowered to 3.5 TeV as a safety measure. This value can be increased only after a longer shut down period of about 18 months, in which further safety updates are installed in the accelerator. This shut down is planned for 2013.

Collisions of bunches occur at four interaction points where the beam-lines cross. At these points the four major experiments are placed: The general purpose experiments ATLAS¹ and CMS² as well as the more specialised experiments ALICE³ and LHCb⁴ (see also Figure 3.1).

Superconducting magnets are important building blocks of the accelerator. The particles are kept on track by dipole magnets with a magnetic field strength of up to 8.3 T. The beam is focused and defocused by quadrupole magnets. This is needed for a stable operation of the accelerator as well as a high luminosity.

The instantaneous luminosity can be written as

$$\mathcal{L} = fn \frac{N_1 N_2}{A} \quad (3.1)$$

with f as revolution frequency, n the number of bunches in a beam, $N_{1,2}$ the number of particles in a bunch and A the cross section area of the bunches. Since the revolution frequency is fixed and the number of particles per bunch is limited, the possibilities for an increase of the luminosity are the number of bunches per beam and the width of the bunches. The number of bunch positions per beam is limited to 3564, whereof only 2808 bunches can be filled due to constraints from operation. This leaves the interaction area $A = 4\pi\sigma_x\sigma_y$ as the measure to adjust the luminosity to the needs of the experiments. The planned luminosity for the general purpose experiments ranges from $10^{31} \text{ cm}^{-2} \text{ s}^{-1}$ in the beginning to $10^{34} \text{ cm}^{-2} \text{ s}^{-1}$ in the high luminosity phase.

¹A Toroidal LHC ApparatuS

²Compact Muon Solenoid

³A Large Ion Collider Experiment

⁴Large Hadron Collider beauty experiment

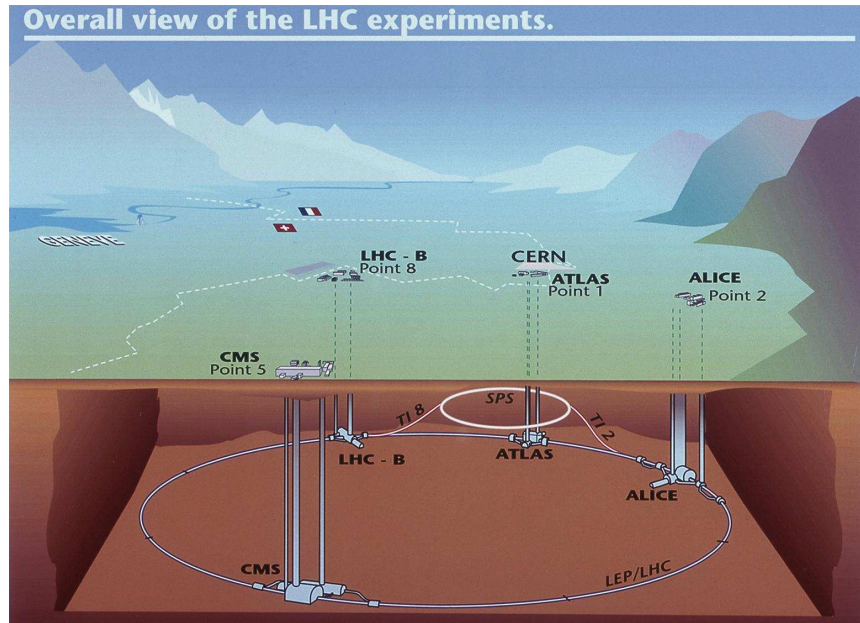


Figure 3.1.: Scheme of the LHC ring with the four main experiments [40].

Another common unit for the luminosity beside $1 \text{ cm}^{-2} \text{ s}^{-1}$ is $1 \text{ b}^{-1} \text{ s}^{-1}$, with barn being $1 \text{ b} = 10^{-28} \text{ m}^2$. This helps to calculate the integrated luminosity:

$$\mathcal{L}_{\text{int}} = \int \mathcal{L} dt \quad (3.2)$$

with the unit being 1 b^{-1} .

Thus the number N of expected events in a data sample corresponding to a certain integrated luminosity is

$$N = \sigma \mathcal{L}_{\text{int}} \quad (3.3)$$

with σ being the cross section of the involved processes. It is expected that multiple interactions per bunch crossing take place, commonly called pile-up. In the high luminosity phase with $\mathcal{L} = 10^{34} \text{ cm}^{-2} \text{ s}^{-1}$ about 23 proton proton collisions happen in one bunch crossing. But already with lower luminosities pile-up occurs, which is a demanding task for the experiments.

3.2. ATLAS Detector

The ATLAS experiment is a general purpose detector, built and operated by a collaboration of 174 institutes and more than 3000 physicists [41]. The available centre-of-mass energy of $\sqrt{s} = 7 \text{ TeV}$, and later $\sqrt{s} = 14 \text{ TeV}$, is unprecedented in an earth-bound particle accelerator and allows for a large discovery potential of such an experiment.

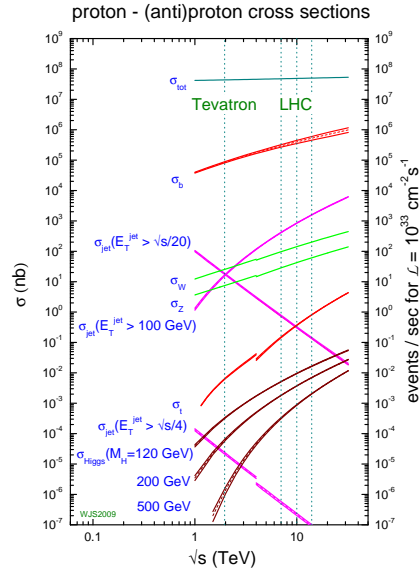


Figure 3.2.: Predictions of the total cross section (σ_{tot}) and cross sections for individual cross sections (left axis). Expected event rates per second at an instantaneous luminosity of $\mathcal{L} = 10^{33} \text{ cm}^{-2} \text{ s}^{-1}$ as a function of the centre-of-mass energy \sqrt{s} [43].

The physics program of ATLAS is very diverse, but the main objectives are [40]:

- The search for the Higgs boson. The sensitivity for the mass of a Standard Model Higgs boson extends from the LEP exclusion limit of 114.4 GeV [42] up to about 1 TeV for $\sqrt{s} = 14 \text{ TeV}$.
- Test of the validity of the Standard Model, with precision measurements of the top quark mass, b-physics and CP violation.
- Search for physics beyond the SM, in particular supersymmetry and extra dimensions.
- Study of hadronic matter under extreme conditions in lead-lead collisions, and possibly the transition to a state in which quarks and gluons are deconfined, the quark-gluon plasma.

Figure 3.2 shows the predictions of the individual and total cross section for different SM processes as a function of the centre-of-mass energy \sqrt{s} [43]. The sudden jump in some curves is due to the difference between proton-antiproton and proton-proton collisions. The expected event rate per second at an instantaneous luminosity of $\mathcal{L} = 10^{33} \text{ cm}^{-2} \text{ s}^{-1}$ is also displayed. The expected higher event rate for signal processes as Higgs production at the LHC compared to the Tevatron leads to higher statistics and a higher sensitivity. But the large gap between total cross section and e.g. the cross section for Higgs production is a big challenge for the experiment in order to identify and select the interesting processes. Due to

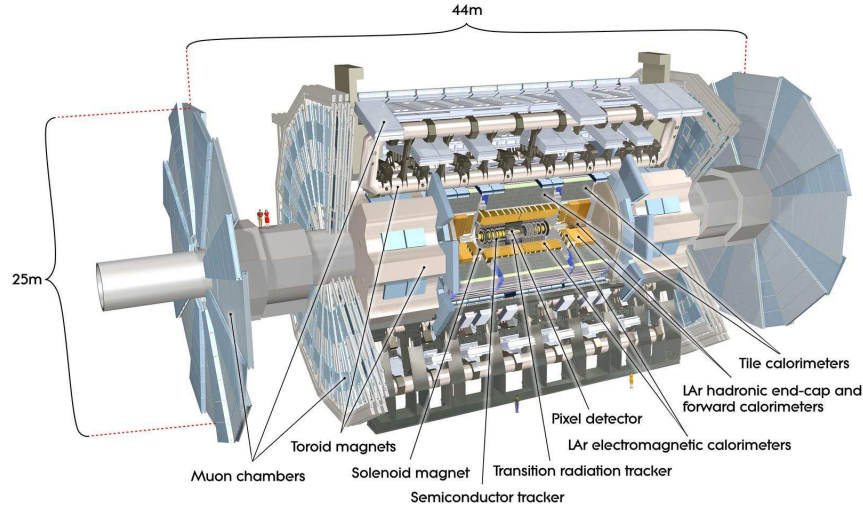


Figure 3.3.: Scheme of the ATLAS Detector [40].

the wide ranged physics goals of the experiment and the operation conditions, the challenges and design requirements, as listed below, are demanding:

- efficient track and vertex reconstruction near the interaction point to identify pile-up vertices and secondary vertices from b and τ decays.
- electromagnetic calorimetry with a high energy resolution and solid angle coverage to identify and measure electrons and photons.
- hermetic hadronic calorimetry for accurate jet measurements and determination of E_T^{miss} .
- muon system for high p_T resolution over a wide momentum range and unambiguous charge determination for high p_T muons.
- high detector granularity to handle the high particle flux and resolve overlapping events and objects.
- fast, selective and reliable trigger system to handle the high interaction rate and guarantee an efficient selection of interesting physics processes.
- radiation tolerant electronics and detector components to handle the harsh environment of a hadron collider.

Figure 3.3 shows an overview of the ATLAS detector. It has diameter of 25 m and an overall length of 46 m, weighing about 7000 t. It is constructed rotation-symmetric around the beam axis, providing full coverage for the azimuthal angle. The different components are arranged layer-wise. The central part is built in a barrel shape while the more forward detector regions are built as end-caps.

A detailed description of the detector can be found elsewhere [40]. A short summary of the different detector components crucial for this analysis is given in the following sections.

Coordinate System

The coordinate system of the ATLAS experiment is a right handed cartesian system. The x-axis is pointing to the centre of the ring, the y-axis is pointing vertically upwards, and the z-axis is oriented parallel to the beam direction⁵. The origin of the coordinate system is at the nominal interaction point at the centre of the detector. The azimuthal angle ϕ , with $0 \leq \phi < 2\pi$, is measured in the x-y plane around the beam axis. The angle $\phi = 0$ corresponds to the positive x-axis, the positive y-axis is represented by $\phi = \pi/2$. The polar angle θ is measured from the beam axis with positive z , depending on the momentum components transverse (p_T) and parallel (p_z) to the beam axis:

$$\theta = \arctan\left(\frac{p_T}{p_z}\right) \quad (3.4)$$

More useful for the physics description of an event is the rapidity y . The difference in rapidity of two particles is Lorentz invariant under a boost in z direction. It is defined as

$$y = \frac{1}{2} \ln\left(\frac{E + p_z}{E - p_z}\right) \quad (3.5)$$

To calculate the rapidity, mass and momentum of the particle must be known. A comparable measure is the pseudo-rapidity η , which is often used and defined as

$$\eta = -\ln\left[\tan\left(\frac{\theta}{2}\right)\right] \quad (3.6)$$

In the massless limit ($p \gg m$) the pseudo-rapidity closely approximates the rapidity. The transverse plane ($\theta = \pi/2$) corresponds to $\eta = 0$, while for directions close to the beam axis the pseudo-rapidity approaches infinity.

3.2.1. Magnet System

The overall size of the ATLAS detector is dominated by the magnet system. The whole system has dimensions of 26 m in length and 22 m in diameter. The generated magnetic fields are needed for momentum measurements and particle identification. A 2 T strong magnetic field for the inner detector is provided by a central solenoid. The muon system uses the field generated by a barrel toroid and two end-cap toroids with an average strength of 0.5 T and 1 T respectively.

The superconducting *solenoid* magnet [44] is built from a single-layer coil. It uses the same cryostat as the electromagnetic barrel calorimeter, thus reducing the material budget in front of the calorimeters. This helps to reduce the probability for a particle to start showering and deposit energy before the active layers of the calorimeters are reached. The solenoid is shorter compared to the inner detector for the same reason (5.8 m vs 7.2 m). This geometry

⁵the positive z-axis is pointing towards the LHCb detector

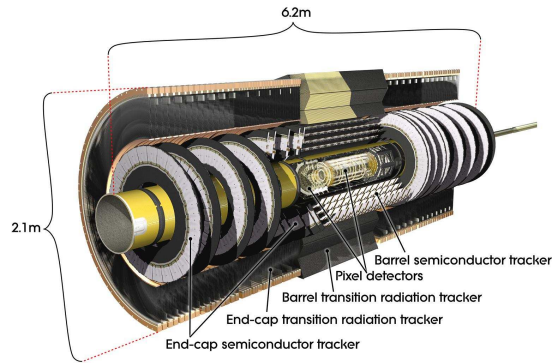


Figure 3.4.: Scheme of the ATLAS Inner Detector [40].

introduces a non-uniformity to the magnetic field, falling from 2 T at the interaction point to 0.5 T at the end of the inner detector.

The air-core *toroid* magnets [45] have an eight-fold symmetry around the beam axis and generate a magnetic field in a pseudo-rapidity range from $0 \leq |\eta| \leq 2.7$. The barrel toroid coils are contained in individual cryostats and placed in between the hadronic calorimeters and the muon spectrometer. The other toroid coils are assembled in one large cryostat per end-cap.

3.2.2. Inner Detector

The Inner Detector (ID) of ATLAS is designed to reconstruct tracks and vertices and to provide information for particle identification [46]. Using a 2 T strong axial field it is possible to reconstruct tracks with a transverse momentum of $p_T > 0.5$ GeV. Particles with a lower momentum have a too small bending radius and are therefore looping without escaping the inner detector. The Inner Detector comprises three sub detectors. Closest to the beam axis is the pixel detector, responsible for primary vertex reconstruction and determination of secondary vertices coming from long lived particles. It is followed by the Semiconductor Tracker (SCT), used for high precision pattern recognition measurements. A pseudo-rapidity range of $|\eta| < 2.5$ is covered by these two detectors. The outermost sub-detector is the Transition Radiation Tracker (TRT). Covering a pseudo-rapidity range of $|\eta| < 2.0$, it enhances the pattern recognition range and additionally provides particle identification information.

Pixel Detector

The Pixel Detector [47] is built out of 1744 semiconductor modules. Each of the modules has an area of 15.5 cm^2 and is $250 \text{ }\mu\text{m}$ thick. The nominal size of each pixel on the modules is $50 \text{ }\mu\text{m} \times 400 \text{ }\mu\text{m}$ in $\phi \times z(R)$ for the barrel (end-cap). The modules are arranged in three layers in the barrel and in three disk layers in the two end-caps. The innermost layer of the pixel detector is placed at about 5 cm around the beam axis. An intrinsic resolution of $10 \text{ }\mu\text{m}$ in the $R - \phi$ plane and $115 \text{ }\mu\text{m}$ in z direction can be achieved.

A pixel module is operated as a p-n junction in reverse bias. A charged particle traversing the detector creates electron-hole pairs. These are separated by the applied depletion voltage and transported to the surface, where they are detected by charge sensitive amplifying electronics. Each module has 46 080 readout channels, which leads to 80.4 million channels for the whole pixel detector. This represents about half the number of readout channels provided in the ATLAS detector.

Due to the proximity to the interaction point, the pixel detector is placed in a harsh environment, requiring especially a robust radiation hardness. For the innermost barrel layer a radiation dose of 500 kGy is expected after five years of LHC operation at design luminosity, which makes it necessary to replace it after this time period. The two outer layers are expected to reach this dose only after ten years.

Semiconductor Tracker

The Semiconductor Tracker (SCT) [48] is the intermediate sub-detector of the inner detector. It can provide four additional space points to a track, thus contributing to momentum, impact parameter and vertex position measurement. Due to its relatively high resolution it is also useful for pattern recognition. It is based on the same function principle as the pixel detector, but is equipped with strips instead of pixels. The single modules are build as stereo modules with two layers of strips, arranged with an angle of 40 mrad between the orientation of the layers. This provides information of the $z(R)$ position in the barrel (end-cap). The modules are installed in four concentric layers in the barrel and nine disks in both end-caps. One strip layer of each stereo module is placed parallel to the beam axis in the barrel and radially in the end-caps. This ensures a proper measurement of the ϕ coordinate. The position resolution of the SCT is 17 μm in the $R - \phi$ ($z - \phi$) plane and 580 μm in $z(R)$ for the barrel (end-cap). In total the silicon modules cover a surface of 63 m^2 and are read out via 6.3 million readout channels.

Transition Radiation Tracker

The Transition Radiation Tracker (TRT) [49] is the outermost sub-detector of the inner detector of ATLAS. It provides further space points for the track reconstruction and additionally a particle identification measure. It is built out of thin proportional drift tubes with a diameter of 4 mm. The straw tubes are filled with a xenon based gas mixture, and have a gold-plated tungsten wire in the centre as anode. As cathode serves an aluminium coating layer on the tube. As indicated by its name, the detector makes use of the transition radiation effect. A relativistic charged particle emits photons when it crosses the boundary of two materials with different dielectric constants. The radiated energy is linearly proportional to the Lorentz factor ($\gamma = E/m_0$). Thus the TRT can not only be used to determine track points of the charged particle but especially to distinguish between electrons and heavier particles. In the barrel 52 544 straw tubes are arranged in 73 layers parallel to the beam axis. In the end-caps 160 layers comprise 122 880 tubes, which are oriented radially around the beam axis. The space between successive layers is filled with polypropylene foil acting as radiator. A large number of space points per track can be expected from this detectors. The chosen geometry ensures at least 36 hits for a traversing charged particle with $p_T > 0.5$ GeV. The TRT only provides a $R - \phi$ measurement, with an intrinsic accuracy of 130 μm per straw tube.

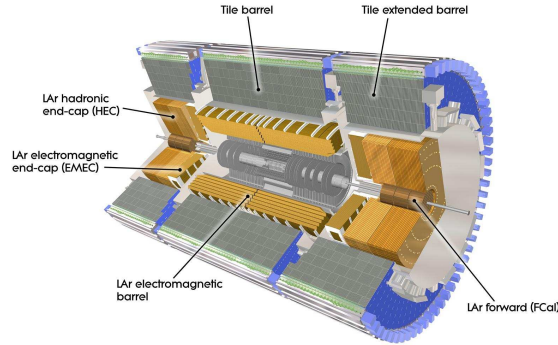


Figure 3.5.: Scheme of the ATLAS Calorimetry [40].

3.2.3. Calorimetry

The purpose of calorimetry is to provide both an energy measurement and a directional information about the measured energy deposition. Furthermore it allows the determination of missing transverse energy E_T^{miss} due to its large coverage in pseudo-rapidity while limiting so called *punch-throughs* from non-minimum ionising particles to the muon system. The calorimetry of ATLAS is divided in an electromagnetic part, dedicated to the measurement of electrons and photons, and a hadronic part, optimised for jet reconstruction and missing transverse energy measurements. The general layout of the calorimetry is shown in Figure 3.5.

Electromagnetic Calorimeter

The Electromagnetic Calorimeter (EMCalo) [50] is a non-compensating sampling calorimeter, realised as a lead-liquid argon ionisation chamber. This technology was chosen due to its good characteristics concerning electronic noise, energy resolution, radiation robustness and a possible high granularity implementation. Lead plates are used as absorbers. Their purpose is to induce the electromagnetic shower as well as to absorb shower constituents with too low energy to create new particles in the shower. The gaps between the absorber plates are filled with liquid argon (LAr) as active layer. The secondary electrons and positrons, created during shower evolution, ionise the argon atoms. The resulting ionisation signal is then collected by copper electrodes which are also situated between the absorber plates. The electrodes consist of three layers. The outer two distribute the high-voltage over the LAr gap, while the inner one collects the ionisation signal via capacitive coupling. The absorber plates and electrodes are projective to the interaction point in η direction and are bent in an accordion shape. With this design an incident particle will always traverse through both the absorber and the active material, providing maximum hermeticity for particles coming from the interaction point.

The electromagnetic calorimeter is divided into a barrel part ($|\eta| < 1.4$) and two end-caps ($1.4 < |\eta| < 3.2$). The overlap region $1.37 < |\eta| < 1.52$, also referred to as crack

region, is expected to show poorer performance due to a lack of instrumented material. The *electromagnetic barrel calorimeter* is placed around the central solenoid, inside the barrel cryostat surrounding the ID cavity. It consists of two half-barrels, divided by a thin gap of 4 mm at $z = 0$. Each half barrel is divided into 16 modules, each covering an equal slice of the full azimuthal range. In depth the modules are segmented into three regions (strip, middle, back), adding up to a thickness radiation length ranging from $22 X_0$ ($\eta = 0$) to $33 X_0$ ($|\eta| = 1.3$). The innermost layer is divided in fine strips in η direction and is important for e.g. γ/π^0 separation. The middle part is divided in squared cells with fine granularity to provide good position resolution. The largest energy fraction of an electromagnetic shower is deposited in this part. The tail of an electromagnetic shower is collected in the back layer, which also consists of cells but with a coarser granularity. The material budget a particle has to traverse before entering the electromagnetic barrel is about $2.3 X_0$ ($|\eta| = 0$) to $6 X_0$ ($|\eta| = 1.475$). In order to be able to correct for this energy loss in the inner detector, central solenoid and cryostat wall, a pre-sampler detector is placed in front of the barrel. It comprises a 11 mm thin LAr layer with 64 identical azimuthal cells. Each barrel module provides 3424 readout channels, including the corresponding pre-sampler cells.

The two *electromagnetic end-cap calorimeters* are contained within cryostats together with the hadronic end-caps and the forward calorimeters. Each end-cap comprises two co-axial wheels. The covered pseudo-rapidity range is $1.375 < |\eta| < 2.5$ ($2.5 < |\eta| < 3.2$) for the outer (inner) wheel. Each wheel is divided into eight wedge shaped modules. In the range of $1.5 < |\eta| < 2.5$ the modules are divided in three layers in depth, in the same way as for the barrel. In the other ranges they consist only out of two layers in depth with a coarser granularity. For $1.5 < |\eta| < 1.8$ a pre-sampler is implemented in front of the end-cap with two 2 mm thin LAr layers. The total active thickness of a module is larger than $24 X_0$. Together with the pre-sampler cells each module provides 3984 readout channels.

Hadronic Calorimeter

The Hadronic Calorimeter [51] covers a pseudo-rapidity range of $|\eta| < 4.9$ and uses two different techniques. The barrel region is equipped with a tile calorimeter, while the end-cap and forward regions are based on copper-liquid-argon technology. The *Tile Calorimeter* is divided in a central barrel and two extended barrels, and subdivided in 3 layer in radial depth. It uses steel as absorber and scintillating plates, referred to as tiles, as active medium. An ionising particle crossing a tile produces ultraviolet light, which is transformed to visible blue light by scintillating additives. The edges of the tile are equipped with wavelength shifting fibres, which collect the light and guide it to two photo multiplier tubes (PMTs). Several tiles are grouped to certain PMTs, forming cells with a size in $\Delta\eta \times \Delta\phi$ of 0.1×0.1 for the inner two layers and 0.2×0.1 for the outer layer. The thickness of the three layers corresponds to 1.5, 4.1 and 1.8 interaction lengths (λ_{int}) from inside to outside at $\eta = 0$. Between the central and the extended barrel is a gap of about 70 cm, mainly used for cabling and services for the sub-detectors closer to the interaction point. This only partially instrumented region is expected to perform poorer compared to the rest of the tile calorimeter. The number of readout channels for the tile calorimeter is about 10 000.

The two *Hadronic End-cap Calorimeters* use copper plates as absorbers and liquid argon as active medium. Each end-cap consists of two wheels placed concentrically around the

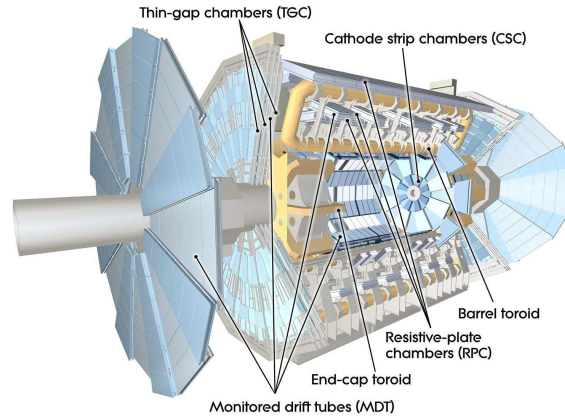


Figure 3.6.: Scheme of the ATLAS Muon System [40].

beam axis. Each wheel is constructed from 32 identical modules and is divided into two longitudinal readout segments. Each hadronic end-cap calorimeter provides 5632 readout channels and has an active part corresponding to approximately $12\lambda_{\text{int}}$.

The two *Forward Calorimeters* (FCALs) are placed at high $|\eta|$, and are therefore exposed to a high level of radiation. Each FCAL is divided into three 45 cm deep modules. The first module uses copper as absorber and is optimised for electromagnetic measurements. The outer two modules are made of tungsten and have the purpose of measuring mainly hadronic interactions. Compared to the other ATLAS liquid argon calorimeters the design is much denser. Each forward calorimeter has a depth of approximately $10\lambda_{\text{int}}$ and provides 1762 readout channels.

3.2.4. Muon System

Muons are the only detectable particles which can traverse the calorimeters. Being minimum ionising particles their momentum is determined by track measurements. For this purpose a dedicated muon system is installed outside the hadronic calorimeter. It has two functions, namely precise momentum measurement and fast trigger information. The first task is accomplished by two high precision tracking chambers, covering a pseudo-rapidity range of $|\eta| < 2.7$. For the second task dedicated trigger chambers are installed with a pseudo-rapidity coverage of $|\eta| < 2.4$.

Tracking Chambers

The *Tracking Chambers* consist of three concentric barrel layers and four end-cap disks at each side. The measurement of track coordinates is mainly performed with monitored drift tubes. The only exception are the innermost end-cap disks which are equipped with cathode strip chambers.

Monitored Drift Tubes [52] are equipped with an internal chamber alignment system, hence are called monitored. They comprise three to eight layers of 30 mm diameter aluminium tubes which are filled with an Ar-CO₂ gas mixture at 3 bar absolute pressure. A

muon traversing the gas produces ionisation charge which is collected by the central tungsten/rhenium anode wire. The achievable spatial resolution is $80\ \mu\text{m}$ per tube and $35\ \mu\text{m}$ per chamber. In total there are 1150 monitored drift chambers, providing approximately 354 000 channels.

Cathode Strip Chambers [53] are multi-wire proportional chambers with two cathodes, both segmented into strips orthogonal to the anode wire. These chambers are used in the innermost disks because of their high granularity. This is needed for the operation with high rates and background conditions in this region. They offer smaller drift times, better timing resolution, a good two-track resolution and a low neutron sensitivity. A total of 32 cathode strip chambers installed in ATLAS provide approximately 31 000 readout channels.

Trigger Chambers

The *Trigger Chambers* provide bunch crossing identification, robust and fast measurements for trigger decisions and track point information in the direction orthogonal to the tracking chambers. In the barrel region ($|\eta| < 1.05$) three layers of resistive plate chambers are used while in the end-cap region ($1.05 \leq |\eta| \leq 2.4$) the muon system is equipped with 4 layers of thin gap chambers.

Resistive Plate Chambers [53] use a thin gas gap between two parallel resistive plates as active medium. The primary ionisation electrons are multiplied in avalanches by a uniform electric field. The resulting ionisation signal is read out via capacitive coupling by metal strips on both sides of the detector. A resistive plate chamber consists of two layers, both providing η and ϕ information simultaneously. The chambers are mounted together with the monitored drift tubes. Two chambers sandwich the middle drift tube layer while the third one is located close to the outer disk. A muon traversing the barrel region will therefore create six trigger chamber signals. This helps in reducing the fake rate due to noise hits. In total the system is equipped with 606 resistive plate chambers providing 373 000 readout channels.

Thin Gap Chambers [54] are similar in design to multi-wire proportional chambers. The difference is a smaller anode wire to wire distance than the cathode to wire distance. This leads to a shorter drift time and hence a good timing resolution. The chambers are oriented such that the wires measure the R coordinate, while the ϕ coordinate is provided by radial copper strips on the back side of the cathode plates. One thin gap chamber is placed in front of and two behind the second monitored drift tube disk. A fourth chamber is placed in front of the innermost tracking layer. The end-caps comprise 3588 thin gap chambers which provide 318 000 readout channels.

3.2.5. Trigger

The purpose of the ATLAS *Trigger System* is to reduce the data rate from the produced rate ($10^9\ \text{Hz}$) at nominal running conditions to a level which is offline storable ($200\ \text{Hz}$). The challenge is to identify and keep interesting events while discarding background events all within a limited time. This problem is addressed with a three level trigger system.

The *Level-1 trigger* (L1) [55] is implemented in dedicated hardware. It uses information from an electrostatic beam pick-up (BPTX) as well as coarse detector information from the

calorimeters and muon system, but not from the inner detector. In addition multiplicity information from the minimum bias trigger system (MBTS) and the very forward detectors are taken as input. The decision of this level is based on the following signatures: jets, electrons/photons, muons, hadronic tau decays (all above well defined p_T thresholds) as well as high values of E_T^{miss} and ΣE_T . The available time for the decision is $2.5 \mu\text{s}$. Therefore no complex algorithms can be used, but only robust and fast methods like a sliding window technique. If the event is accepted, information about regions of interest (RoIs) are passed on to the high level trigger. The nominal output rate from Level 1 is $\sim 100 \text{ kHz}$.

The *High Level Trigger* comprises two trigger levels, *Level 2* (L2) and *Event Filter* (EF). Both are software based and run on a dedicated processor farm. Level 2 uses the full detector granularity including the information from the inner detector, but only for the regions of interest received from Level 1. It already works with more complex object reconstruction algorithms, leading to e.g. the possible distinction between electrons and photons. The decision taking time for Level 2 is $\sim 10 \text{ ms}$. The nominal output rate from Level 2 is $\sim 3.5 \text{ kHz}$. If the event is accepted from Level 2 the final decision is taken by the Event Filter. It has access to an event reconstruction with the full detector granularity and information. Objects are reconstructed with algorithms which are similar to offline reconstruction. The decision time is in the order of seconds, and the output rate is as required 200 Hz . A combination on L1, L2 and EF trigger item is called trigger chain. Every high level item can only be initiated by the L1 item corresponding to the trigger chain. The complete set of trigger chains is set up in the trigger menu, which can be adjusted for different running conditions and physics purposes. If a trigger chain or item is producing a higher rate than allocated it can be prescaled. In this case only every n th time an accept decision of an item is passed on to the next level. This prescale can be applied on any level.

Debug Stream

Due to the difficult task of the trigger it may happen that a decision for a certain event can not be taken. Reasons are algorithm failures or time outs in the high level triggers. Many are due to time outs in the muon system. Large signals in the muon system can be induced by cosmic showers or punch-through jets. The latter are most likely to occur for high p_T jets in the direction of the borders of different calorimeter parts, i.e. from barrel to extended barrel and from extended barrel to the end-cap. The punch-through jet creates many hits in the muon system. This signal excess in the muon system causes problems with e.g. the computing intensive muon track segment fitting. If the algorithm does not finish within 2 s , this leads to a time out error and the trigger execution is stopped.

All events for which a trigger decision can not be taken are stored in the so called *debug stream*. The trigger algorithms are run again offline for these event, and they can be analysed to see if they have importance for a certain analysis. A reinsertion of the event into the nominal physics stream is difficult and therefore not done routinely. Hence, especially for search analyses, it is very important to check the debug stream events to ensure that no interesting event is missed due to a trigger problem.

3.2.6. Luminosity Measurement

The luminosity can be determined using MBTS, the Zero-Degree Calorimeter (ZDC), the ALFA⁶ detector, and LUCID⁷ [56]. The latter is the principal luminosity monitor. It is placed around the beam pipe at $z = \pm 17$ m, measured from the nominal interaction point of ATLAS. The detector consists of Cerenkov tubes. These are aluminium tubes with a length of 1.5 m and a diameter of 15 mm. They are filled with C₄F₁₀ gas under a constant pressure of 1.1 bar. Each side consists of 20 tubes. The energy threshold for the production of Cerenkov light is 10 MeV (2.8 MeV) for electrons (pions).

LUCID is calibrated using van der Meer scans [57], which use a scan of the beam separation parameter to determine the beam size A . The number of protons is determined from the beam intensity, which is estimated by measuring the total charge of bunches. The luminosity can then be calculated using Equation (3.1).

Performance goals

The physics goals and operation requirements determine the nominal performance goals of the ATLAS detector. These are summarised in Table 3.1.

detector component	required resolution
Tracking	$\sigma_{p_T}/p_T = 0.05\% p_T \oplus 1\%$
EM calorimetry	$\sigma E/E = 10\%/\sqrt{E} \oplus 0.7\%$
Hadronic calorimetry	
barrel and end-cap	$\sigma_E/E = 50\%/\sqrt{E} \oplus 3\%$
forward	$\sigma_E/E = 100\%/\sqrt{E} \oplus 10\%$
muon spectrometer	$\sigma_{p_T}/p_T = 10\%$ at $p_T = 1$ TeV

Table 3.1.: Nominal performance goals for the ATLAS detector [40]

3.3. Reconstruction and Performance with Early Data

Definitions

In this work, the following definitions are chosen for the transverse momentum sum and invariant mass: Σp_T is defined as the scalar sum of the transverse momentum p_T for all selected reconstructed final state objects. E_T^{miss} is not included in this sum. The invariant mass M_{inv} , with p_i representing the reconstructed four momenta of all objects and E_x^{miss} and E_y^{miss} being the x and y components of E_T^{miss} , is defined as follows:

$$M_{\text{inv}} = \sqrt{p^2} \quad \text{with} \quad p = \sum_{i=\text{objects}} p_i + (E_T^{\text{miss}}, E_x^{\text{miss}}, E_y^{\text{miss}}, 0). \quad (3.7)$$

⁶Absolute Luminosity for ATLAS

⁷Luminosity measurement using Cerenkov integrating detector

Including $E_{\text{T}}^{\text{miss}}$ improves the mass resolution, since the energies of particles like neutrinos or gravitons, which otherwise escape the detector, are partially taken into account. Although called invariant mass, M_{inv} is not invariant under Lorentz transformations due to the z component of the missing energy not measurable at a hadron collider.

3.3.1. Jets

Anti- k_{\perp} Algorithm

In order to form jets as physics objects from topological calorimeter clusters [58] an algorithm is needed. Requirements are co-linear and infra-red safety. A relatively new approach is the anti- k_{\perp} jet clustering algorithm [59].

This algorithm calculates, for all input objects i , the quantities d_{ij} and d_{iB} as follows:

$$d_{ij} = \min(k_{\perp i}^{-2}, k_{\perp j}^{-2}) \frac{(\Delta R)_{ij}^2}{R^2} \quad (3.8)$$

$$d_{iB} = k_{\perp i}^{-2} \quad (3.9)$$

$$(\Delta R)_{ij}^2 = \sqrt{(y_i - y_j)^2 + (\phi_i - \phi_j)^2}$$

with $k_{\perp i}$ being the transverse momentum of object i and y_i its rapidity. The quantities d_{ij} and d_{iB} can be seen as distance parameters between objects and an object and the beam, respectively. Having calculated all d_{ij} and d_{iB} , an assorted list is compiled. If the smallest entry is a d_{ij} then the corresponding objects are merged. If the smallest entry is a d_{iB} , object i is considered a "jet". As finalised object it is removed from the list. Thus this algorithm merges or finalises objects with large transverse momentum first. The quantity R is a resolution parameter which determines the distance at which two neighbouring jets are resolved. After each step the list is recalculated until all objects are finalised.

In ATLAS two versions of this algorithm are commonly used, only differing in the parameter R . These are named AntiKt4 and AntiKt6 with $R = 0.4$ and $R = 0.6$, respectively.

Jet Energy Scale and Resolution

The jet algorithm as used for data and detector-level simulation is using topological calorimeter clusters. The baseline calibration of these clusters is based on test-beam measurements. This corrects the cluster energy to the electromagnetic scale. Since the ATLAS calorimeters have a lower response to hadronic than to electromagnetic energy deposition, a further correction is needed once a jet is identified. This correction factor is determined with global cell weighting using simulated data and is mainly η and p_{T} dependent. Energy losses due to material in front of the calorimeters are also compensated by this calibration method. Dead material and fluctuations in the hadronic shower, in particular in its electromagnetic content, worsen the resolution beyond the intrinsic energy resolution of the calorimeters. Test-beam data [60, 61] and in-situ measurements [62, 63] show, that the detector simulation describes the calorimeter response to single hadrons to within 5%.

The final energy scale calibration and its uncertainty account by design for uncertainties in the hadronic shower modelling, description of calorimeter noise, material in front of the

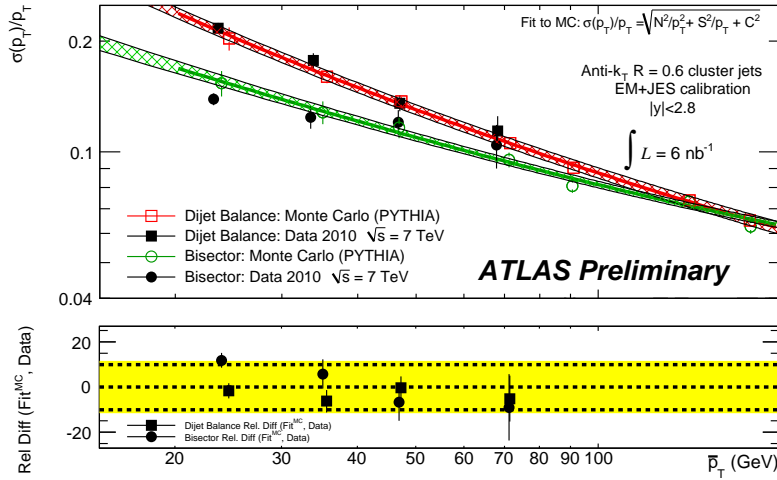


Figure 3.7.: Jet Energy Resolution for $\sqrt{s} = 7$ TeV, determined with an integrated luminosity of 6 nb^{-1} [65].

calorimeters and uncertainties due to differences between test-beam measurements and the in-situ detector. In a study done with the first 7 nb^{-1} of data [64], the jet energy scale calibration is determined using numerical inversion of the response calculated from MC. The overall p_T correction for jets is below 50%, for central jets (i.e. the barrel region) with $p_T > 60$ GeV below 35%. The overall uncertainty is below 9% for the entire η and p_T range and below 7% for central jets with $p_T > 60$ GeV. The effect of the uncertainty for the data analysis in this work is discussed in Section 5.5.

With the first 6 nb^{-1} of data the jet energy resolution was determined [65]. Two different techniques are used. The first method uses di-jet balance. A Gaussian is fitted to the distribution of the asymmetry of the two jet transverse momenta and its width is used to determine the resolution. The other method is called bi-sector method and uses an imbalance vector, defined as vector sum of the two leading jets in the event. Deviations from zero are used to determine the resolution. The results from both methods are compared two the MC prediction from PYTHIA. The result is shown in Figure 3.7. It is found that the MC simulation describes the jet energy resolution measured from data within 14% for jet transverse momenta between 20 and 80 GeV in the rapidity range $|\eta| < 2.8$.

Event Cleaning

Especially in the early data taking periods of an experiment it is probable to find a behaviour of the detector which are unexpected. These detector effects can lead to fake jets (called *bad jets*) or to problems in the jet energy scale (called *ugly jets*). Typical causes are sporadic noise cells in the LAr and Tile calorimeter, noise bursts in the HEC and coherent noise in the electromagnetic calorimeter. Additionally, cosmics and beam background can distort the measurement. To ensure a clean data sample, selection criteria have to be defined to find jet candidates which are with a high probability good jets, i.e. not bad or ugly jets. An extensive study of these effects has been done by the ATLAS collaboration [66]. These are the recommended selection criteria:

Reject jets created by detector effects (bad jets)

- The 5 cells with the highest energy deposition must contain less than 90 % of the energy of the jet.
- The fraction of the jet energy deposited in the hadronic end-cap (f_{HEC}) is less than or equal to 0.8.
- The absolute value of the jet quality variable, which quantifies how closely the measured calorimeter pulses match a reference pulse is less than $1 - f_{\text{HEC}}$.
- The fraction of energy of the jet deposited in the electromagnetic calorimeter is less than or equal to 0.95.
- The cell-weighted time of the jet is less than 50 ns different from the average event time.

Reject jets with problematic Jet Energy Scale (ugly jets)

- The fraction of the jet energy deposited in the TileGap3 scintillators must be less than or equal to 0.5.
- The fraction of the jet energy coming from masked cells, whose energy is extrapolated using the energy density of neighbouring cells, must be less than or equal to 0.5.

A fake or wrongly measured jet has two effects, both affecting the analysis. Besides the energy from the bad or ugly jet itself it leads to a mismeasurement of $E_{\text{T}}^{\text{miss}}$. Since, in this work, both values are used for the calculation of the visible invariant mass M_{inv} (see Section 3.3), this leads to poorly measured event properties. Thus if a bad or ugly jet is found with $p_{\text{T}} > 40$ GeV or $p_{\text{T}}^{\text{emscale}} > 10$ GeV the whole event is rejected. This avoids faked signal candidates and ensures a clean data sample.

Jet Selection

In this work jets reconstructed with the anti- k_{\perp} algorithm and a resolution parameter of $R = 0.4$ (AntiKt4) are used. With the smaller resolution factor, compared to $R = 0.6$, it is possible to better resolve objects. The transverse momentum is taken at the calibrated jet energy scale determined with global cell weighting. The momentum requirement for all jets is $p_{\text{T}} > 40$ GeV. This helps to reduce effects from pile-up. The fiducial selection is the restriction to central jets with $|\eta| < 2.8$. This is the range, for which the energy calibration is valid.

3.3.2. Electrons and Photons

Electrons and photons are identified using a common algorithm. The ATLAS standard electron and photon reconstruction and identification algorithm as defined in [67] is designed to have high identification efficiencies while providing different levels of background rejection. Starting point for the reconstruction is a seed cluster with $E_{\text{T}} > 2.5$ GeV in the second layer of the electromagnetic calorimeter. A track matching this cluster in a broad window of $\Delta\eta \times \Delta\phi = 0.05 \times 0.1$ is searched for among all reconstructed tracks with $p_{\text{T}} > 0.5$ GeV.

Photon Reconstruction

The cluster is considered a photon candidate, if either no matching track is found (unconverted photon candidate) or if there is a conversion vertex matched to the track (converted photon candidate). In the barrel region the required cluster size is $3 \times 7 (3 \times 5)$ cells for converted (unconverted) photon candidates, in the end-cap region it is 3×7 cells for all photon candidates.

Electron Reconstruction

If a track is found, this cluster is considered an electron candidate. The track matching closest to the barycentre of the cluster is kept. The required cluster size of final electron candidates is $3 \times 7 (5 \times 5)$ cells, corresponding to $\Delta\eta \times \Delta\phi = 0.075 \times 0.175 (0.125 \times 0.125)$ for the barrel (end-cap) calorimeter.

Identification

In order to ensure a high electron and photon identification efficiency while providing a good background suppression, there are three levels of electron identification selection, called *loose*, *medium* and *tight*. Each level adds further requirements to the previous one. They are defined in [67, 68, 69] and are summarised here.

- **loose (electron & photon):** This selection restricts electron (photon) candidates to $|\eta| < 2.47(2.37)$ due to the coverage of the inner layers of the electromagnetic calorimeter. Additionally, the region $1.37 < |\eta| < 1.52$ is excluded to ensure the finest granularity in the first layer. It also vetoes leakage to the hadronic calorimeter and uses the middle layer of the electromagnetic calorimeter for information on basic shower shape variables (lateral shower containment and shower width).
- **medium (electron):** This selection provides additional rejection of hadrons. It uses information from the first layer of the electromagnetic calorimeter (shower width and energy ratio of the difference between the largest and second largest energy deposition and the sum of these two energies), track quality (number of hits in pixel and SCT, transverse impact parameter) and track-cluster matching variables ($\Delta\eta$ between the cluster and the track extrapolated to the first layer of the electromagnetic calorimeter).
- **tight (electron):** This selection further rejects charged hadrons and electrons from conversion. It makes requirements on the ratio of cluster energy to track momentum, the number of hits in the TRT, and on the ratio of the number of high threshold hits to the number of total hits in the TRT. It also tightens the requirements for cluster-track matching ($\Delta\phi$ between cluster and track extrapolated to the second layer of the electromagnetic calorimeter). Electrons from conversions are rejected by requiring at least one hit in the first layer of the pixel detector.
- **tight (photon):** This selection provides further background rejection. The energy deposit ratio of different cluster sizes in the middle layer is evaluated. Using the first layer several shower shape selections are applied (shower width, fraction of energy

outside the core, ratio of the energy difference between the largest and second largest energy deposit over their sum). For further π^0 suppression also the energy difference between the strip with the second largest energy deposit and the strip with the smallest energy deposit between the two leading strips is evaluated.

Object Quality Selection

During the early data taking period some detector problems were discovered influencing the measurement of electrons and photons. These issues include dead and non-nominal high voltage regions, isolated dead or high-noise channels, and dead Front End Boards (including optical read-out links), which perform the read-out and digitisation of the calorimeter signals. Regions with such issues are marked in object quality maps. They add up to about 7% of the whole calorimeter area. To ensure a proper reconstruction and energy measurement, electron and photon candidates are selected to be outside regions, where either the pre-sampler or the first or second layers are affected. The full $3 \times 7 (5 \times 5)$ clusters in the barrel (end-cap) are required not to overlap with these regions.

Electron and Photon Selection

In this work, the electrons used are required to fulfil the medium selection of the identification algorithm. For photons the tight selection is applied. The transverse momentum selection for both electrons and photons is $p_T > 20$ GeV. Electron and photon candidates with energy deposition in regions marked in the object quality maps are rejected. If the energy deposition is also identified as a jet, which is a common case, this jet can still be used for the analysis. This helps to partially recover the energy from the rejected object.

3.3.3. Muons

Muons produce signals both in the inner detector (Section 3.2.2) and in the dedicated muon system (Section 3.2.4). The algorithms used to reconstruct and identify muons is described in detail in [67, 70]. In this work, muons measured with the *staco* algorithm are used. This method is shortly described in the following.

The *standalone muon* approach is based on muon system information only. It is independent of whether or not a matching track is found in the inner detector. It is initiated locally by the search for straight line track segments in the bending plane. The track segments are required to point towards the center of the ATLAS detector. Two or more segments from different muon stations are combined to form a muon track candidate. Track information (p_T , η , ϕ , transversal and longitudinal distance of closest approach to the primary vertex) are extrapolated to the interaction point.

Combined muon candidates are formed from the combination of standalone muon track candidates and tracks identified in the inner detector. A χ^2 -test is performed, evaluating the track parameters at the point of closest approach to the beam axis. The combined track parameters are calculated using a statistical combination (*staco*) of both the standalone and inner detector track information. Therefore these muon candidates are also called *Staco* muons.

Muon Selection

In this work, muons are identified as combined muons using the staco algorithm. The transverse momentum requirement is $p_T > 20 \text{ GeV}$ and muon candidates are restricted to $|\eta| < 2.0$.

Overlap Removal

Signals from showering objects like jets, electrons and photons are sometimes difficult to distinguish in the detector. Large energy depositions in the calorimeters are often identified as both a jet and an electron or photon. This leads to double-counting of the energy and wrong particle multiplicities. To resolve this ambiguity an overlap removal is applied in this work. This is based on the distance between two objects in $\eta - \phi$ space:

$$\Delta R = \sqrt{(\Delta\eta)^2 + (\Delta\phi)^2} \quad (3.10)$$

with $\Delta\eta$ and $\Delta\phi$ being the difference in pseudo-rapidity and azimuthal angle respectively. The order of priority of object removal is electrons, photons and jets. This reflects the fact, that electrons can be detected most reliably, while any energy deposition in the calorimeter often is already identified as jet. If the distance between a photon and an electron is $\Delta R < 0.1$, the photon is removed. If the distance of a jet to an electron or photon is $\Delta R < 0.2$, the jet is removed. The wider overlap exclusion region in this case is due to the larger shower opening angle of jets. This procedure resolves the ambiguity of identification while ensuring that deposited energy is taken into account.

3.3.4. Missing Transverse Energy

The reconstruction of the missing transverse energy E_T^{miss} is based on calorimeter deposits as well as on muon information. The algorithm and performance is described in [71]. The *calorimeter contribution* is calculated using cells from topological clusters. This helps to limit the number of contributing cells N_{cell} and thus the influence of noise on E_T^{miss} . On average, about 2500 cells are selected for this calculation in a collision event. For calibration purposes the so called *local cluster weighting scheme* is used. It first classifies a hadronic topocluster as electromagnetic or hadronic, depending on its topology. Additional corrections are applied for energy loss due to deposits outside the topocluster or in dead material in front or close to the topocluster. Weights determined from Monte Carlo simulations are then used to calibrate the topocluster cells. The *muon contribution* is calculated from both isolated and non-isolated (within $\Delta R < 0.3$ to the closest jet) muon candidates. Isolated muons are using the combined information from both the muon system and the inner detector as described in Section 3.3.3. For non-isolated muons it is impossible to distinguish between muon and jet tracks in the inner detector. Therefore the information from the muon system is only used, as long as there is no significant mismatch to the combined measurement.

The missing transverse energy is then calculated as:

$$\begin{aligned} E_{x(y)}^{\text{miss}} &= - \left(E_{x(y)}^{\text{calo}} + E_{x(y)}^{\mu(\text{iso})} + E_{x(y)}^{\mu(\text{non-iso})} \right) \\ E_{\text{T}}^{\text{miss}} &= \sqrt{(E_{\text{x}}^{\text{miss}})^2 + (E_{\text{y}}^{\text{miss}})^2} \end{aligned} \quad (3.11)$$

3.3.5. Trigger

In the early data taking period with a recorded integrated luminosity $\mathcal{L} = 297 \text{ nb}^{-1}$, the trigger decision is based only on Level 1. Since the instantaneous luminosity and therefore the interaction rate is low enough, a further reduction by the high level trigger is not necessary. During operation the performance of the trigger has been improved significantly. An example is a timing update of the Level-1 Calorimeter Trigger (L1Calo), which was conducted after a few weeks of operation. It was based on the initial timing update using splash events.

The following section will summarise the initial timing update shortly. The emphasis is placed on the methods developed during the course of this work. The details of the timing update can be found in Ref. [72].

Timing Update

The L1Calo system uses information from the calorimeters to form a trigger decision. Therefore it receives roughly 7200 analogue calorimeter signals. These signals are digitised in the L1Calo hardware with the LHC frequency of 40.08 MHz. The digitised samples are used at a later stage to measure the deposited energy and to assign it to the correct LHC bunch crossing.

To ensure correct operation the signal must be sampled at its peak. The difference has to be within $\pm 5 \text{ ns}$ for the resolution of the energy measurement to be better than 2% [73]. The hardware of the L1Calo system has the ability to adjust the sampling point with nanosecond precision. This so called fine timing offset has to be optimised for each of the 7200 channels individually.

The optimisation of the fine timing offset is only possible, if the difference between the signal peak and the sampling point is known. The L1Calo system only provides data of the digitised samples, thus limiting the timing resolution to 25 ns. An example of such a digitised pulse can be seen in Figure 3.8. To increase the precision of the timing measurement to the required nanosecond-level a fit is applied to the digitised samples. Various fitting functions have been investigated [74, 75] and a Landau and Gaussian hybrid function was found to describe the data best. In the course of this work, the function was further optimised using reconstructed pulses of the charge injection systems. Figure 3.8 shows one example of such a reconstructed pulse. These pulses are reconstructed by sampling 15 time slices, while shifting the sampling point by 1 ns steps across a 25 ns range. The initial fine timing offsets have been derived using reconstructed pulses.

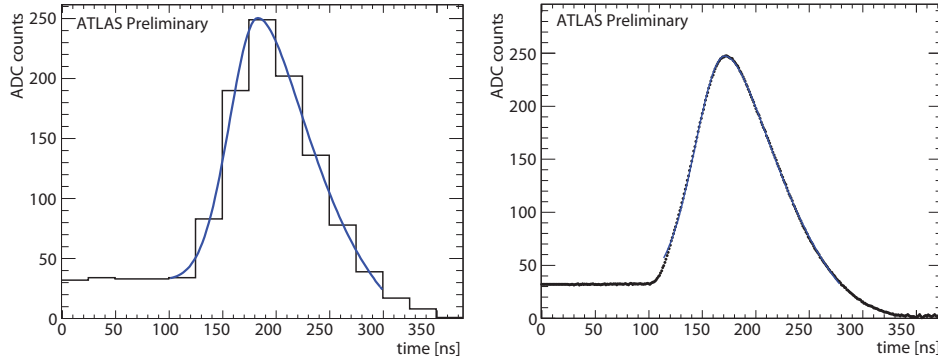


Figure 3.8.: Calorimeter pulse from the read-out of the L1Calo system (left). The right figure shows a reconstructed pulse with nanosecond time resolution. Both pulses are fitted with the Landau-Gaussian hybrid function defined in Equation (3.12) [72].

$$\begin{aligned}
 f(t \leq t_0) &= A \cdot \exp \left[-\frac{(t - t_0)^2}{2\sigma_{\text{gaussian}}^2} - \frac{1}{2} \right] + C \\
 f(t > t_0) &= \left(A + D \cdot \exp \left(\frac{1}{2} \right) \right) \cdot \exp \left[-\frac{1}{2} \left(\frac{t - t_0}{\sigma_{\text{landau}}} + \exp \left(-\frac{t - t_0}{\sigma_{\text{landau}}} \right) \right) \right] + C - D
 \end{aligned} \tag{3.12}$$

The optimised fit function is defined in Equation (3.12). On the rising edge a Gaussian is used, while a Landau describes the falling edge. Both functions are joined continuously at t_0 . The fit stability was increased by determining bounds on some of the fit parameters using the reconstructed pulses.

The fine timing offsets were measured using splash events which were delivered by the LHC prior to collisions in autumn 2009. Splash events are produced by proton bunches hitting the collimators located ± 145 m from the center of the ATLAS detector. These collisions produce secondary particle showers, which traverse the ATLAS detector and deposit a significant amount of energy in almost every channel of the L1Calo system. Therefore splash events provide an ideal environment for cross-checks and optimisations of the timing offsets derived with the charge injection systems.

Figure 3.9 shows the signal-peak time derived from a splash event. The signal-peak time is corrected for time-of-flight differences between collision and splash events. One can clearly see a distinct step at the border between the barrel and end-cap calorimeter at $|\eta| = 1.5$ in the hadronic layer. This stems from the fact that the relative phase between the calibration systems of the Tile and LArg calorimeter is unknown.

The final corrections to the timing offsets used for first collision data in 2009 have been

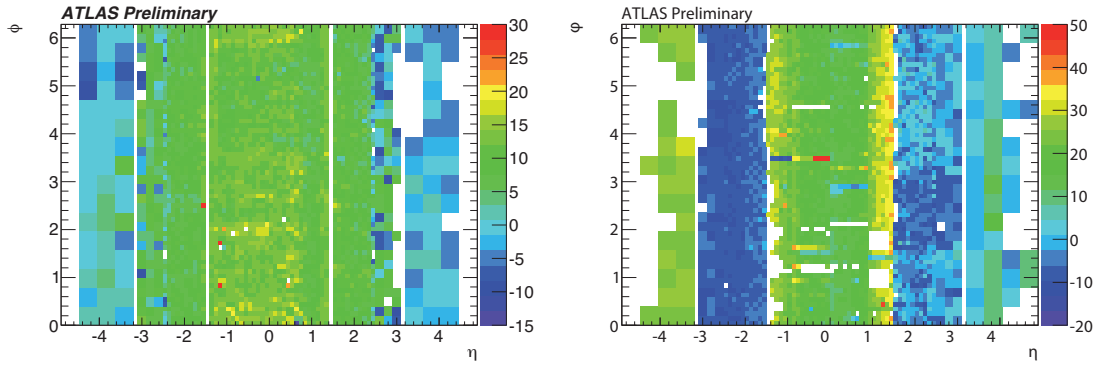


Figure 3.9.: Signal peak time location corrected for time-of-flight differences between collision and splash events. The left figure shows the electromagnetic layer, the right figure shows the hadronic layer [72].

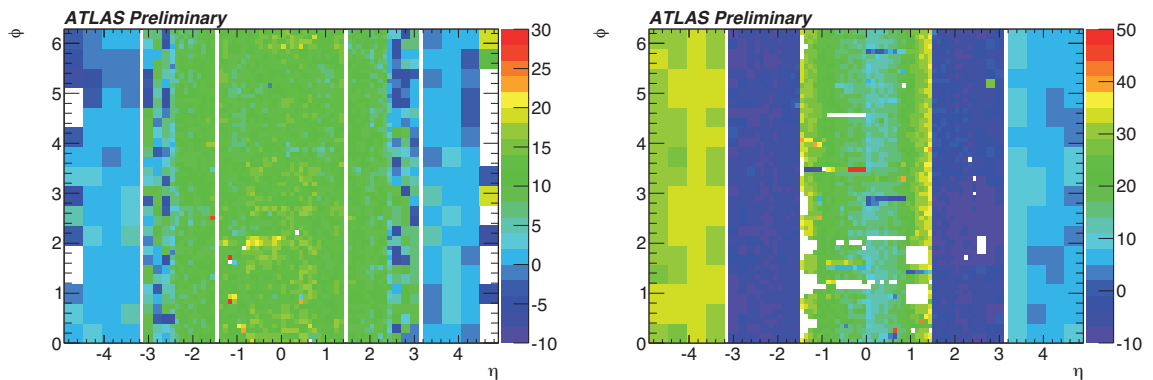


Figure 3.10.: Final peak time corrections derived from splash events in 2009. The left figure shows the electromagnetic layer, the right figure shows the hadronic layer [72].

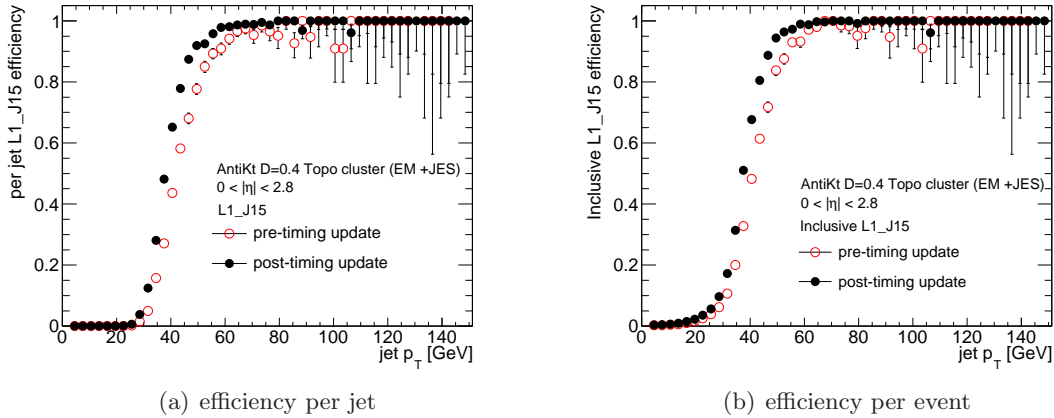


Figure 3.11.: Trigger efficiency for the trigger L1J15 before and after the timing update

derived using the average of all available splash events. They can be seen in Figure 3.10. For some channels no correction could be derived. This was mostly due to ongoing commissioning or saturation in the central region and lack of signal in the forward region. If possible, an average timing correction for these channels was derived from the neighbouring channels.

After this initial timing calibration further improvements of the fit function (3.12) have been achieved during the course of this work. Fixed parameters for each individual channel are determined from reconstructed pulses of the charge injection systems and then used for the fit of the reconstructed pulses from collision data. This method increases the fit stability further and allows a precise derivation of the fine timing offsets completely from data. Details of this method can be found in Ref. [76].

The effect of this data driven timing corrections on the trigger efficiency can clearly be seen by looking at Figure 3.11. For the lowest unscaled single jet trigger, called L1_J15 (also used for the analysis described in Chapter 5), the trigger efficiency per jet becomes fully efficient at 60 GeV after the timing update. Before the timing update the plateau is reached later at 80 GeV. Also the rise of the turn-on curve is steeper. For a jet with $p_T = 40$ GeV, the efficiency rises from 45 % to 65 %.

Debug Stream

For the first $\mathcal{L} = 297 \text{ nb}^{-1}$ of data, a total of 4820 events are stored in the debug stream due to errors during the trigger decision. Reasons for this errors are cosmic showers or punch through jets. A typical shower event is shown in Figure 3.12. The incident direction can clearly be seen in the hits of the inner detector. The number of hits and tracklets illustrate clearly, that a fast online trigger decision is hard to achieve for such an event. Nevertheless, comparing the number of debug stream events to the total number of about 1.3×10^8 events in this data sample, it can be concluded that the trigger reliability is already very high.

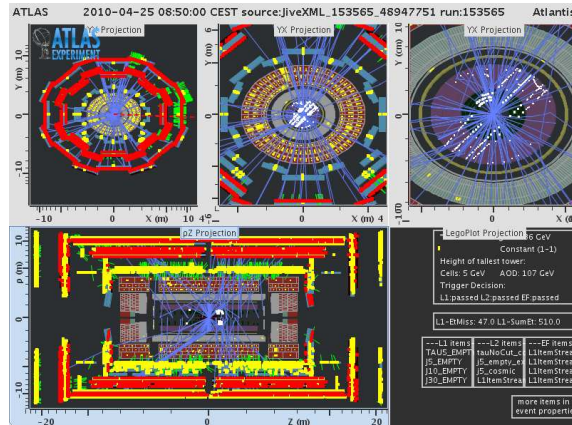


Figure 3.12.: ATLAS event display of a debug stream event (run 153565, event 48947751)

3.3.6. Luminosity

The luminosity is measured using LUCID [56]. The luminosity measurement was evaluated using both $\sqrt{s} = 900$ GeV and $\sqrt{s} = 7$ TeV data [77]. The biggest uncertainty on the luminosity measurement is contributed from the determination of the number of protons per bunch (10 %). Another uncertainty of 3 % is introduced due to the growth of the transverse emittance. In total, the uncertainty on the luminosity measurement with LUCID is 11 % [77].

Recently, an updated luminosity determination was published [78]. With an improved determination of the bunch current and thus the number of protons per bunch as well as other improvements it was possible to lower the luminosity measurement uncertainty to 3.4%. Since at the time of the studies presented in this work this improvement was not available, the first result is used.

3.4. Monte Carlo Simulation

The simulation of physics processes is embedded in the ATLAS software framework ATHENA. Events are generated with Monte Carlo generators suitable for the desired physics process. The following simulation of the interactions of generated final state particles with the detector as well as the digitisation is done with GEANT4 [79]. Afterwards the digitised data is reconstructed using the same algorithms as for real physics events. In the following, the Monte Carlo generators used in this work are shortly described.

Pythia

PYTHIA [80] is a leading order event generator. It is widely used in particle physics. It can generate about 240 different hard processes calculated with the leading order *matrix element* (ME) from Feynman diagrams. Higher order QCD processes are reproduced by parton showering based on leading log approximation. For hadronisation PYTHIA uses the string model [81, 82, 83, 84]. In this work PYTHIA 6.421 is used for QCD jet production

and the shower evolution and hadronisation of signal samples. The proton PDF set used is CTEQ6L1 [85] provided by LHAPDF [86].

Herwig and Jimmy

Herwig [87] is a leading order generator that uses the cluster model [88] for hadronisation. It is combined with Jimmy [89], which generates multi-parton scattering events. Herwig 6.510 and Jimmy 4.10 are used together with CTEQ6L1 PDFs for W/Z boson + jet production and for shower evolution and hadronisation of ALPGEN and MC@NLO events.

AlpGen

ALPGEN [90] is a tree level matrix element calculator for multi-parton final states. It uses the exact leading order ME and provides the calculation from $2 \rightarrow 2$ to $2 \rightarrow 6$ parton processes. ALPGEN only generates the hard process, while parton shower evolution and hadronisation are governed by HERWIG. This two step process leads to double counting of events with multi-parton final states, since during shower evolution additional partons are produced. To avoid these double countings MLM matching [91] is applied. Partons generated by ALPGEN are matched to jets from final state particles, based on their distance ΔR in the $\eta - \phi$ plane. If all partons match a jet and no jets are unmatched, then the event is kept. Otherwise it is rejected. In this work, ALPGEN 2.13 is used with PDF sets from CTEQ6L1 for QCD jet production as well as W boson + jets and Z + jets production.

MC@NLO

MC@NLO [92, 93] is a next-to-leading order generator. The shower evolution and hadronisation is done by HERWIG/JIMMY. MC@NLO is used in this work in version 3.41 with PDF sets from CTEQ6.6 for $t\bar{t}$ production.

Charybdis

CHARYBDIS is a black hole Monte Carlo generator. It is used in this work in two versions. Version 1.003 [94] is used for the study presented in Section 4.2. It is interfaced to HERWIG/JIMMY for parton evolution and hadronisation. This version can only simulate non-rotating black holes without the emission of gravitons. Version 2 of CHARYBDIS [35] implements also rotating black holes and graviton emission. The available physics scenarios are comparable to BLACKMAX. One additional feature is the possibility to fix the number of final burst particles. This version is interfaced to PYTHIA for parton evolution and hadronisation and is used in Chapter 5.

3.5. BlackMax

BLACKMAX [27, 95] is a Monte Carlo generator used to generate black holes in different scenarios with extra dimensions. It only provides the production and decay of the black hole. The following shower evolution and hadronisation is done with PYTHIA. In this work, BLACKMAX is used with the CTEQ6.6 PDFs.

BLACKMAX allows the simulation with different scenarios, which might have a significant influence on the production and decay of black holes, as described in Chapter 2. Available are:

- Rotating black hole on a tensionless brane.
- Non-rotating black hole on a tensionless brane.
- Non-rotating black hole on a tensionless brane with fermion brane splitting.
- Non-rotating black hole on a non-zero tension brane.

A list of all available parameters can be found in Appendix B. The first scenario is used throughout this work, if not otherwise stated. The most important other parameter choices are:

- The PDG definition [9] for the fundamental Planck mass M_D is used.
- Lepton number, baryon number and charge are conserved in the decay.
- For the Planck phase of the decay, the final burst model is chosen with a variable number of particles. It is implemented as follows:
 1. The numbers of decay particles are counted according to their electric charge: $N_{\pm 1/3}$ for down-type quarks, $N_{\pm 2/3}$ for up-type quarks, $N_{\pm 1}$ for charged leptons and W bosons, N_g for gluons and N_n for the uncharged particles ν, γ, Z, H .
 2. The smallest sum N for a combination of all N_i , which conserves electric and color charge, is chosen.
 3. If $N < 2$, additional N_n uncharged particles are added, until $N = 2$.
 4. For every N_i , the particles are chosen according to their degrees of freedom, as in Hawking radiation.
 5. Momenta and energies are assigned to the particles randomly, conserving the momentum and energy of the black hole at the time of the final burst.

Implementation

In the course of this work, BLACKMAX was implemented [96] and validated [97] for the ATLAS collaboration. The basic principle is to generate the production and decay into primary decay particles externally using BLACKMAX. The output is then interfaced to ATHENA using *Les Houches Accord Event Files*. This format [98] was developed as a standard for external generators. In close collaboration with the authors of BLACKMAX the according output format was implemented as an option into the generator. The format uses XML-encoding and defines all relevant information needed for the following steps in the event generation chain. The basic production information is given once for all events in the form:

```
<init>
IDBMUP(1) IDBMUP(2) EBMUP(1) EBMUP(2) PDFGUP(1) PDFGUP(2) PDFSUP(1) PDFSUP(2) IDWTUP NPRUP
XSECUP XERRUP XMAXUP LPRUP
</init>
```

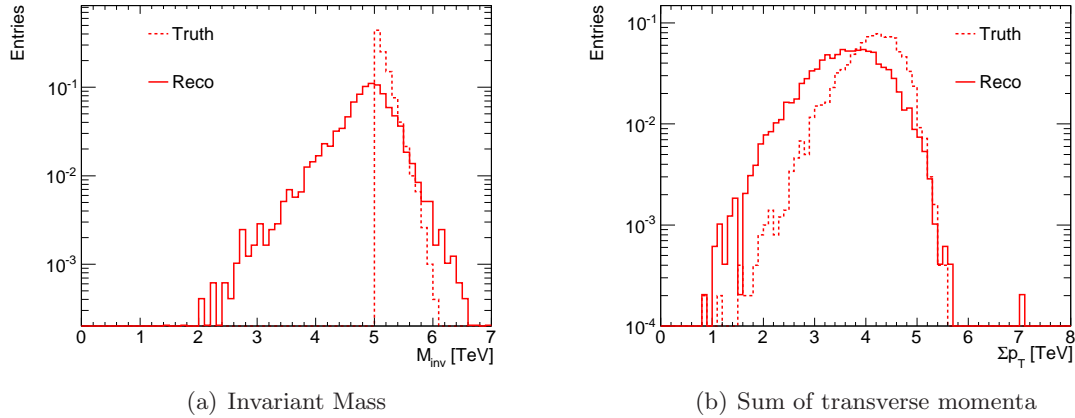


Figure 3.13.: Distributions of the invariant mass (a) and sum of transverse momenta (b) for a BLACKMAX sample with $n = 7$ extra dimensions, $M_D = 1$ TeV and $M_{\text{th}} = 5$ TeV. Shown are the truth information (dashed line) after the primary decay of the black hole and the reconstructed information after the MC chain within ATHENA. Both distributions are normalised to unity.

The stored information are the beam particle ID (`IDBMUP(1,2)`), the energy of the beams (`EBMUP(1,2)`), the PDF sets used (`PDFGUP(1,2)`, `PDFSUP(1,2)`), the weighting strategy (`IDWTUP`), the number of separately identified processes (`NPRUP`). These processes are then listed in the following lines with the corresponding cross section (`XSECUP`), the cross section error (`XERRUP`), the maximum weight (`XMAXUP`) and the identifier for the process (`LPRUP`).

Every event is formatted as follows:

```
<event>
NUP IDRUP XWGTUP SCALUP AQEDUP AQCDUP
IDUP(I) ISTUP(I) MOTHUP(1,I) MOTHUP(2,I) ICOLUP(1,I) ICOLUP(2,I)
↪ PUP(1,I) PUP(2,I) PUP(3,I) PUP(4,I) PUP(5,I) VTIMUP(I) SPINUP(I)
</event>
```

Here the first line holds the number of particles in the event (`NUP`), the identity of the process (`IDRUP`), the weight of the event (`XWGTUP`), the Q scale of the event (`SCALUP`), the used value, if any, for α_{em} (`AQEDUP`) and α_S (`AQCDUP`). The next `NUP` lines give the details for every involved particle: the PDG ID (`IDUP(I)`), the status of the particle (`ISTUP(I)`), the mother particles (`MOTHUP(1,2,I)`), the color flow lines (`ICOLUP(1,2,I)`), the particle momentum vector (p_x, p_y, p_z, E, m) (`PUP(1-5,I)`), the invariant lifetime of a decaying particle (`VTIMUP(I)`) and the cosine between the spin vector of a particle and its three-momentum (`SPINUP(I)`). The sign \hookrightarrow denotes the continuation of the line before. Details on all variables can be found in e.g. the PYTHIA manual [80].

Validation

In the following, basic kinematic distributions are shown for one example scenario produced with BLACKMAX. Displayed are the truth information before and the reconstructed

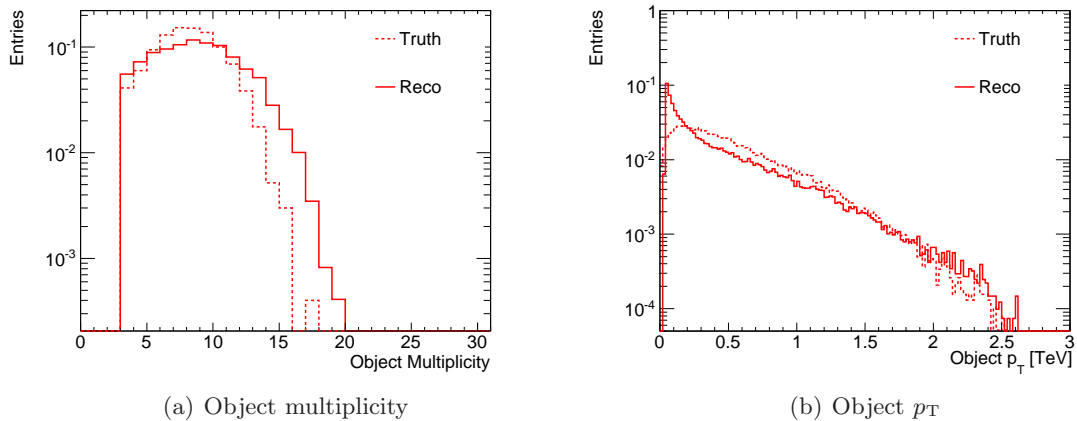


Figure 3.14.: Object multiplicity and transverse momentum for a BLACKMAX sample with $n = 7$ extra dimensions, $M_D = 1$ TeV and $M_D = 5$ TeV. Shown are the truth information (dashed line) after the primary decay of the black hole and the reconstructed information after the MC chain within ATHENA. Both distributions are normalised to unity.

information after showering and hadronisation with PYTHIA and the simulation and reconstruction chain in ATHENA. The chosen sample is simulated using rotating black holes with $n = 7$ extra dimensions, a fundamental Planck mass of $M_D = 7$ TeV and a threshold mass of $M_{\text{th}} = 1$ TeV. The latter is clearly visible in the invariant mass spectrum in Figure 3.13 (a). For the truth information, the true mass of the generated black hole is shown. The reconstructed invariant mass is calculated using all reconstructed objects as defined above. The true mass distribution shows a sharp turn-on at the threshold mass, and falls quickly for higher masses due to kinematics. The reconstructed mass also peaks at the threshold mass. The sharp turn-on has vanished, instead the reconstructed mass starts as low as 2 TeV due to the resolution. The same argument holds for higher masses, where the reconstructed mass exceeds the true mass. The truth transverse momentum sum distribution as shown in Figure 3.13 (b) starts at 1.5 TeV, peaks at 4 TeV and ends below 6 TeV. The distribution for reconstructed objects deviates clearly. Beside the resolution effect already mentioned for the mass distribution, the transverse momenta of non-interacting particles like neutrinos and gravitons from black hole emission and secondary decays are not contributing to this sum. Therefore the distribution extends to smaller values and peaks earlier at 3.5 TeV, compared to the truth information.

The object multiplicity per event is displayed in Figure 3.14 (a). The effect of the missing non-interacting particles in the reconstructed sample is overcompensated by secondary decays of gauge bosons and initial and final state radiation. Both the truth and the reconstructed distribution peak around a multiplicity of 8 – 9 objects. The reconstructed multiplicity extends up to 20 objects per event. The inclusive object p_T distribution as shown in Figure 3.14 (b) shows good shape agreement between truth and reconstruction for high- p_T values above ~ 1 TeV. For lower values secondary decays and initial and final state radiation lead to an increase in the reconstructed p_T distribution. While the true transverse

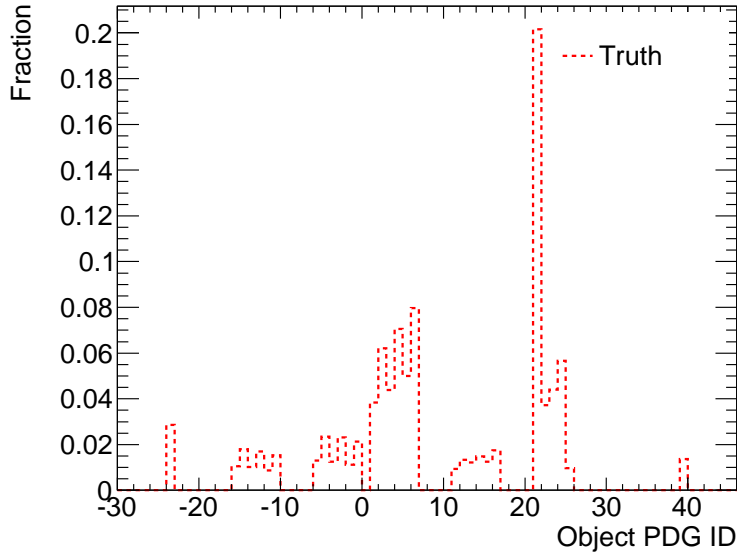


Figure 3.15.: Distribution of the PDG ID of the emitted article for a BLACKMAX sample with $n = 7$ extra dimensions, $M_D = 1$ TeV and $M_D = 5$ TeV. Shown is the truth information after the primary decay of the black hole. The distribution is normalised to unity.

momentum peaks around 200 GeV, the reconstructed p_T distribution rises towards smaller values until the selection requirement of $p_T > 40$ GeV for jets.

The emission spectrum of a black hole is dominated by jets, as can be seen in Figure 3.15, where the fraction of the total emission of particle types according to their PDG ID [2] is displayed. Gluons (21) are the largest contribution to the particle spectrum (20%). Together with quarks (1 – 6) and anti-quarks (–1 – –6) they account for a jet fraction⁸ of $\sim 65\%$. Compared to QCD expectations, the fraction of direct electrons and muons is also high (5%).

In conclusion, the implementation of BLACKMAX into the software framework ATHENA including its simulation chain was successful and the generated samples can be used to study interesting final states as shown in the next chapters.

⁸neglecting the secondary decays of gauge bosons

4. Search Strategies

The prediction of effects like microscopic black holes at the LHC opens up the opportunity to search for new physics beyond the Standard Model already with small datasets due to the high predicted cross sections and clear signature. Different search strategies have been developed, according to the LHC run plans at the time of the study. In the course of this work, contributions to different studies were made. The first study was aiming at microscopic black holes at $\sqrt{s} = 14$ TeV, where especially the trigger behaviour of black holes were in the focus of this work. This study was published in the context of the CSC efforts of the ATLAS experiment [99]. The resulting strategies are compared to a different approach, which was developed to also cover scenarios with suppressed lepton emission and is based on simulations for $\sqrt{s} = 10$ TeV. The main contributions are in sample generation, selection strategy and discovery reach. This study is already covered well in the context of another work [100] and presented to the ATLAS collaboration [101]. Finally, an adaptation of this search strategy for $\sqrt{s} = 7$ TeV is presented.

4.1. Signal Properties

The production and decay of microscopic black holes at the LHC as described in Chapter 2 provides a striking signature. Although model uncertainties and parameter space are large, key features of most models are consistent within the different predictions:

- Large multiplicity of high energetic final state particles due to the thermal decay.
- Final state particle spectrum dominated by jets, but possibly with a significant fraction of electroweak objects. Driven by Hawking radiation, the particle spectrum composition of the final state depends on the available degrees of freedom for different particle species as well as on grey body factors describing suppression or enhancement of certain species due to properties of the extra dimensions.
- Large invariant mass and scalar sum of transverse momentum over all final state particles due to the high production mass of the black hole.
- Long tail in the missing transverse energy E_T^{miss} distribution due to the emission of high energy neutrinos and gravitons.

4.2. Selection Strategies with Leptons

First search strategies for black holes were developed and presented for $\sqrt{s} = 14$ TeV [99]. They exploit the key features of the decay, namely the large multiplicity of particles with

high transverse momenta and the large scalar sum of transverse momenta. Additionally they use the abundance of leptons with high p_T in the decay to further suppress the SM background. For this study the black hole Monte Carlo generator CHARYBDIS [94] interfaced with HERWIG/JIMMY is used. The main parameters are listed below:

- Minimum black hole mass $M_{\text{th}} = 5 \text{ TeV}$.
- Fundamental Planck mass $M_{\text{DL}} = 1 \text{ TeV}$ in the definition $M_{\text{DL}}^{n+2} = G_{\text{D}}^{-1}$ [11].
- Final burst decay into two particles.
- Baryon number, electric und colour charge are conserved in the decay.

The three main signal samples are generated with $n = 2, 4, 7$ extra dimensions and non-rotating black holes. The respective cross sections are $\sigma = 40.7 \text{ pb}$, 24.3 pb and 22.3 pb . The different definition of the fundamental Planck mass compared to Chapter 2 leads to a decrease in cross section for larger numbers of extra dimensions.

The considered background processes are QCD jet, $t\bar{t}$, W + jets and Z + jets. The cross sections for the different processes are listed in Table 4.1.

Process	Event Generator	Cross section [pb]
QCD jet production	PYTHIA	12.84×10^3
$t\bar{t}$	MC@NLO	833
Z +jets	ALPGEN	560
W +jets	ALPGEN	51.8

Table 4.1.: Background processes with event generator and cross section.

Triggering on Black Holes

Since jets typically carry a dominant fraction of the visible decay energy, they provide the best option for triggering on black holes. The simulated trigger efficiencies for the three trigger levels are shown in Figure 4.1 for different trigger thresholds as a function of the offline reconstructed jet p_T . The efficiencies are shown for the black hole sample with $n = 2$ extra dimensions. A matching is required between the offline reconstructed jet and the trigger jet object on the respective level. Every offline reconstructed jet is matched to the closest trigger jet object in ΔR . For Level-1, a modified approach is necessary to avoid incorrect matching. In a radius of $\Delta R < 0.5$ around the offline reconstructed jet, all trigger jet objects are evaluated and the one closest in energy is chosen as match.

The shape of the Level-1 trigger efficiency for a trigger threshold of 800 GeV is due to the saturation of Level-1 trigger tower energies at 255 GeV. If the deposited energy in one of the four trigger towers corresponding to a trigger jet object of Level-1 exceeds 255 GeV, the p_T of the trigger jet object is set to $4 \times 255 \text{ GeV} = 1020 \text{ GeV}$.

The trigger efficiencies for single jets show the expected behaviour on all trigger levels. The trigger efficiencies for the single-jet, three-jet and four-jet trigger are displayed in Figure 4.2

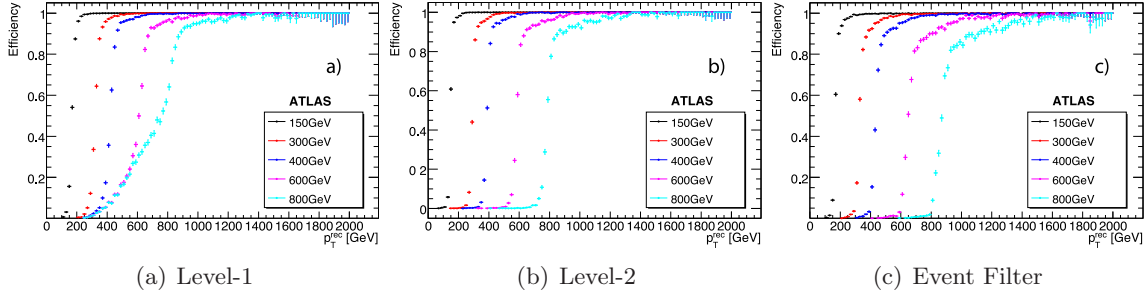


Figure 4.1.: Simulated jet trigger efficiencies as functions of the offline reconstructed jet p_T Level-1 (a), Level-2 (b) and Event Filter (c), for different trigger p_T -thresholds for $\sqrt{s} = 14$ TeV [99].

Trigger	$n = 2$			$n = 4$			$n = 7$		
	L1	L2	EF	L1	L2	EF	L1	L2	EF
j100	1	1	1	1	1	1	1	1	1
j400	0.997	0.997	0.997	0.977	0.997	0.996	0.990	0.987	0.985
3j100	0.998	0.998	0.998	0.952	0.952	0.952	0.807	0.806	0.805
3j250	0.972	0.971	0.971	0.886	0.885	0.885	0.710	0.704	0.704
4j100	0.985	0.985	0.985	0.807	0.806	0.806	0.525	0.522	0.522
4j250	0.865	0.862	0.862	0.612	0.607	0.607	0.343	0.341	0.341

Table 4.2.: Simulated jet trigger efficiencies for black hole events as functions of the jet p_T threshold for CHARYBDIS samples with $M_{\text{th}} = 5$ TeV [99].

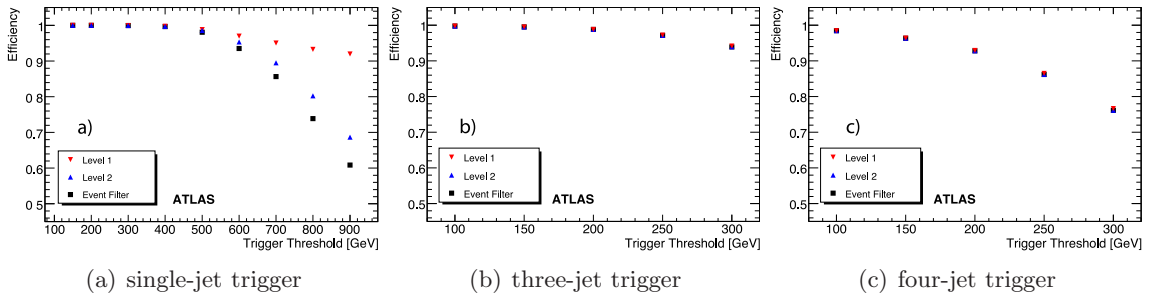


Figure 4.2.: Simulated trigger efficiencies as functions of the trigger threshold for single-jet (a), three-jet (b) and four-jet trigger (c) [99].

as a function of the trigger threshold. The efficiencies for the three signal samples are summarised in Table 4.2. The highest efficiency is provided by the single-jet trigger, which is considered the master trigger for black holes. It shows an efficiency of $> 99\%$ at all trigger levels for a trigger threshold of up to 400 GeV. The expected rate for Standard Model processes at this threshold is expected to be less than 0.1 Hz for an instantaneous luminosity of $10^{31} \text{ cm}^{-2} \text{ s}^{-1}$, allowing for an unpre-scaled use of this threshold for the first year of running at $\sqrt{s} = 14 \text{ TeV}$. But also multi-jet triggers with a moderate trigger threshold of $\leq 200 \text{ GeV}$ provide a high efficiency and are an option in the case that the single-jet trigger is pre-scaled.

Selection Strategies

Jets, electrons, photons and muons are defined as objects. The minimum p_T requirement for jets is 20 GeV, for all other objects it is 15 GeV. The first selection strategy uses the high Σp_T of black hole events to suppress the background. Figure 4.3 (left) shows the invariant mass distributions after a requirement of $\Sigma p_T > 2.5 \text{ TeV}$ for the signal sample with $n = 2$ extra dimensions and for the background samples. A further lepton requirement (electron or muon) with $p_T > 50 \text{ GeV}$ reduces the number of background events significantly. This is shown in Figure 4.3 (right).

A second approach is to exploit the large multiplicity of objects with high transverse momentum in black hole events. Selecting events with at least four objects with $p_T > 200 \text{ GeV}$ suppresses the background efficiently, as can be seen in Figure 4.4 (left). Requiring at least one lepton with $p_T > 200 \text{ GeV}$ in the event again reduces the number of background events significantly. Figure 4.4 (right) shows the invariant mass distributions after both requirements.

Table 4.3 shows the acceptance and remaining number of events for both selection strategies. Especially the QCD jet production events are significantly suppressed by the lepton requirement in both cases.

To determine the discovery reach of these strategies for data taken with $\sqrt{s} = 14 \text{ TeV}$, the integrated luminosity is evaluated, which is required to detect a minimum of 10 events, with $N_S/\sqrt{N_B}$. Here, N_S is the number of detected signal events and N_B the expected number of background events. The sensitivity for different black hole masses is estimated

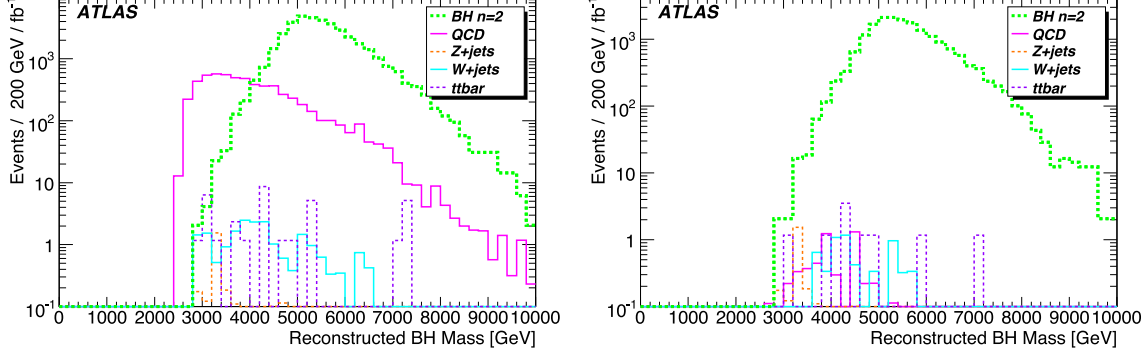


Figure 4.3.: Invariant mass distributions for $\sqrt{s} = 14$ TeV after requiring $\Sigma p_T > 2.5$ TeV (left), and after additionally requiring a lepton with $p_T > 50$ GeV. Displayed are the distributions for the signal sample with $n = 2$ extra dimensions and for background samples [99].

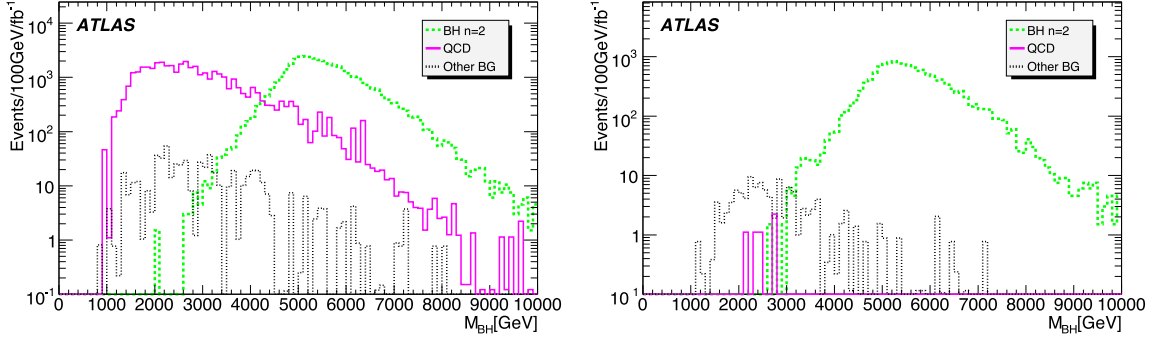


Figure 4.4.: Invariant mass distributions for $\sqrt{s} = 14$ TeV after requiring at least four objects with $p_T > 200$ GeV (left), and after additionally requiring at least one lepton with $p_T > 200$ GeV in the event. Displayed are the distributions for the signal sample with $n = 2$ extra dimensions and for background samples [99].

Datset	$\Sigma p_T + \text{lepton}$		4-object + lepton	
	Events [fb]	Acceptance	Events [fb]	Acceptance
$n = 2$	$14.0 \pm 0.2 \times 10^3$	0.34	$18.6 \pm 0.2 \times 10^3$	0.46
$n = 4$	4521 ± 126	0.19	6668 ± 83	0.27
$n = 7$	1956 ± 82	0.087	3574 ± 60	0.17
$t\bar{t}$	36_{-9}^{+12}	4.3×10^{-5}	$8.2_{-2.43}^{+2.43}$	9.8×10^{-6}
QCD jets	6_{-3}^{+107}	5.6×10^{-7}	$5.37_{-2.02}^{+3.25}$	4.3×10^{-7}
W+jets	56_{-13}^{+24}	1.0×10^{-3}	$4.67_{-0.93}^{+8.75}$	2.4×10^{-6}
Z+jets	19_{-3}^{+90}	4.0×10^{-4}	$2.57_{-0.64}^{+0.95}$	5.0×10^{-5}

Table 4.3.: Acceptance and remaining events in 1 fb^{-1} for signal and background after the $\Sigma p_T + \text{lepton}$ and the four-objects + lepton selection [99].

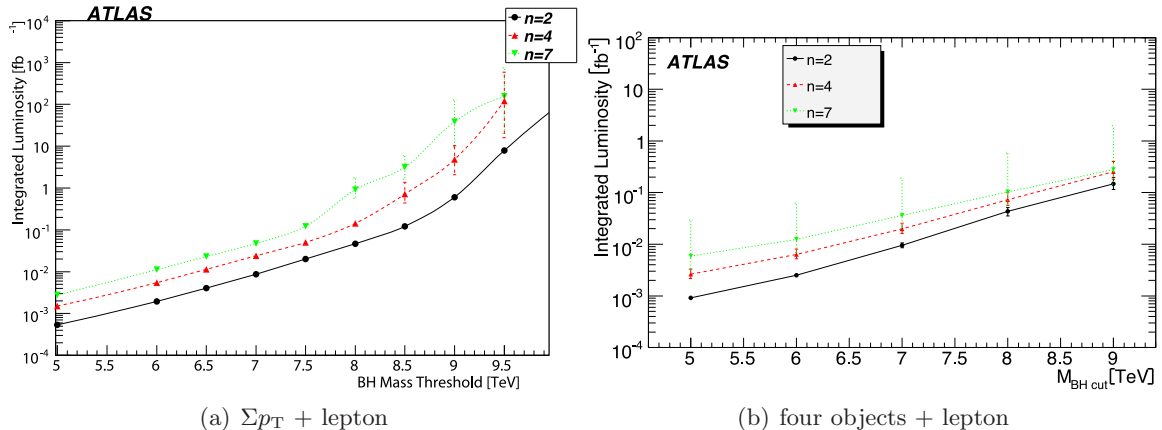


Figure 4.5.: Discovery reach for the Σp_T + lepton requirement (left) and the four-objects + lepton requirement (right) as a function of the minimum reconstructed invariant mass for $\sqrt{s} = 14$ TeV [99].

by requiring a respective minimum reconstructed invariant mass. The resulting discovery reach is displayed in Figure 4.5 for the Σp_T + lepton (left) and the four-object + lepton requirement (right). With only a small amount of data, corresponding to $\sim 1 \text{ pb}^{-1}$, it should be possible to discover black holes with $M_{\text{inv}} = 5$ TeV. Even higher masses are within reach with less than 1 fb^{-1} of data taken with $\sqrt{s} = 14$ TeV.

4.3. 5-Object Selection Strategy

The study presented above was aimed at $\sqrt{s} = 14$ TeV. The plans for the LHC were adjusted to running at $\sqrt{s} = 10$ TeV. At the same time, a new Monte Carlo generator, BLACKMAX, was published and integrated into the ATLAS software framework in the course of this work. With this generator it is possible to study a wider variety of scenarios with different particle emission behaviour for microscopic black holes. In the following a study of search strategies for $\sqrt{s} = 10$ TeV is discussed, which was presented to the

Signal Samples

For this study samples generated with BLACKMAX [27, 95] are used. The fragmentation and hadronisation is done with PYTHIA. The detector simulation is done using the ATLAS fast simulation ATLFAST [102]. It uses a simple parametrization of the detector response. The result is a realistically smeared truth information with the advantage of fast processing time and the drawback of missing detailed detector properties like e.g. granularity. Nevertheless this is sufficient to study basic signal features and acceptances.

Table 4.4 lists the different signal samples. They cover a broad range of scenarios available from BLACKMAX, which are described in more detail in Chapter 3. The naming convention is the following. "C" denotes the simulated scenario and "N" the number of extra dimensions. The first two samples contain non-rotating black holes produced with a model of two (seven)

Sample	Model Scenario	n	n_s	a / TeV^{-1}	B	σ / pb
C1_N2	tensionless, nonrotating, nonsplit	2	0	–	1.0	2.51
C1_N7	tensionless, nonrotating, nonsplit	7	0	–	1.0	16.27
C2_N2	tension, nonrotating, nonsplit	2	0	–	0.9	8.51
C3_N2	tensionless, rotating, nonsplit	2	0	–	1.0	2.55
C3_N7	tensionless, rotating, nonsplit	7	0	–	1.0	16.75
d2_n1	tensionless, nonrotating, split	2	1	10.0	1.0	1.94
d7_n1	tensionless, nonrotating, split	7	1	10.0	1.0	14.15

Table 4.4.: Major parameters of BLACKMAX samples used in this strategy analysis: number of extra dimensions n , number of split dimensions n_s , distance parameter for split dimensions a , and deficit angle parameter characterising brane tension B . Production cross sections σ are given for $\sqrt{s} = 10 \text{ TeV}$ with the black hole mass range $M_{\text{BH}} > 5 \text{ TeV}$ and $M_{\text{D}} = 1 \text{ TeV}$.

extra dimensions with tensionless, non-split branes. They are denoted in the following as C1_N2 (C1_N7). The third sample (C2_N2) is generated using a model with two extra dimensions and a non-split brane with tension. For other numbers of extra dimensions the necessary grey-body factors are not yet calculable. The brane tension leads to an increase of the event horizon radius and thus to a decrease of the Hawking temperature of the black hole. The black holes are again non-rotating. This is different for the next two samples, C3_N2 and C3_N7. Here rotating black holes are produced within a model with 2 and 7 extra dimensions, again with a tensionless and non-split brane. The spin reduces the event horizon of the black hole and thus raises its Hawking temperature. The last two samples (d2_n1 and d7_n1) are not using the above described naming convention. They are generated using a model with two ("d2") and seven ("d7") extra dimensions including one dimension ("n1") with splitted branes for leptons and quarks. This separation leads to a suppression of lepton emission, since a black hole at a hadron collider is produced on the quark brane. This may lead to a different acceptance compared to the other signal samples.

Standard Model Background Samples

The main contributions to the background in this analysis are expected from QCD jet production and $t\bar{t}$ production. The important parameters of the used background samples are summarised in Table 4.5.

The $t\bar{t}$ sample is generated using PYTHIA [80]. QCD jet production, being the dominant process in a hadron collider, is simulated with two Monte Carlo generators, PYTHIA and ALPGEN [90]. A short description of the generators can be found in Chapter 3.

Comparing the results from both Monte Carlo generators helps to estimate uncertainties due to the modelling of QCD processes. As can be seen in Figure 4.6 the cross section prediction for the two generators differs. In a potential data analysis, the background predictions are usually normalised to data in a control region. In order to simulate this and to only be sensitive to shape differences, ALPGEN is normalised to PYTHIA in a kinematic regime similar to a potential signal region. In this case, due to the black hole threshold

Process	Generator	Sample	p_T -region [GeV]	σ [pb]	# Events
$t\bar{t}$	PYTHIA	$t\bar{t}$		220.5	10^6
QCD	PYTHIA	J5	280-560	5133	10^6
		J6	560-1120	112	10^6
		J7	1120-2240	1.074	10^6
		J8	> 2240	1.118×10^{-3}	10^6
QCD	ALPGEN	Np2J5Plus	> 280	750.6	50 000
		Np3J5Plus	> 280	1920.0	46 926
		Np4J5Plus	> 280	2173.4	43 927
		Np5J5Plus	> 280	1431.6	41 350
		Np6J5Plus	> 280	967.9	38 095

Table 4.5.: Standard Model background samples and the respective process cross sections at $\sqrt{s} = 10$ TeV.

mass of $M_{\text{th}} = 5$ TeV, the invariant mass prediction at 3 TeV is used to determine a scale factor for ALPGEN of 0.54. This avoids the discrepancy due to cross section predictions and is generally applied to all ALPGEN distributions.

If not otherwise stated, all following numbers and figures are always for the sum of the $t\bar{t}$ and PYTHIA respectively ALPGEN sample.

Object Selection

Since this study uses samples simulated with ATLFast, no sophisticated object reconstruction and identification is possible. Jets, electrons, photons and muons are commonly defined as objects. The selection criteria are the following. Jets are reconstructed using the cone algorithm with a radius¹ of $R = 0.4$. The minimum transverse momentum requirement is $p_T > 20$ GeV. For electrons, photons and muons isolation is required. This is defined with an upper threshold for the deposited energy ($E_{\text{dep}} < 10$ GeV) in a cone ($R = 0.2$) around the object. Additionally, the distance to the next object is required to be $\Delta R > 0.4$. Only isolated objects are considered. The minimum transverse momentum requirement for these objects is $p_T > 15$ GeV. For all objects a fiducial selection of $|\eta| < 2.5$ is applied. The missing transverse energy is calculated from all non-interacting particles. Since it is not measurable in the detector, how many particles produced the missing transverse energy, it is not counted as object.

The transverse momentum sum Σp_T is defined as scalar sum using all objects plus the missing transverse energy E_T^{miss} . The invariant mass is defined as

$$M_{\text{inv}} = \sqrt{p^2} \quad \text{with} \quad p = \sum_{i=\text{objects}} p_i + (E_T^{\text{miss}}, E_x^{\text{miss}}, E_y^{\text{miss}}, 0), \quad (4.1)$$

due to the missing z component information of the missing energy.

¹ $R = \sqrt{\eta^2 + \phi^2}$

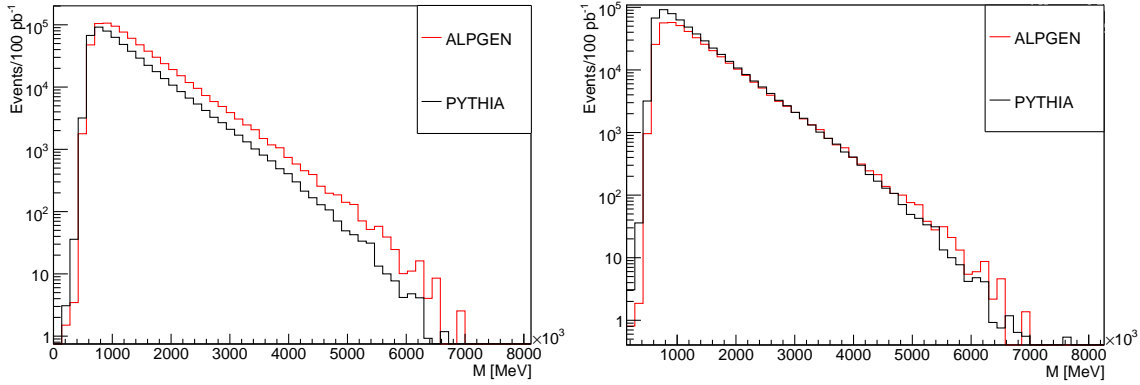
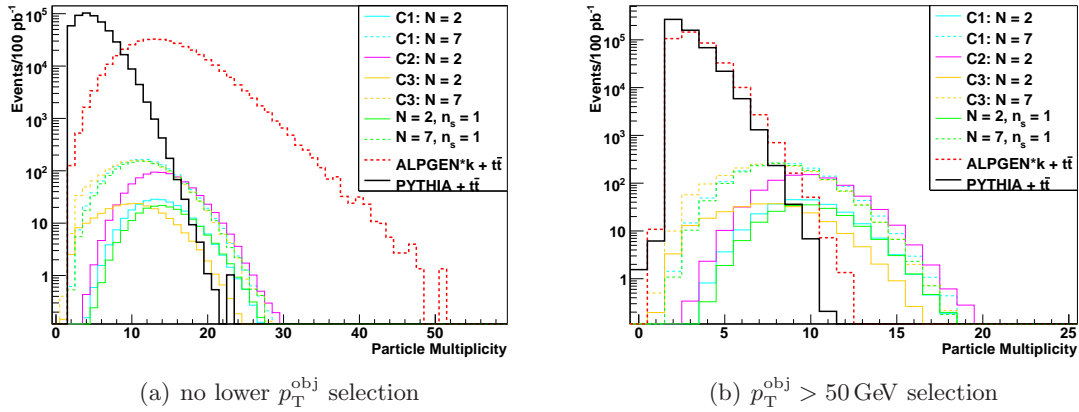


Figure 4.6.: Reconstructed invariant mass for $\sqrt{s} = 10$ TeV for PYTHIA and ALPGEN samples before (left) and after (right) rescaling of ALPGEN at $M_{\text{inv}} = 3$ TeV [101].



(a) no lower p_T^{obj} selection

(b) $p_T^{\text{obj}} > 50$ GeV selection

Figure 4.7.: Object multiplicity for $\sqrt{s} = 10$ TeV for signal and background samples without (a) and with (b) an additional selection on the object p_T [101].

Distributions

Figure 4.6 shows the invariant mass distributions for the two QCD jet production generators PYTHIA and ALPGEN calculated from all objects without any further selection. On the left both samples are normalised to a luminosity of $\mathcal{L} = 100 \text{ pb}^{-1}$. While agreeing well in shape ALPGEN predicts more events than PYTHIA. As explained above ALPGEN is therefore scaled with a factor of 0.54. The resulting distributions are shown on the right. The shape differences are small for the inclusive samples. All following distributions are scaled with this factor.

The object multiplicity is shown in Figure 4.7. Due to the higher cross section the background samples have a much higher number of events for the same luminosity of $\mathcal{L} = 100 \text{ pb}^{-1}$. Also the much higher prediction for the multiplicity from ALPGEN compared with PYTHIA and signal samples is visible. Applying a selection on the objects' transverse momentum of $p_T > 50$ GeV suppresses soft radiation effectively. The resulting distribution

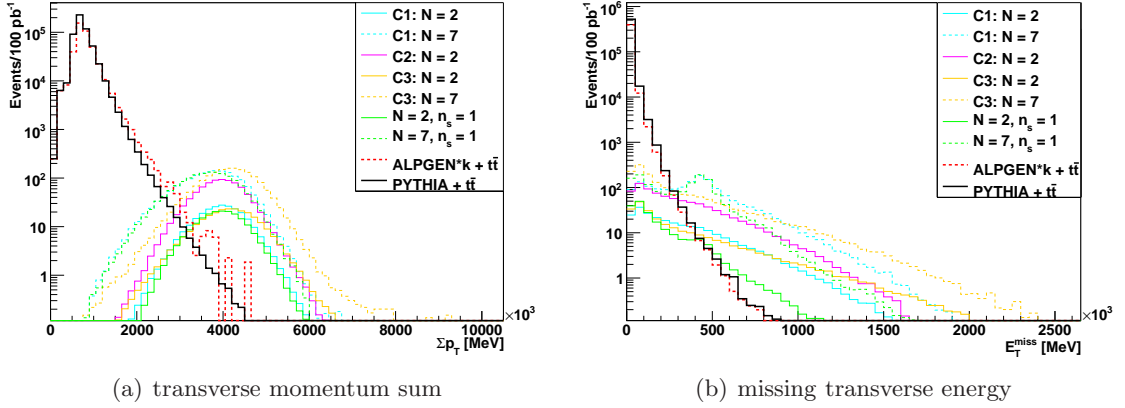


Figure 4.8.: Σp_T (a) and E_T^{miss} (b) distributions for signal and background samples for $\sqrt{s} = 10$ TeV [101].

is shown on the right. The multiplicity prediction for the signal samples now exceeds both background samples.

Figure 4.8 displays on the left the transverse momentum sum for the different black hole scenarios and background samples. Although the rise from values $\Sigma p_T > 1$ TeV and the peak around $\Sigma p_T > 4$ TeV for the signal samples are an effect of the sharp threshold mass during generation, the signals dominate over the steeply falling background distribution. In the missing transverse energy distribution on the right the signal distributions have a longer tail towards high energies. This is mostly due to neutrino and graviton emission.

Taking the knowledge from these distributions it is plausible to require both a high transverse momentum sum and a large multiplicity of high p_T objects to enhance the signal fraction in a data sample and suppress background processes effectively. Black holes are robust against such a selection due to their high production mass and hard transverse momentum spectrum for a large object multiplicity.

5-Object Analysis Strategy

The selection strategies presented before are using key features of black hole signals, namely a high transverse momentum sum and a large multiplicity of objects with high p_T . Both selections additionally rely on the prediction of a significant lepton fraction in the decay process of the black holes. This leads to a bad performance for models with lepton suppression like simulated in the samples d2_n1 and d7_n1. To avoid the dependency on leptons a new approach is taken. The idea is to combine the signal properties of high transverse momentum sum and large multiplicity of high p_T objects. In Figure 4.9(a) the Σp_T distribution is shown. Additionally to the background samples the signal sample d2_n1 with the lowest predicted cross section of all considered samples (compare Table 4.4 and Figure 4.8) is displayed. By requiring $\Sigma p_T > 3.5$ TeV an effective suppression of the background can be achieved while still allowing for a high acceptance of signal events.

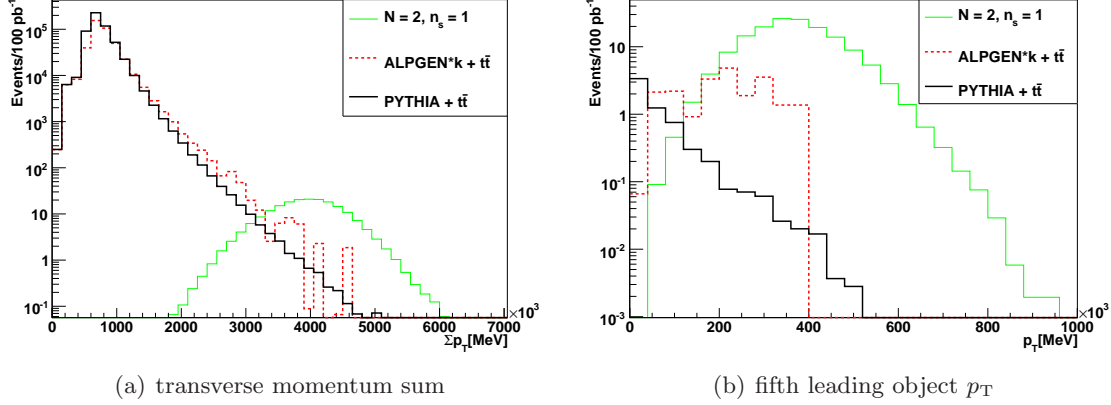


Figure 4.9.: Σp_T (a) distribution for the lowest signal sample and background. p_T spectrum for the fifth leading object (b) after the selection $\Sigma p_T > 3.5$ TeV for $\sqrt{s} = 10$ TeV [101].

Selection	C1_N2	C1_N7	C2_N2	C3_N2	C3_N7	d2_n1	d7_n1
Σp_T and lepton	46%	35%	46%	33%	31%	15%	13%
4 obj incl. lepton	29%	22%	29%	21%	19%	4%	5%
$\Sigma p_T > 3.5$ TeV	79%	62%	79%	82%	83%	79%	59%
5-object selection	70%	49%	71%	55%	58%	72%	47%

Table 4.6.: Signal acceptance of all three selection strategies for the different BLACKMAX samples [101].

Acceptance is defined here as:

$$\text{acceptance} \equiv \frac{\text{number of selected events}}{\text{total number of events}}. \quad (4.2)$$

Figure 4.9 (b) shows the transverse momentum spectrum of the fifth object after requiring $\Sigma p_T > 3.5$ TeV. A requirement of five objects with a transverse momentum of $p_T > 200$ GeV further reduces the background acceptance while the impact on the signal acceptance is small. The combination of both requirements is from now on called 5-object selection. The acceptance for both the previously defined selections as well as this strategy are summarised in Table 4.6 for signal samples and in Table 4.7 for background samples. The performance of the alternative selection is good. The signal acceptance is higher for all scenarios compared to the other selections. Additionally, it shows less dependency on the signal model used. The background suppression is comparable to the other selections. The suppression of the PYTHIA sample is better by one order of magnitude compared to the ALPGEN sample. Overall, the 5-object selection is an improvement in comparison with the other selections.

Selection	$t\bar{t}$	QCD-PYTHIA (J5+)	QCD-ALPGEN (J5+)
$\Sigma p_T > 3.5$ TeV	4.4×10^{-3} %	1.039×10^{-3} %	0.013%
5-object selection	2×10^{-4} %	3.95×10^{-5} %	3.51×10^{-4} %

Table 4.7.: Background acceptance of the 5-object selection strategy for the different background samples [101].

Discovery Potential

For this analysis, the discovery of a signal is defined as

$$\text{significance} \equiv \frac{N_S}{\sqrt{N_B + \sigma_B^2}} \geq 5 \quad (4.3)$$

$$N_S > 10,$$

where $N_{S(B)}$ is the number of signal (background) events after selection, and σ_B is the systematic uncertainty on the background prediction. During early data taking the number is expected to have large systematic uncertainties due to both a bad description of the detector performance and model uncertainties for the background like higher order QCD effects and parton distribution functions. Therefore a systematic uncertainty of 100% is assumed, i.e. $\sigma_B = N_B$.

For a sample corresponding to an integrated luminosity of $\mathcal{L} = 100 \text{ pb}^{-1}$ the expected number of signal (N_S) and background (N_B) events are listed in Tables 4.8 and 4.9. The background prediction from ALPGEN is significantly higher than from PYTHIA. The larger statistical error for ALPGEN is due to the limited size of the generated sample. The calculated significance for both PYTHIA and ALPGEN as background sample is listed in Tables 4.10 and 4.11 for all signal models. The lowest significance is predicted for the split-brane scenario with two extra dimensions (d2_n1). The highest significance is expected for non-rotating black holes in a model with tensionless non-split branes and two extra dimensions (C1_N7).

The performance of the 5-object selection can be seen in Figure 4.10. Here the invariant mass distribution is shown for all events (a) and after the 5-object selection (b). The strong background suppression is clearly visible. The different distribution shape of ALPGEN compared to PYTHIA in Figure 4.10 (b) is probably due the limited statistics for the sample in this kinematic regime.

To estimate the discovery reach for a certain reconstructed invariant mass, a lower invariant mass threshold is necessary. At the same time this threshold can be used to ensure the selection of semi-classical microscopic black holes. Using the predicted significance from Table 4.10 and the invariant mass distributions in Figure 4.10 it is possible to calculate the required integrated luminosity for the discovery of a black hole. This is illustrated in Figure 4.11 with PYTHIA as background sample. With only 10 pb^{-1} of data at $\sqrt{s} = 10$ TeV it should be possible to discover all models simulated for this study with a lower mass threshold of 5 TeV. But since the LHC operates at $\sqrt{s} = 7$ TeV for the first years, an adaptation of the search strategy and a recalculation of the discovery potential is necessary. This is shown in the following.

Selection	C1_N2	C1_N7	C2_N2	C3_N2	C3_N7	d2_n1	d7_n1
$\sum p_T$ and 5 objects	175	797	601	137	951	141	704
$\sum p_T$ and lepton	113	569	39	82	519	28	199
4 obj incl. lepton	73	341	250	53	317	8	69

Table 4.8.: Number of expected signal events (N_S) in 100 pb^{-1} of data at for $\sqrt{s} = 10 \text{ TeV}$ after the different selections strategies for the various black hole scenarios [101].

Selection	$t\bar{t}$	QCD-PYTHIA	QCD-ALPGEN (rescaled)
$\sum p_T$ and 5 objects	0.04 ± 0.03	0.21 ± 0.02	1.35 ± 1.19
$\sum p_T$ and lepton	1.28 ± 0.17	0.01 ± 0.01	10.77 ± 4.09
4 obj incl. lepton	1.37 ± 0.17	0	2.20 ± 2.13

Table 4.9.: Number of expected background events (N_B) in 100 pb^{-1} of data at $\sqrt{s} = 10 \text{ TeV}$ after the different selection strategies [101].

Selection	C1_N2	C1_N7	C2_N2	C3_N2	C3_N7	d2_n1	d7_n1
$\sum p_T$ and 5 objects	676	3066	2314	529	3661	545	2710
$\sum p_T$ and lepton	85	431	300	63	399	21	151
4 obj incl. lepton	53	249	192	39	231	6	50

Table 4.10.: Significance of the different selection strategies for the various black hole scenarios, using the QCD background prediction by PYTHIA. The values are given for 100 pb^{-1} of data at $\sqrt{s} = 10 \text{ TeV}$ [101].

Selection	C1_N2	C1_N7	C2_N2	C3_N2	C3_N7	d2_n1	d7_n1
$\sum p_T$ and 5 objects	95	436	329	75	521	77	386
$\sum p_T$ and lepton	9	46	3	7	42	2	16
4 obj incl. lepton	20	94	69	15	87	2	19

Table 4.11.: Significance of the different selection strategies for the various black hole scenarios, using the QCD background prediction by ALPGEN. The values are given for 100 pb^{-1} of data at $\sqrt{s} = 10 \text{ TeV}$ [101].

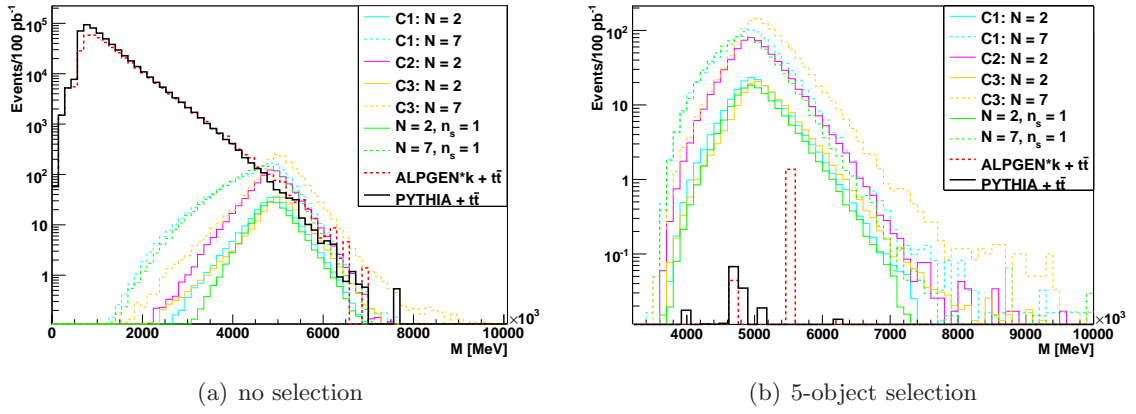


Figure 4.10.: Invariant mass distribution before (a) and after (b) the 5-object selection for $\sqrt{s} = 10$ TeV [101].

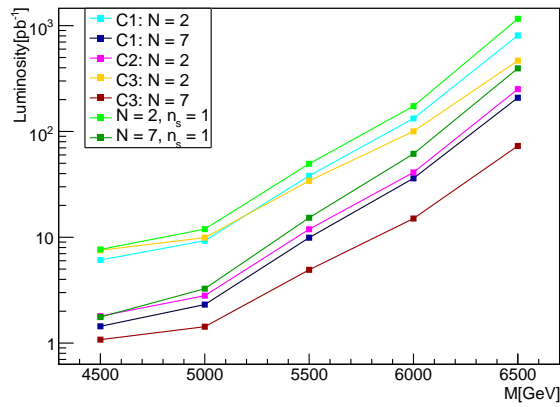


Figure 4.11.: Required integrated luminosity at $\sqrt{s} = 10$ TeV for the discovery of a black hole for different model scenarios [101].

n	M_D [TeV]	M_{th}	σ [pb]
2	1.0	5.0	3.19×10^{-3}
3	1.0	5.0	5.38×10^{-3}
4	1.0	5.0	7.60×10^{-3}
5	1.0	5.0	9.98×10^{-3}
6	1.0	5.0	1.26×10^{-2}
7	1.0	5.0	1.49×10^{-2}

Table 4.12.: Signal samples for $\sqrt{s} = 7$ TeV. Listed are the number of extra dimensions n , the Planck mass M_D , the minimum threshold mass M_{th} and the production cross section σ .

4.4. Adaptation for $\sqrt{s} = 7$ TeV

A similar study as for a centre-of-mass energy of $\sqrt{s} = 10$ TeV is done for the LHC beam energy which is available for the first years of data taking, $\sqrt{s} = 7$ TeV. A slightly different approach to determine robust selections is taken, and the signal and background samples differ as well. This study is described in the following.

Signal Samples

Due to the lower centre-of-mass energy of $\sqrt{s} = 7$ TeV, the cross section for black hole production is suppressed compared to $\sqrt{s} = 10$ TeV for the same scenario. To reach a minimum mass of e.g. $M_{\text{th}} = 5$ TeV requires the Bjorken x to be high for both partons, which is unlikely following PDF predictions. Therefore a scenario with high production cross section is chosen. It is equivalent to the third sample type from the previous study ("C3"). BLACKMAX is used to simulate rotating black holes within a model of extra dimensions with tensionless, non-split brane. The number of extra dimensions ranges from two to seven. The different samples with corresponding cross sections are listed in Table 4.12.

Background Samples

The background samples used for this analysis are listed in Table 4.13. The dominant background source is QCD jet production. Figure 4.12 shows the invariant mass distributions of the background processes. The left distribution compares the two QCD jet production samples generated with PYTHIA and ALPGEN. For $M_{\text{inv}} < 2$ TeV the two predictions deviate by up to 50%. Since the signal region is well above $M_{\text{inv}} < 2$ TeV, this has no impact on the background prediction. For higher masses both predictions agree within their statistical uncertainties. Especially ALPGEN is limited in statistics for high mass states. The right figure shows the contribution from the different background processes to the mass spectrum. Due to the higher cross section QCD jet production clearly dominates over the other processes, $t\bar{t}$, W + jets and Z + jets. Only for high masses ($M_{\text{inv}} > 4$ TeV) $t\bar{t}$ production contributes significantly. In the following, all shown distributions use a combined sample of all included background processes, using PYTHIA for QCD jet production, if not otherwise stated.

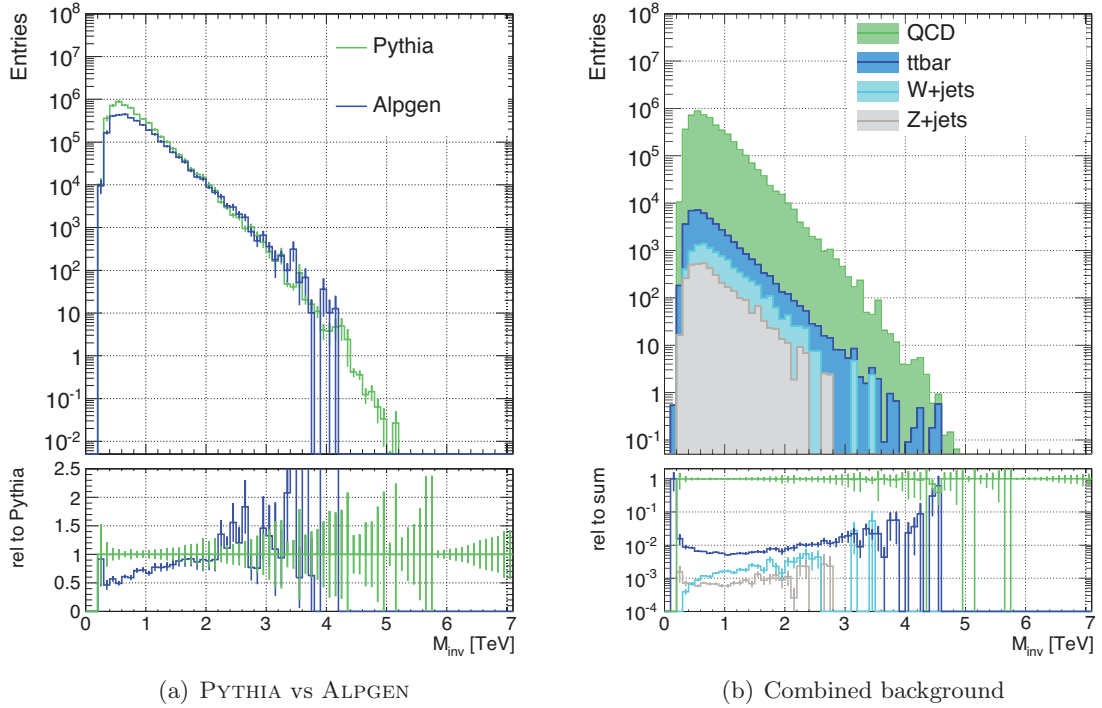


Figure 4.12.: Invariant mass distribution for $\sqrt{s} = 7$ TeV for QCD jet production for an integrated luminosity of $\mathcal{L} = 1 \text{ fb}^{-1}$ with PYTHIA and ALPGEN (a) and for the combination of all included background processes (b). The displayed uncertainties correspond to the limited statistics of the available sample.

Process	Event generator	Cross section [pb]
QCD ($p_T > 8 \text{ GeV}$)	PYTHIA	1.06×10^{10}
QCD ($p_T > 15 \text{ GeV}$)	ALPGEN	3.14×10^8
$t\bar{t}$	MC@NLO	1.65×10^2
Z+jets ($p_T > 20 \text{ GeV}$)	HERWIG	4.13×10^3
W+jets ($p_T > 20 \text{ GeV}$)	HERWIG	3.14×10^4

Table 4.13.: Background processes with event generator, cross section, and the cut on the leading parton p_T .

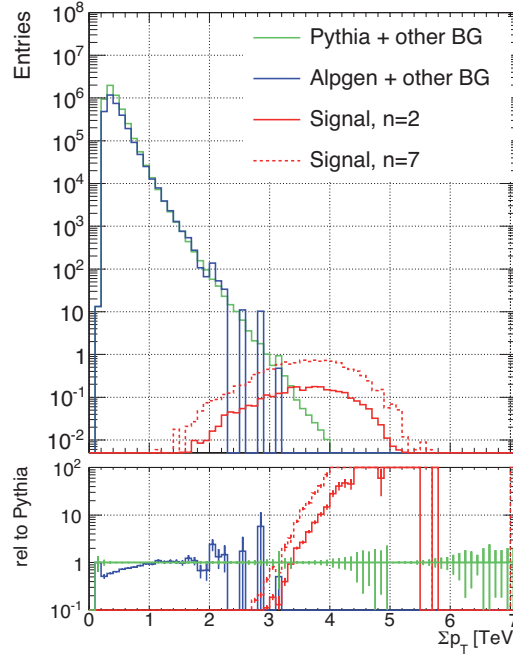


Figure 4.13.: Scalar sum of transverse momenta of all objects for background and two different signal samples with $n = 2(7)$ extra dimensions for an integrated luminosity of $\mathcal{L} = 1 \text{ fb}^{-1}$ at $\sqrt{s} = 7 \text{ TeV}$.

Object Selection

For this study samples with full detector simulation and reconstruction are available. This allows for a more detailed description of detector effects and is also used for analyses of experimental data taken with the ATLAS experiment. The general description of the ATLAS object reconstruction for early data is given in Chapter 3.3. Since for this analysis the different types and flavours of final state particles are not evaluated, they are commonly referred to as objects. Jets, electrons, photons and muons are used as objects. The missing transverse energy E_T^{miss} is used for calculations but is not counted as object. The transverse momentum sum Σp_T and the invariant mass M_{inv} are used as defined in Chapter 3.

Distributions

Kinematic distributions are shown in the following. All samples are normalised to an integrated luminosity of $\mathcal{L} = 1 \text{ fb}^{-1}$. Figure 4.13 shows the scalar sum of the transverse momenta of all objects. The predictions from PYTHIA and ALPGEN differ strongly for lower values ($\Sigma p_T < 1 \text{ TeV}$). For higher values of Σp_T the agreement is good. For $\Sigma p_T > 2 \text{ TeV}$ the statistics for the ALPGEN sample is low. The predictions for the two displayed signal samples with $n = 2$ and $n = 7$ extra dimensions set in at $\Sigma p_T \approx 1.5 \text{ TeV}$ and become comparable to the background at $\Sigma p_T \approx 3 \text{ TeV}$. For higher values of Σp_T the signal dominates clearly. The distributions for the BLACKMAX samples fall again steeply after reaching their peak

around $\Sigma p_T \approx 4 \text{ TeV}$. This peak is an artefact created by the threshold mass requirement of $M_{\text{th}} = 5 \text{ TeV}$ during event generation for the used samples. A higher (lower) value of M_{th} would produce an later (earlier) peak of the distribution.

The transverse momenta of the five leading objects are shown in Figure 4.14. The agreement of the background prediction from PYTHIA and ALPGEN is good for all five distributions. The spectrum becomes significantly softer after the second leading object. The number of events with sufficient object multiplicity also drops off quickly for the background. In contrary the spectra for the displayed signal samples with $n = 2$ and $n = 7$ extra dimensions also become softer, but the number of events represented by the area under the curve is not as affected by the multiplicity requirement for the signal as for the background. This allows for an effective background reduction by selection criteria based on the transverse momentum sum and the multiplicity of high p_T objects as elaborated in the following.

Strategy

A discovery requirement is defined in Eq. (4.4). For the determination of optimal selection criteria a different significance definition is used. In this case the significance is defined as follows:

$$S \equiv \sqrt{N_S \cdot \frac{N_S}{N_B + N_S}}, \quad (4.4)$$

with N_S as number of signal events and N_B as number of background events remaining after a selection. It is well defined for selections with no remaining background events. This is advantageous for an optimisation of the selection, since it allows for a systematic variation of selection criteria.

This method is used for the two variables already defined in the previous study for $\sqrt{s} = 10 \text{ TeV}$, the transverse momentum sum Σp_T and the transverse momentum of the fifth leading object $p_T^{(5)}$. Figure 4.15 shows the event distribution with respect to both variables. The displayed background sample is the combined background prediction from PYTHIA and the other processes, while the signal sample is based on the model with $n = 2$ extra dimensions, chosen because it has the lowest cross section of the used samples. The number of events in a bin is represented by the size of the boxes on a logarithmic scale. For small values of Σp_T and $p_T^{(5)}$ only background events are visible. After a large overlap zone with $2 \text{ TeV} \lesssim \Sigma p_T \lesssim 4 \text{ TeV}$ the signal dominates.

To find the optimal selection parameter for the two variables a systematic variation is done. For each possible combination of minimum Σp_T and minimum $p_T^{(5)}$, κ as defined above (4.4) is calculated for all considered signal samples. The step width is $\Delta \Sigma p_T = 100 \text{ GeV}$ and $\Delta p_T^{(5)} = 10 \text{ GeV}$. The resulting distribution for the lowest signal sample with $n = 2$ extra dimensions is shown in Figure 4.16. The left distribution shows an overview over a large parameter space. The contours show κ on a linear scale. The maximum corresponds to the optimal selection parameter. The right plot shows a zoom of the maximum's area. The maximum is determined for all signal samples. The resulting selection parameter are listed in Table 4.14. The chosen parameter are $\Sigma p_T = 3 \text{ TeV}$ and $p_T^{(5)} = 150 \text{ GeV}$, corresponding to the strictest determined values. The resulting selection is also displayed in the right figure. The shaded area represents the signal region after the selection.

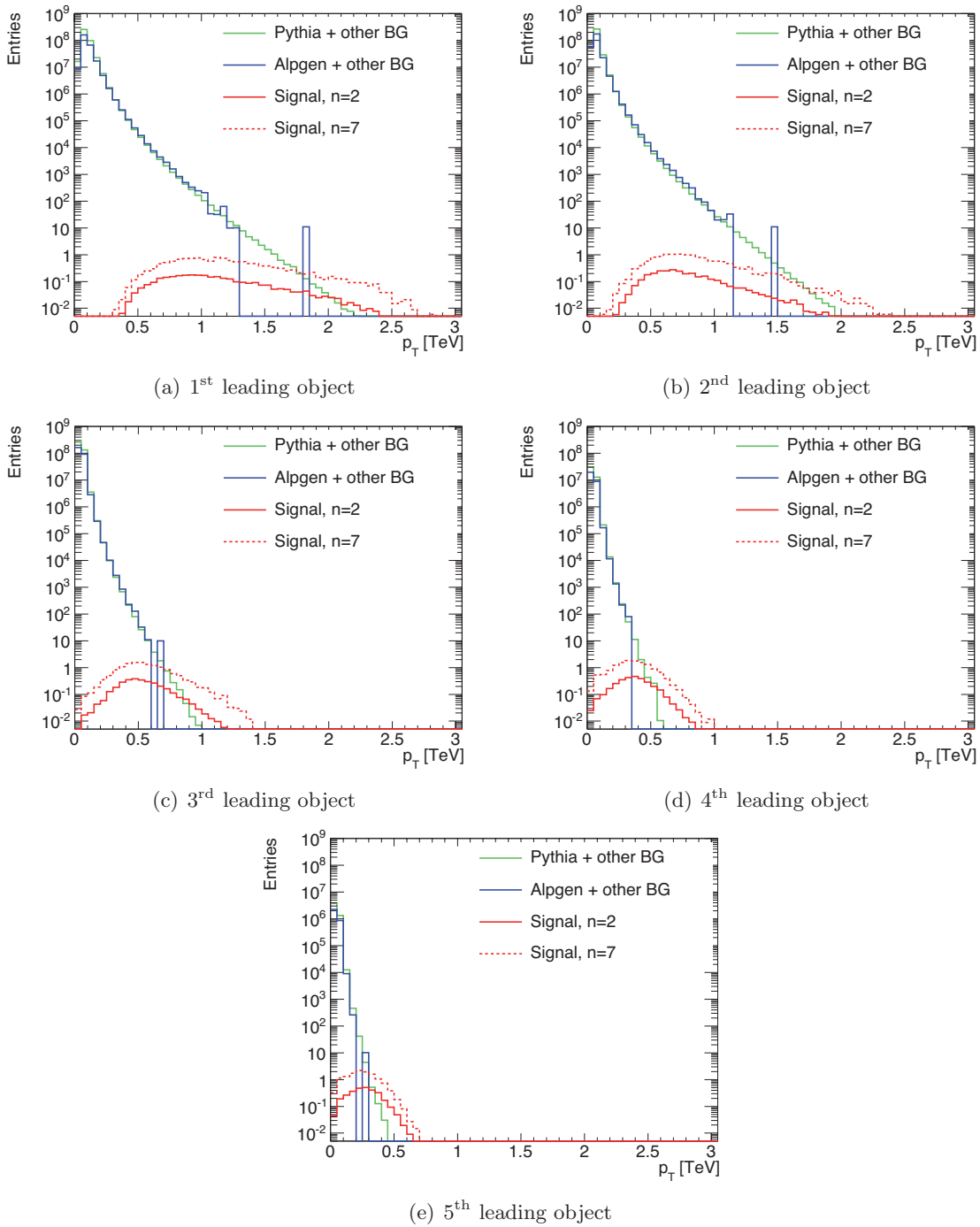


Figure 4.14.: Transverse momentum p_T of the 1st (a) to 5th (e) leading object. The number of events corresponds to an integrated luminosity of $\mathcal{L} = 1 \text{ fb}^{-1}$ at $\sqrt{s} = 7$ TeV. Displayed are only statistical uncertainties.

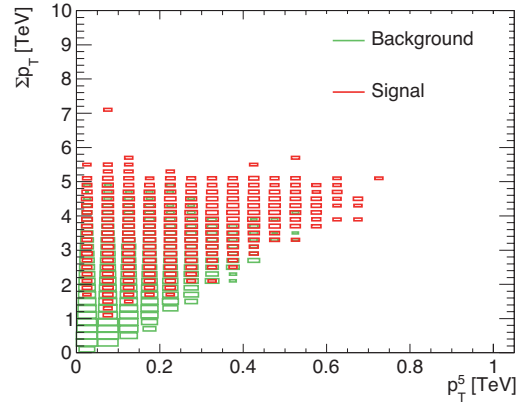


Figure 4.15.: Event distribution of the transverse momentum p_T of the 5th leading object versus the transverse momentum sum Σp_T for background and one signal sample with $n = 2$ extra dimensions. Both samples are scaled according to their cross section at $\sqrt{s} = 7$ TeV. The size of the boxes corresponds to the number of entries in a bin on a logarithmic scale.

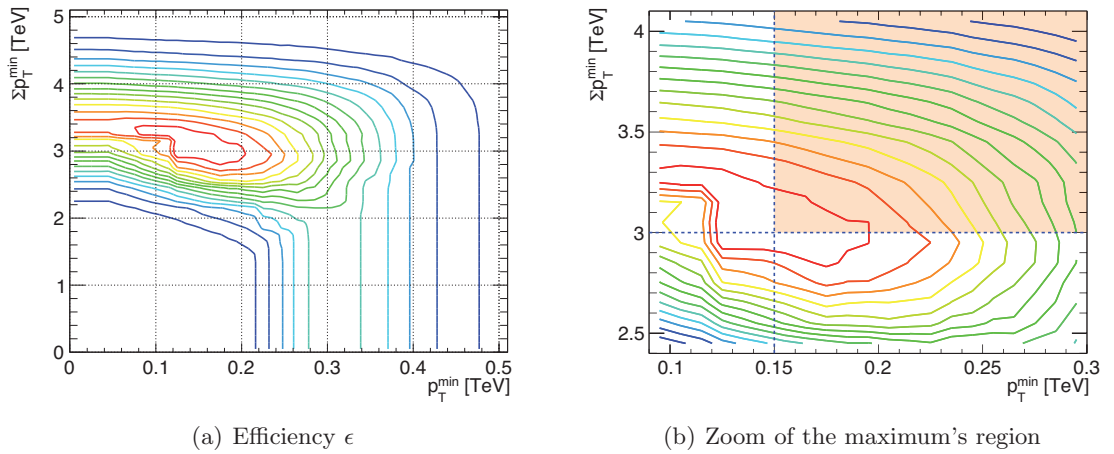


Figure 4.16.: Efficiency ϵ as a function of Σp_T and $p_T^{(5)}$ for a signal sample with $n = 2$ extra dimensions and PYTHIA plus other background processes. The contours show S on a linear scale for $\mathcal{L} = 1 \text{ fb}^{-1}$ at $\sqrt{s} = 7$ TeV. The shaded area displays the selected signal region.

n	Σp_T [TeV]	$p_T^{(5)}$ [GeV]
2	3.0	150
3	3.0	150
4	3.0	150
5	2.9	150
6	2.9	150
7	2.9	150

Table 4.14.: Selection parameter for different signal samples with $n = 2$ to $n = 7$ extra dimensions.

process	QCD jet PYTHIA	QCD jet ALPGEN	$t\bar{t}$	W +jets	Z +jets
Acceptance	5.0×10^{-6} %	0.0 %	0.0 %	0.0 %	0.0 %
Events [1/fb $^{-1}$] (stat.)	0.25 ± 0.05	0	0	0	0

Table 4.15.: Acceptance and number of expected events for background processes. The number of events is given for an integrated luminosity of $\mathcal{L} = 1$ fb $^{-1}$.

The effect on the background samples can be seen in Table 4.15. The acceptance for the PYTHIA QCD jet production sample is 5.0×10^{-6} %. This number is not directly comparable with the result from the study with $\sqrt{s} = 10$ TeV, since the p_T range of the samples is extended to lower values in this study (compare Tables 4.5 and 4.13). This leads to different kinematic distributions, which makes a direct comparison of a relative measure like the acceptance impossible. The number of expected events for $\mathcal{L} = 1$ fb $^{-1}$ after the selection is 0.25 ± 0.05 . For all other samples, including ALPGEN, there is no event left after the selection. This result is due to missing statistics in the high Σp_T region for these samples. Following the distributions shown before the contribution from other background processes is expected to be small, at most in the order of the PYTHIA prediction. For the following calculations the number of expected events from PYTHIA is used.

The acceptance for the signal samples is listed in Table 4.16. It is stable between 66 % and 69 % for the considered signal models. The resulting number of expected events for an integrated luminosity of $\mathcal{L} = 1$ fb $^{-1}$ is therefore only influenced negligibly from the acceptance. The main dependency is on the production cross section for a certain model. Since the cross section is rising with the number of extra dimensions (compare Table 4.12) the number of expected events also rises from 2 to 8 events for $n = 2$ to $n = 7$ extra dimensions.

For a determination of the discovery reach, the definition for the discovery of a black hole from the study for $\sqrt{s} = 10$ TeV, given in Equation 4.4, is used. The required integrated luminosity can be calculated with the given results. It is listed in Table 4.16. It ranges from 1.2 fb $^{-1}$ to 5.0 fb $^{-1}$ for models with $n = 2$ to $n = 7$ extra dimensions. This exceeds the luminosity goal of 1 fb $^{-1}$ for the whole data taking period up to the end of 2011.

n	2	3	4	5	6	7
Acceptance	68.7 %	68.7 %	67.8 %	66.9 %	65.1 %	66.4 %
Events [1/1 fb ⁻¹]	2.00	3.35	4.55	5.81	6.97	8.40
(stat.)	±0.04	±0.06	±0.08	±0.11	±0.13	±0.16
Significance [1/1 fb ⁻¹]	3.6	6.0	8.1	10.3	12.4	14.9
required \mathcal{L} [fb ⁻¹]	5.0	3.0	2.2	1.7	1.4	1.2

Table 4.16.: Acceptance, number of expected events and expected significance for BLACKMAX signal samples with $n = 2$ to $n = 7$ extra dimensions. The number of events and significance are given for an integrated luminosity of $\mathcal{L} = 1 \text{ fb}^{-1}$.

4.5. Summary

This chapter describes possible search strategies for black holes. The first search strategies developed for microscopic black holes at $\sqrt{s} = 14 \text{ TeV}$ rely on a significant abundance of high p_T leptons in the particle spectrum of the black hole. The determined strategies are $\Sigma p_T > 3.5 \text{ TeV}$ including a lepton with $p_T > 50 \text{ GeV}$ and alternatively at least four objects with $p_T > 200 \text{ GeV}$ and a lepton with $p_T > 200 \text{ GeV}$ [99]. The trigger behaviour of black holes was studied for this strategy analysis in the wourse of this work. An unrescaled single jet trigger with a threshold of up to 400 GeV is shown to be fully efficient for microscopic black holes. For $\sqrt{s} = 10 \text{ TeV}$, a study [101] is presented avoiding the lepton requirement. It uses the transverse momentum sum and the transverse momentum of the fifth leading object. The proposed selection criteria are $\Sigma p_T > 3.5 \text{ TeV}$ and $p_T^{(5)} > 200 \text{ TeV}$. With this selection an estimation is made of the required luminosity for a black hole discovery. With 10 pb^{-1} of $\sqrt{s} = 10 \text{ TeV}$ data a discovery is possible. For this study, the sample generation, the selection strategy development and the discovery reach were contributed in the course of this work.

Since the LHC is operated at $\sqrt{s} = 7 \text{ TeV}$ for the first years, the study is updated. A new study is presented which takes into account the changed running conditions. It uses fully simulated samples for different background processes and signal samples at the present centre-of-mass-energy. A different approach is suggested to determine the optimal selection parameter for a set of selection variables. With this method the previously used variables Σp_T and $p_T^{(5)}$ are optimised. The resulting selection parameters are $\Sigma p_T > 3.0 \text{ TeV}$ and $p_T^{(5)} > 150 \text{ TeV}$. The acceptance for the considered signal samples is between 66 % and 69 %. The acceptance for the background processes is $5.0 \times 10^{-6} \%$. Due to the lower production cross section for $\sqrt{s} = 7 \text{ TeV}$ a discovery of a black hole produced within any considered model is not to be expected with the targeted integrated luminosity of 1 fb^{-1} until the end of 2011. Therefore a different approach is presented in the following chapter, aiming at low scale gravity effects with discovery potential in early data.

5. Search for Multi-Object Final States

In the previous chapter it is shown, that semi-classical black holes are not within the search reach for early data at the LHC with $\sqrt{s} = 7 \text{ TeV}$. The predicted production cross section in a semi-classical regime for energies considerably higher than the Planck mass M_{D} is too low. However, other manifestations of gravitational interactions may show up at energies close to M_{D} . Here the semi-classical assumption is not valid and due to the lack of a consistent theory of quantum gravity the available models have only limited predictive power. Thus an inclusive search strategy is deployed to cover a broad range of signal scenarios. This analysis is presented in this chapter.

The data sample, recorded with a collision energy of $\sqrt{s} = 7 \text{ TeV}$, is described in Section 5.1. The properties of potential signal signatures motivate the chosen search strategy and object definitions. This is outlined in Sections 5.2 and 5.3. Based on the selection criteria possible background processes are identified and analysed. With this knowledge a suitable background estimation method is established. The study of uncertainties based on background simulations and data properties is described in Section 5.5. An upper limit on cross section times acceptance is then derived using a Bayesian approach. For different signal models an acceptance calculation is shown in Section 5.7. The chapter ends with a discussion of the results and its impact on models of low scale gravity.

5.1. Early Data Taking in 2010

The dataset used for this analysis was taken in the period from March to July 2010. It contains the very first data taking periods recorded at 7 TeV centre-of-mass energy suitable for physics analysis. The data taking period is split into runs with stable conditions of beam and detector. The instantaneous luminosity was increasing from run to run. The peak luminosity varied between $9.9 \times 10^{26} \text{ cm}^{-2} \text{ s}^{-1}$ and $1.6 \times 10^{30} \text{ cm}^{-2} \text{ s}^{-1}$. The collected integrated luminosity developing over the run period is shown in Figure 5.1. The effect of the rising instantaneous luminosity on the collected amount of data can clearly be seen. The whole dataset corresponds to an integrated luminosity of $\mathcal{L} = 297 \text{ nb}^{-1}$. The uncertainty on the luminosity is 11 % as described before [77]. Due to the low instantaneous luminosity in the beginning of data taking it was possible to run with unprescaled triggers and only select with the Level 1 trigger. With rising luminosity prescales were applied on low threshold L1 triggers. The lowest single jet trigger unprescaled over the whole run period was L1J15.

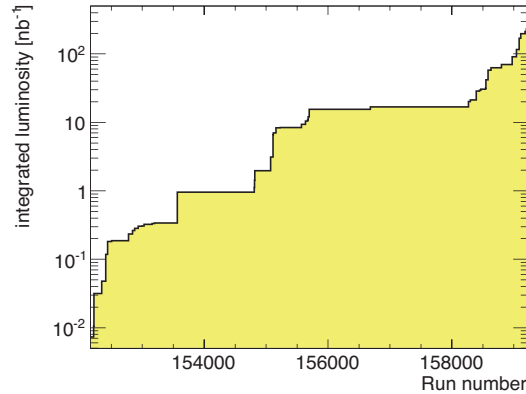


Figure 5.1.: Integrated luminosity in the data taking period after data quality selection.

5.2. Signal and Backgrounds

Signal Signatures

As shown in Chapter 2 there is no reliably motivated physics model for low scale gravity effects close to the fundamental Planck mass M_D . Especially the formation and decay of black holes is difficult to describe in this energy region.

Therefore a more general approach is taken. Instead of relying on predictions from certain models a model independent search within the context of low scale gravity is deployed. The basic features of signals in this regime of new physics are supposed to be still valid. A potential signal has a high invariant mass decaying into many objects with high transverse momentum p_T , thus resulting in a high transverse momentum sum Σp_T .

Although a proper theoretical description is missing, Black Hole Monte Carlo generators can still be used to derive basic kinematic distributions similar to a potential signal. The established production and decay mechanisms for the semi-classical regime are applied to black holes with smaller production masses. In this case the main decay is governed by the final burst. The basic principles used should still be viable in this low transplanckian regime, although some aspects, especially the cross section calculations, are speculative. Using previously set limits from other collider experiments, which were discussed before, the lowest allowed value considered for the Planck mass is $M_D = 0.8$ TeV. For simplicity, the fundamental Planck scale M_D and the black hole threshold mass M_{th} are chosen identically. The two black hole Monte Carlo generators CHARYBDIS and BLACKMAX are used to generate signal samples with $M_D = M_{th} = 0.8$ TeV, 1.0 TeV, 1.2 TeV. More details on the event generation are given later.

Background

Standard Model processes can also create final states with high M_{inv} , large multiplicity and high Σp_T . The most prominent processes are the production of QCD jets, $t\bar{t}$, $W +$ jets and $Z +$ jets.

The considered background samples are listed in Table 5.1. The cross section for QCD jet

production is many orders of magnitude larger compared to the other processes, and thus constitutes the main background. A more detailed assessment of this point is done at a later stage. QCD jet production for this analysis is described by the Monte Carlo generators ALPGEN[90] and PYTHIA[80]. Details of the generators are given in Chapter 2.

The performance of both generators with respect to Standard Model measurements is described in the same chapter. Studies of the inclusive jet cross section [103] show a good agreement between data and MC prediction from PYTHIA. For multi-jets, the predictions from both generators fit the experimental data results remarkably well [104]. ALPGEN nominally describes multi object final states, but also PYTHIA, with only two hard jets in the final state, manages to produce a matching multi-jet spectrum shape via initial and final state radiation.

Process	Event generator	Cross section [pb]
QCD ($p_T > 8$ GeV)	PYTHIA	1.06×10^{10}
QCD ($p_T > 15$ GeV)	ALPGEN	3.14×10^8
$t\bar{t}$	MC@NLO	1.65×10^2
Z+jets ($p_T > 20$ GeV)	HERWIG	4.13×10^3
W+jets ($p_T > 20$ GeV)	HERWIG	3.14×10^4

Table 5.1.: Background processes with event generator, cross section, and the cut on the leading parton p_T .

5.3. Search Strategy

New physics in the context of low-scale gravity is expected to show one of the distinct features of gravity, namely its coupling to all particles. This property is reflected in the democratic decay of black holes as described in Chapter 2. Therefore objects are defined inclusively without distinction between different particle types or flavours. Jets, electrons, photons and muons are commonly referred to as objects. The general description of the ATLAS object reconstruction for early data is given in Chapter 3.3. The missing transverse energy E_T^{miss} is used for calculations but is not counted as an object.

Strategy

As mentioned earlier, the most prominent features of the signature are high mass final states with a large multiplicity of objects with high p_T and thus a high Σp_T . These final state properties common to most models in the context of low-scale gravity enable an inclusive search strategy. Such a strategy is designed to discover any kind of new physics already with early data, where the acquired statistics is too low to do a study as discussed in Chapter 4. If no signal excess over the background prediction is found, a limit on the cross section times acceptance can be derived. The acceptance is a function of the signal model (see Section 5.7). Based on the above object definition the basic selection criterion is a final state with at least

three particles. This suppresses pure di-jet final states and is the most inclusive way of requiring a multi-object final state.

$$N_{\text{obj}} \geq 3 \quad (5.1)$$

The signal region is defined using an M_{inv} and Σp_{T} threshold. For this analysis it is set to

$$M_{\text{inv}} \geq 800 \text{ GeV} \quad \text{and} \quad \Sigma p_{\text{T}} \geq 700 \text{ GeV}. \quad (5.2)$$

The invariant mass requirement ensures the selection of events with a reconstructed mass above the lowest fundamental Planck mass, which is not excluded by other collider experiments. The transverse momentum sum requirement enriches events with central objects, thus suppressing QCD jet production.

By counting the events in the signal region and comparing it to the number of events expected from pure Standard Model processes it is possible to find signs of new physics.

Background Normalisation

First measurements of di-jet [103] and multi-jet [104] final states have shown a reasonable agreement with QCD MC in the transverse momentum spectrum of jets. Also the distributions in pseudo-rapidity agree well in shape, as can also be seen in Figure 5.8. Therefore it is feasible to rely on the shape of the M_{inv} distribution to extract a possible signal above the QCD background. The MC predictions are normalised to the number of events in a control region. This control region is chosen in a similar kinematic regime to the signal region while providing sufficient statistics and avoiding a contamination from a possible signal. For this analysis the control region is defined by

$$300 \text{ GeV} \leq M_{\text{inv}} \leq 800 \text{ GeV} \quad \text{and} \quad \Sigma p_{\text{T}} \geq 300 \text{ GeV}. \quad (5.3)$$

Details on the choice of the control region can be found in Section 5.5. A visualisation of control and signal region is shown in Figure 5.2. The contours represent the number of events on a logarithmic scale as a function of Σp_{T} and M_{inv} . The shaded areas illustrate the control and signal region borders. The same shading and color coding is used in the following distributions to emphasize control and signal region, where applicable.

Data Quality Selection

Since the objects used in this analysis are identified using all major components of the detector, the requirements for the running conditions are strict. First of all, the beam conditions must be stable. The inner detector, calorimeters, muon system, trigger system and magnet system are required to be in good state as defined by the data quality group of ATLAS. If an event is recorded with insufficient data quality conditions it is rejected.

Trigger

The final state is expected to have many jets with high p_{T} . Hence, the lowest unrescaled single jet trigger is chosen for this analysis. For this data sample this trigger is called L1J15

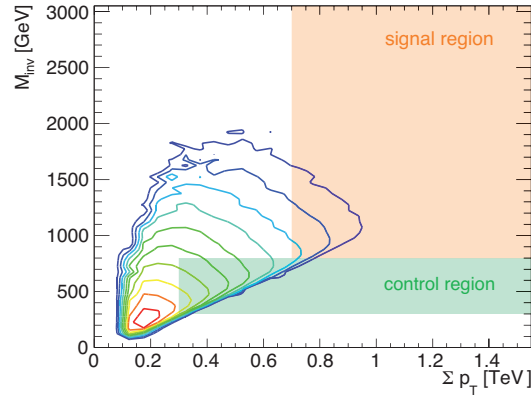


Figure 5.2.: Visualisation of control and signal region. The shown kinematic distribution is using PYTHIA QCD jet production MC. The contours represent the number of events on an arbitrary logarithmic scale.

and is fully efficient for jets with $p_T > 60$ GeV (see Figure 3.11). Since it is a calorimeter based trigger, it is also sensitive to electrons and photons, but not to muons. To avoid any loss of events a single muon trigger with a threshold of 10 GeV is taken as a control trigger in a separate study. No additional events from this trigger pass the event requirements, thus the jet trigger is a save choice for this analysis. The trigger is fully efficient for this analysis for two reasons. The Σp_T requirement of 300 GeV (700 GeV) for the control (signal) region strongly favours high p_T jets which are above the efficiency threshold of 80 GeV for this trigger. Furthermore, the multi object requirement leads to an increase of the event selection efficiency compared to the single jet efficiency.

$$\epsilon_{3\text{jets}} = 1 - (1 - \epsilon_{1\text{jet}})^3 \quad (5.4)$$

If the efficiency for a single jet with $p_T = 40$ GeV is $\epsilon_{1\text{jet}} = 65\%$ (compare Figure 3.11), then the combined efficiency for three jets with the same transverse energy is already $\epsilon_{3\text{jet}} > 95\%$. The combination of both effects leads to the save assumption of a fully efficient trigger. As a cross-check in data, events selected by the lowest jet trigger L1J5 are studied. This trigger is fully efficient for jets with $p_T = 40$ GeV, but it is prescaled for most of the data taking period. After requiring $N_{\text{obj}} \geq 3$ and $\Sigma p_T > 300$ GeV, there are 627 events left which are triggered by L1J5. All of these events are also triggered by L1J15, thus yielding a 100% efficiency. The uncertainty on the efficiency is determined using an approach explained elsewhere [105]. For $N = 627$ events it gives

$$\sigma = \sqrt{\frac{N+1}{(N+3)(N+2)^2}} = 0.16\%. \quad (5.5)$$

Vertex

The beam running conditions determine a nominal collision point close to the centre of the detector. Since the protons are spread within the bunches, the primary vertex of collision

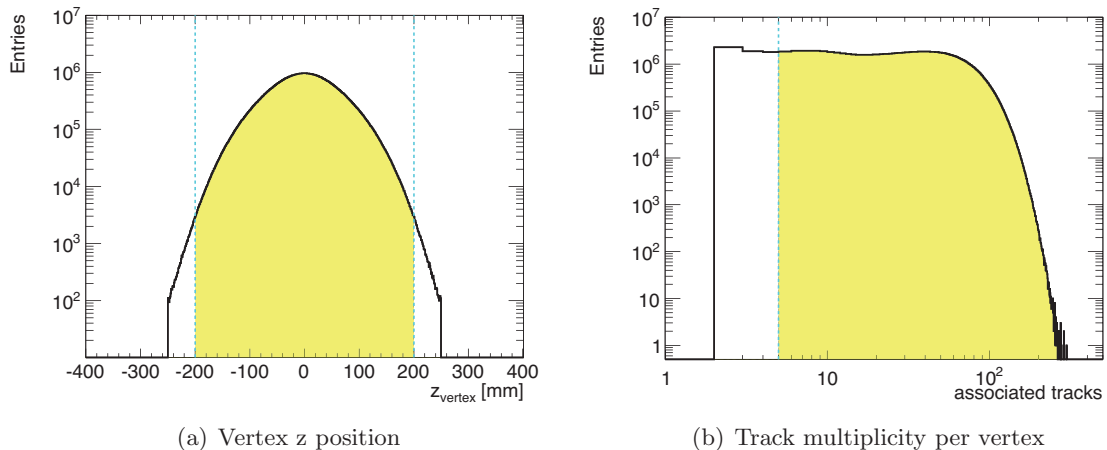


Figure 5.3.: Vertex distributions in the data sample corresponding to a luminosity of $\mathcal{L} = 297 \text{ nb}^{-1}$. The dashed line shows the selection criterion, and the filled area the vertices passing the selection.

events is distributed around the nominal collision point. A typical vertex position distribution is shown in Figure 5.3 (a). Tracks reconstructed in the inner detector are associated to identified vertices. The number of associated tracks to a vertex is illustrated in Figure 5.3 (b). To reject events from beam gas interactions or cosmic showers a primary vertex is required with

- at least 5 tracks associated to this vertex
- a z position close to the nominal interaction point: $|z_{\text{vtx}} - z_{\text{beamspot}}| < 200 \text{ mm}$

The selections are illustrated in Figure 5.3. The shaded areas represent the vertices passing the selection. There is no veto for multiple primary vertices in an event, also called pile-up vertices. From all events passing the trigger requirement, 99% pass the vertex selection.

Pile-Up Events

The instantaneous luminosity was increased during the considered data taking period. An increase of the number of pile-up events is visible, if the number of protons per bunch is increased or the beam diameter is reduced. Figure 5.4 (a) shows the average number of vertices per event $\langle N_{\text{vtx}} \rangle$ as a function of the run number. The error bars denote the spread of the distribution for each run. Since events are only counted if at least one vertex is found, the minimum average number is one. The first change of running conditions was after run 153565. Here a slight increase in $\langle N_{\text{vtx}} \rangle$ is visible. A second change was applied after run 156682. Afterwards, the average number of vertices per event was about 1.5.

The effects of pile-up are expected to contribute mainly in the low- p_T region, and should be suppressed by the requirement of $p_T > 40 \text{ GeV}$ for jets. Figure 5.4 (b) shows the number of events in the control region per integrated luminosity for the individual runs in the data

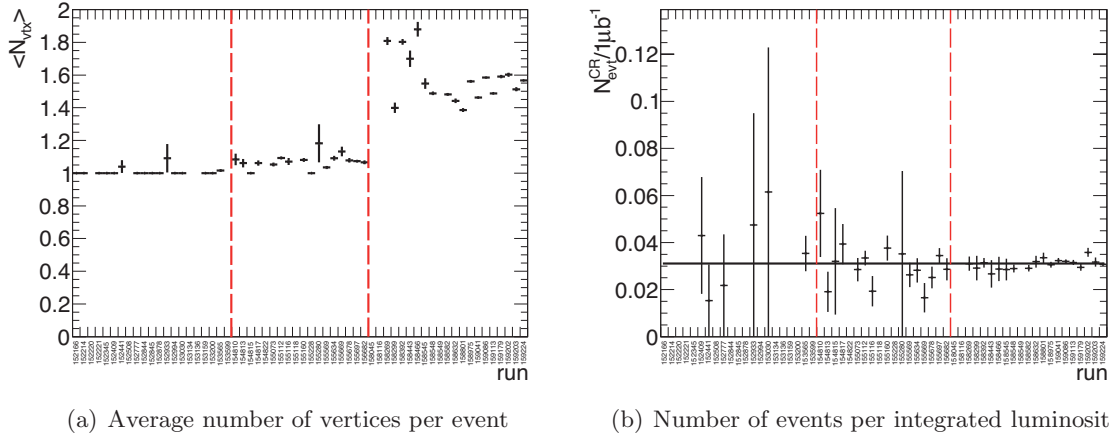


Figure 5.4.: Average number of vertices per event (a) and number of events per integrated luminosity (b). Both are shown as a function of the run in the considered data taking period with an integrated luminosity of $\mathcal{L} = 297 \text{ nb}^{-1}$.

Criteria	Events
total	7 945 734
vertex	7 864 819
event cleaning	7 838 578
$N \geq 3$	92 686
$\Sigma p_{\text{T}} > 300 \text{ GeV}$	11 679
control region	9223
$\Sigma p_{\text{T}} > 700 \text{ GeV}$	200
signal region	194

Table 5.2.: Data events after the different selection steps. The total number of events is given after data quality and trigger selection.

taking period. The number of events is stable for all runs within the statistical uncertainty. Hence, it can be concluded that pile-up has no measurable effect on this analysis.

Event Cleaning

To avoid effects from jets which are identified as fake or wrongly measured, events containing such jets are rejected. The procedure is described in Section 3.3.1. From all events after the vertex requirement, 99.7% pass the event cleaning selection.

The effects of the above described selection steps on the data sample with $\mathcal{L} = 297 \text{ nb}^{-1}$ is summarised in Table 5.2. The biggest reduction results from the three object requirement. In the control region are 9223 events found. After all steps a total of 194 events is counted in the signal region.

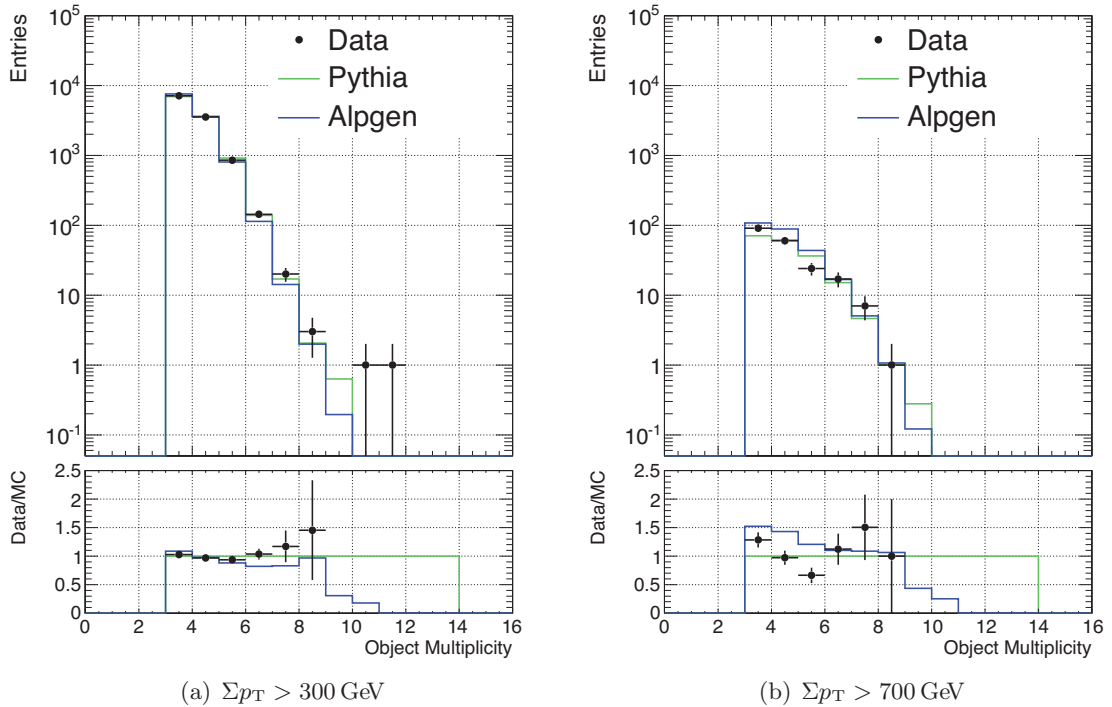


Figure 5.5.: Object multiplicity for events passing the selection criteria. The shown MC distributions are normalised to the number of data events in the control region.

5.4. Kinematic Properties

Kinematic properties have been studied after the basic object, trigger and vertex selections and the requirement of at least 3 objects. The distributions are displayed in Figures 5.5 to 5.8. They show a good agreement between data and the Monte Carlo prediction. The results in the data sample are compared to the QCD jet production samples produced with PYTHIA and ALPGEN. All MC samples are normalised to the number of events in the control region. Figure 5.5 shows the object multiplicity after requiring a transverse mass sum of $\Sigma p_T > 300$ GeV (a) and $\Sigma p_T > 700$ GeV (b), respectively. Both distributions peak at a multiplicity of three. For the higher Σp_T requirement the distribution is less steeply falling compared to the lower Σp_T requirement. Since the object p_T distribution is steeply falling (see Figure 5.7), events with low multiplicity and relatively low p_T objects are most probable, but suppressed by the high Σp_T requirement. The highest observed object multiplicity is 11(9) for $\Sigma p_T > 300(700)$ GeV. No significant deviations from both MC samples are visible. Only in the multiplicity distribution with high Σp_T , data and the Monte Carlo predictions are not in agreement within the statistical uncertainty of data for low multiplicities.

Figure 5.6 shows the composition of object types. Already with no Σp_T requirement the sample is clearly dominated by jets. Only about 0.1% of the objects are either electrons, photons or muons. For higher transverse momentum sum requirements this ratio stays roughly constant, while the total number of events drops. For $\Sigma p_T > 300$ GeV only 70 events are observed containing one non-jet object, and 3 events with 2 muon objects. For $\Sigma p_T > 700$ GeV all events contain only jet objects. This is in agreement with Monte Carlo predictions. Table 5.3 summarises the remaining objects after different selection steps. It

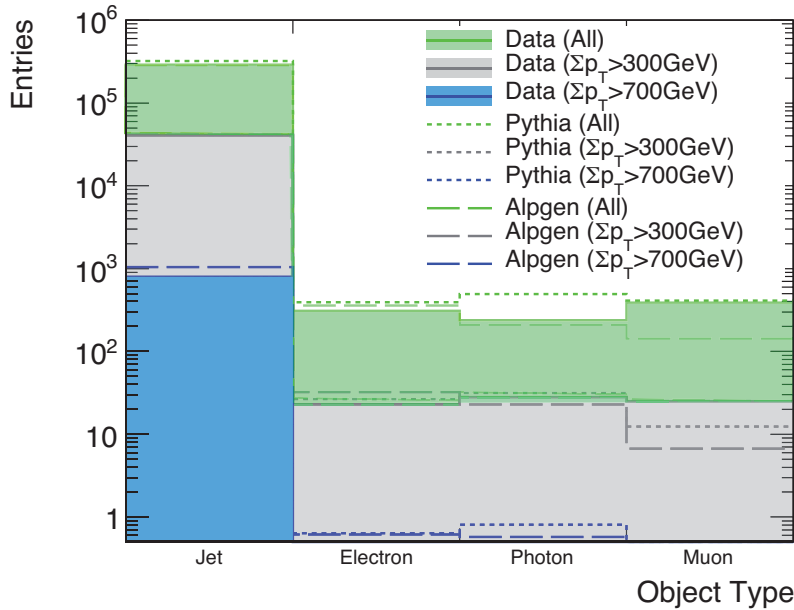


Figure 5.6.: Object type for events passing the selection criteria and varying p_T selections. The shown MC distributions are normalised to the number of data events in the control region.

supports the above statements.

The distributions of object transverse momentum p_T and pseudo-rapidity η are shown in Figures 5.7 and 5.8. The highest observed transverse momentum of an object in this sample is $p_T = 1.12$ TeV. In general, ALPGEN predicts a higher number of high p_T objects compared to PYTHIA. For $\Sigma p_T > 700$ GeV, ALPGEN deviates by more than 20% from data. PYTHIA shows a better agreement with the data. The pseudo-rapidity distributions show a good agreement in shape between data and MC. No regions with increased or decreased activity are visible.

5.5. Systematic Studies

A wide range of systematic studies has been done to estimate effects from detector and running conditions during early data taking. Object reconstruction uncertainties like jet energy scale and resolution are studied within the collaboration as outlined in Chapter 3, and are applied to this analysis. Also model uncertainties, e.g. the PDF choice and the Q^2 scale, are used to estimate the resulting uncertainty for this analysis. The results for most studies, which are described in more detail in the following, are collected in Table 5.4. A summary of all systematic studies is given at the end of this section.

QCD jet production

The two predictions for QCD jet production by PYTHIA and ALPGEN differ significantly, as can be seen in the distributions of Section 5.4. Figure 5.9 shows the invariant mass

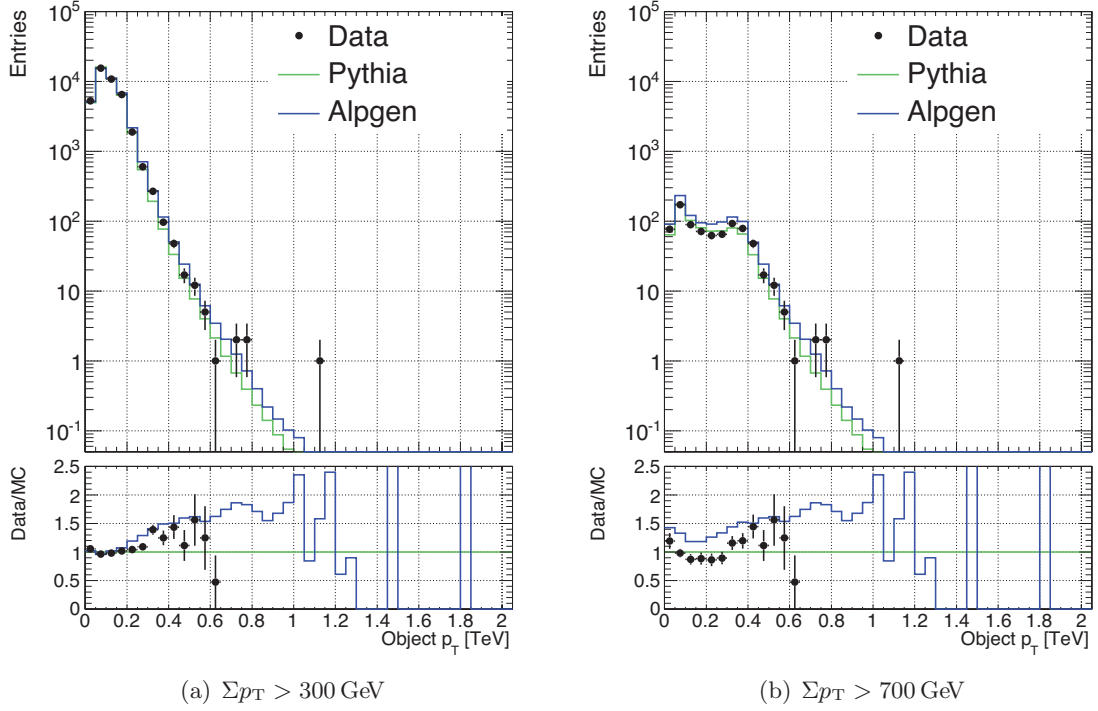


Figure 5.7.: Distributions of the transverse momentum p_T for objects passing the selection criteria. The shown MC distributions are normalised to the number of data events in the control region.

Criteria	Objects	Jets	Electrons	Photons	Muons
total	81 891 571	43 478 000	28 681 336	8 907 764	824 471
object selection	6 261 452	6 234 632	12 600	12 359	1861
OTX selection	6 259 854	6 234 632	11 821	11 540	1861
event cleaning	6 259 854	6 234 632	11 821	11 540	1861
overlap removal	6 243 879	6 218 657	11 821	11 540	1861
$N \geq 3$	290 133	289 199	308	239	387
$\Sigma p_T > 300 \text{ GeV}$	40 817	40 741	23	28	25
control region	31 548	31 483	17	26	22
$\Sigma p_T > 700 \text{ GeV}$	792	792	0	0	0
signal region	772	772	0	0	0

Table 5.3.: Objects after different selection steps

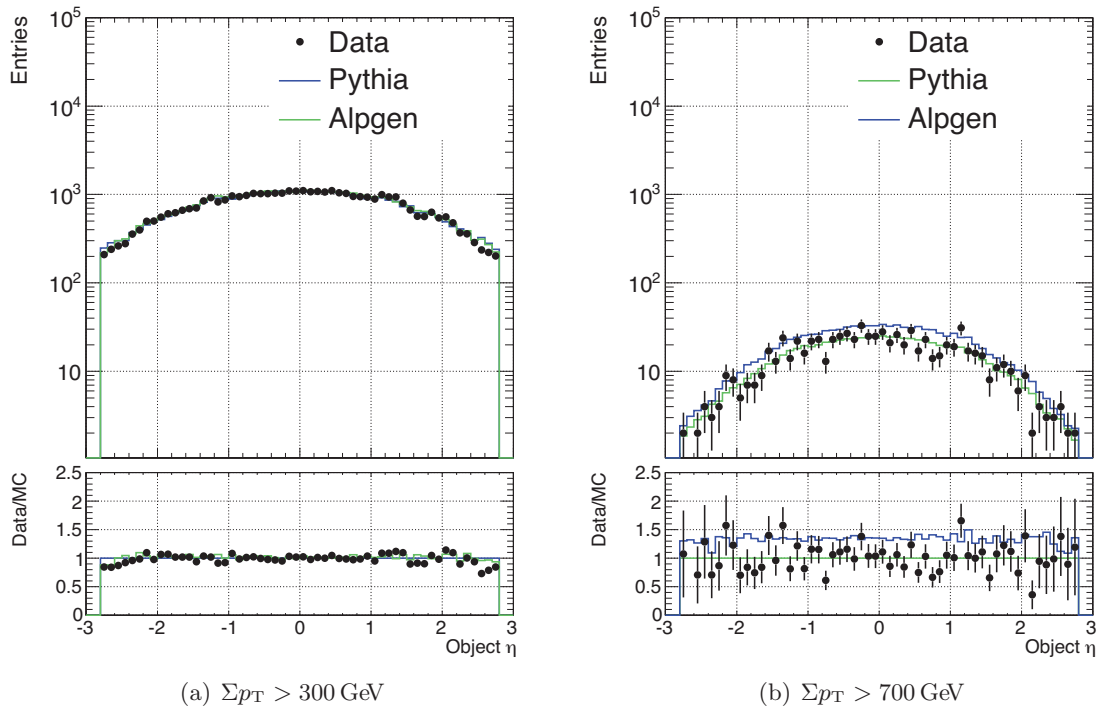


Figure 5.8.: Distributions of the pseudo-rapidity η for objects passing the selection criteria. The shown MC distributions are normalised to the number of data events in the control region.

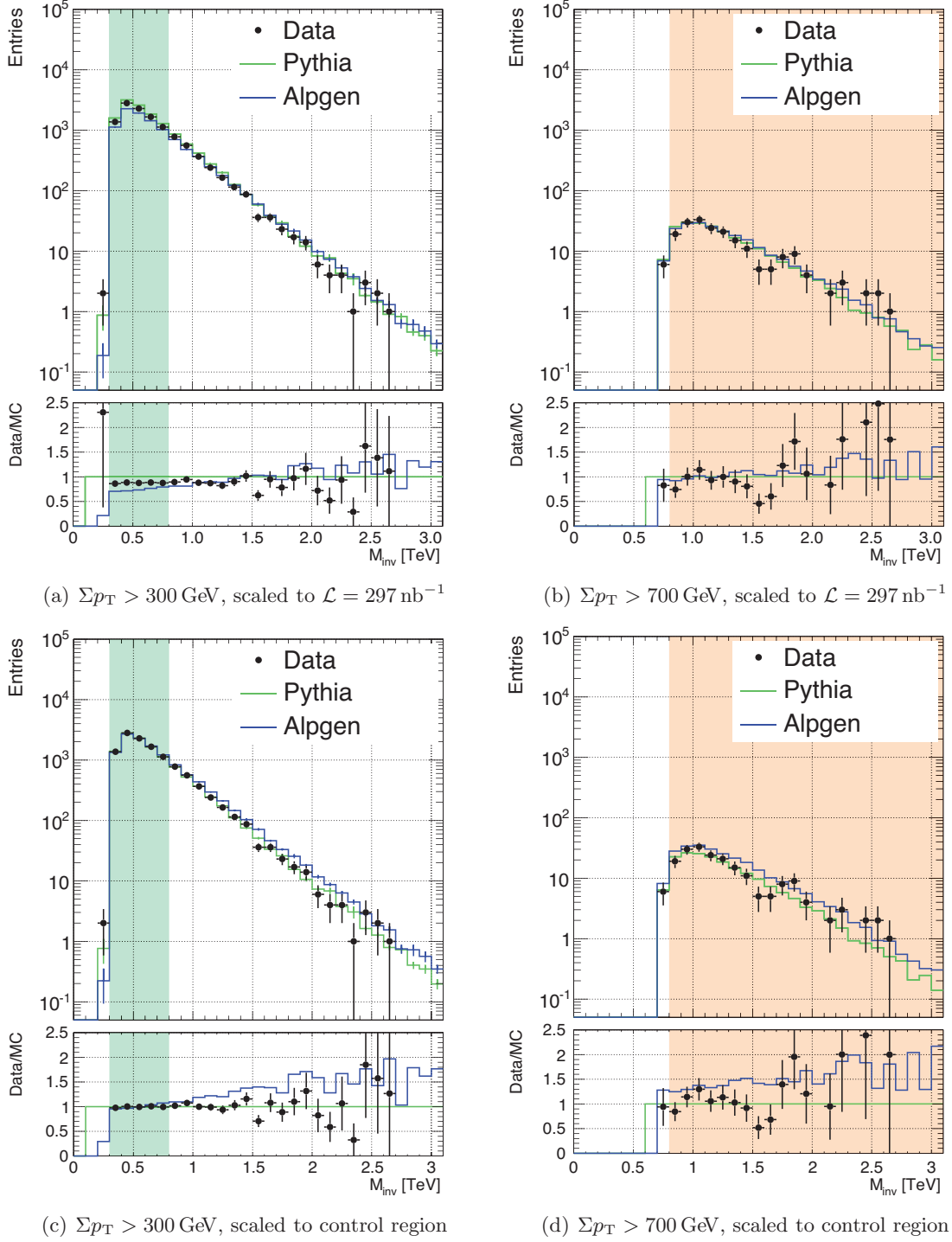


Figure 5.9.: Invariant mass distributions for data and QCD jet production with PYTHIA and ALPGEN. The samples are normalised to either a luminosity of $\mathcal{L} = 297 \text{ nb}^{-1}$ (a, b) or the number of data events in the control region (c, d).

	sample	events in CR norm to $\mathcal{L} = 297 \text{ nb}^{-1}$	events in SR	scale factor	events in SR norm to CR	relative to 183 events
QCD	PYTHIA	$10\,505 \pm 58$	208 ± 1.2	0.88	183 ± 1.0	
	ALPGEN	7747 ± 44	214 ± 1.6	1.19	255 ± 2.0	+37.8 %
PDF	CTEQ6ll	$10\,505 \pm 58$	208 ± 1.2	0.88	183 ± 1.0	
	MRST2007	$14\,499 \pm 69$	272 ± 1.4	0.64	173 ± 0.9	-5.6 %
	CTEQ6.6	$11\,571 \pm 61$	244 ± 1.3	0.80	194 ± 1.0	+6.1 %
	error up		266		209	+7.4 %
	error down		225		183	-5.8 %
Q^2	$\alpha = 1.0$	$10\,505 \pm 58$	208 ± 1.2	0.88	183 ± 1.0	
	$\alpha = 0.5$	$11\,265 \pm 60$	235 ± 1.3	0.82	192 ± 1.0	+5.2 %
	$\alpha = 2.0$	9817 ± 57	187 ± 1.1	0.94	175 ± 1.1	-4.2 %
JES	unchanged	$10\,505 \pm 58$	208 ± 1.2	0.88	183 ± 1.0	
	+JES	$15\,775 \pm 82$	362 ± 1.9	0.58	212 ± 1.1	+15.8 %
	-JES	7080 ± 43	120 ± 0.8	1.30	156 ± 1.0	-14.7 %
JER	unchanged	$10\,505 \pm 58$	208 ± 1.2	0.88	183 ± 1.0	
	JER	$10\,907 \pm 63$	216 ± 1.2	0.85	182 ± 1.0	-0.3 %

Table 5.4.: Number of events in control (CR) and signal (SR) region for different systematic studies. The given numbers are calculated for PYTHIA if not otherwise stated. The given uncertainty is the statistical uncertainty due to the limited statistics of the samples.

distributions for data and the Monte Carlo samples. The shaded regions illustrate the control and signal region. For PYTHIA the shape agreement in the invariant mass distribution is good, while the cross section prediction is too low compared to data. This conclusion can be drawn from the distributions normalised to luminosity (a, b). In the distributions normalised to the number of data events in the control region (c, d) it is visible that the shape agreement between ALPGEN and data is worse compared to PYTHIA. The prediction of the number of high mass final states is significantly higher. There is no clear evidence which generator is more accurate in the physics description of the analysed final states. The number of events in control and signal region are shown in Table 5.4. Due to the better shape agreement in object p_T and invariant mass, PYTHIA is used as baseline sample. The difference of +37.8% from ALPGEN to PYTHIA is taken as systematic uncertainty of the QCD jet production prediction.

Background

The number of events expected in the control and signal region from the different background processes listed in Section 5.2 is dependent on their cross sections. As can be seen in Figure 5.10, the contributions from background processes like W +jets, Z +jets and $t\bar{t}$ are clearly negligible to the standard QCD jet production in both control and signal region. Therefore the only background process used for the systematic studies and the following calculations is QCD jet production. Adding all other contributions up, an uncertainty of +1% is assigned to the number of expected background events.

Contributions from Leptons and Photons

The number of events with electrons, photons or muons in the control or signal region is very low. In the control region 61 events contain one or more of these objects, while in the signal region only jets are present (see also Section 5.4). Only 4 of the events in the control region do not pass the requirement of three or more objects, when only jets are considered. The 61 events in the control region correspond to only 0.6% of all 9223 events in this region. Therefore no systematic studies for electrons, photons and muons are done. The uncertainty due to the inclusion of these object types without detailed performance study is reflected with a systematic uncertainty of $\pm 0.6\%$.

Control Region

The choice of the control region has a direct influence on the estimation of the QCD background. The challenge is to find a region with high statistics while being in a similar kinematic regime as the signal region, but free from signal events. Due to the steeply falling M_{inv} distribution (see Figure 5.9) it is desirable to choose a lower boundary in order to use as much statistics as possible. At the same time it is necessary to be close to the signal region and avoid the influence of processes from another kinematic regime, i.e. lower mass and p_T final states compared to the signal region. To study the influence of the choice of the control region different regions are compared for ALPGEN and PYTHIA. The results can be seen in Figure 5.11 and are summarised in Table 5.5. In general ALPGEN behaves more stable under variation of the control region compared to PYTHIA. For PYTHIA only a dependence on the

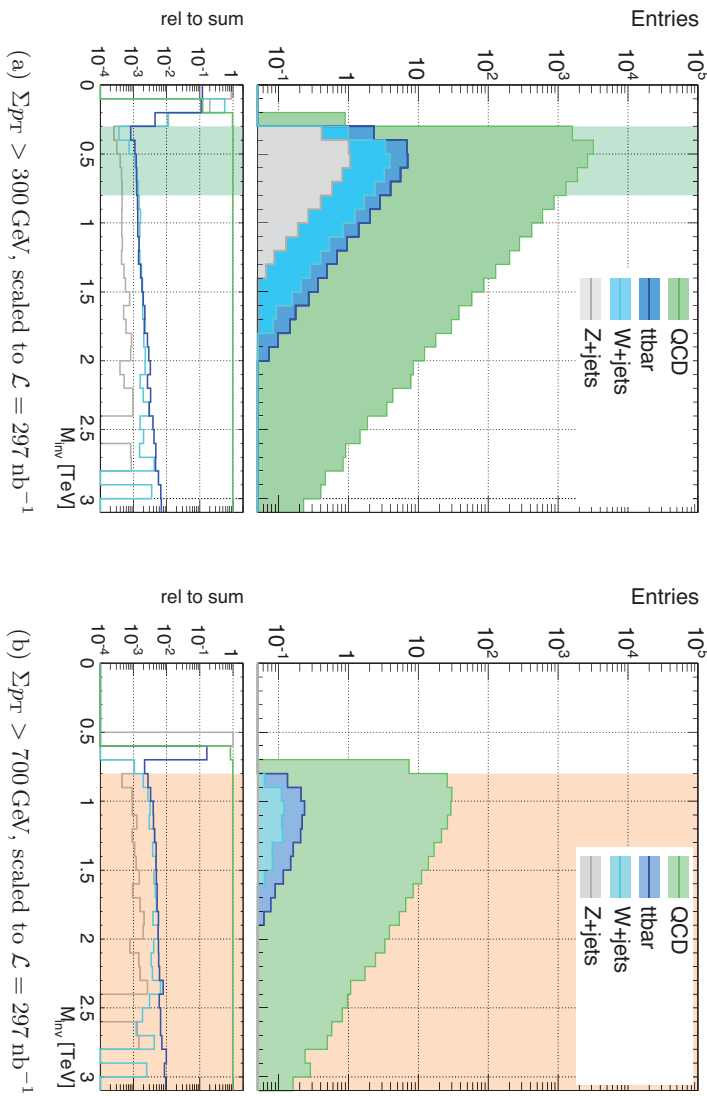


Figure 5.10.: Invariant mass distributions for different background processes. The samples are normalised to a luminosity of $\mathcal{L} = 297 \text{ nb}^{-1}$.

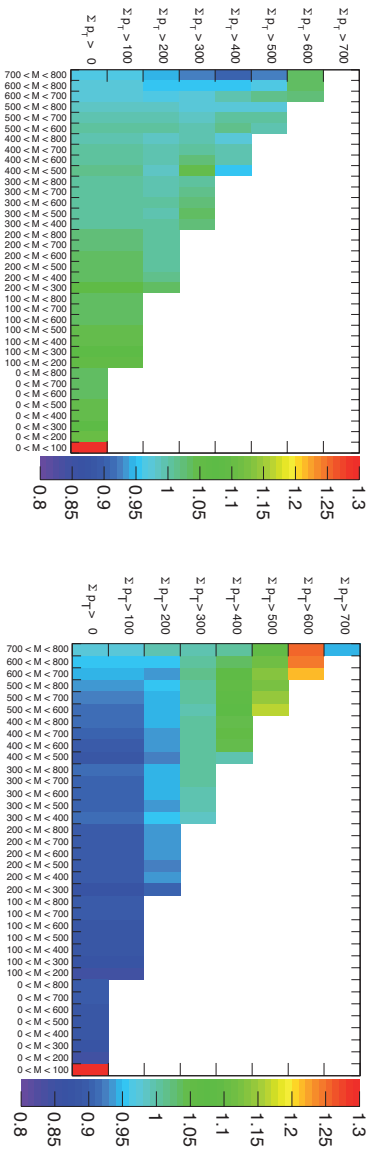


Figure 5.11.: Normalisation factors for different control regions relative to the nominal chosen control region ($\Sigma p_T > 300 \text{ GeV}$ and $300 \text{ GeV} < M < 800 \text{ GeV}$). The left figure shows the results for the PYTHIA sample, the right figure for the ALPGEN sample. The units of M_{inv} and Σp_T are 1 GeV.

$M_{\text{inv}}^{\text{min}}$	500 GeV	400 GeV	300 GeV	200 GeV
PYTHIA				
$\Sigma p_{\text{T}} > 200 \text{ GeV}$	179 (13280)	177 (24185)	177 (39739)	176 (50073)
$\Sigma p_{\text{T}} > 300 \text{ GeV}$	188 (5756)	188 (8918)	188 (10505)	
$\Sigma p_{\text{T}} > 400 \text{ GeV}$	197 (1996)	196 (2304)		
$\Sigma p_{\text{T}} > 500 \text{ GeV}$	211 (497)			
ALPGEN				
$\Sigma p_{\text{T}} > 200 \text{ GeV}$	250 (9504)	251 (17015)	253 (27851)	255 (34501)
$\Sigma p_{\text{T}} > 300 \text{ GeV}$	248 (4367)	254 (6626)	255 (7747)	
$\Sigma p_{\text{T}} > 400 \text{ GeV}$	249 (1586)	248 (1823)		
$\Sigma p_{\text{T}} > 500 \text{ GeV}$	248 (422)			

Table 5.5.: Predicted number of events from PYTHIA and ALPGEN MC in the signal region for different control regions. The upper invariant mass limit is 800 GeV. The number of events in the control region is shown in parentheses.

Criteria	Events
total	4820
trigger	322
vertex	310
control region	13
signal region	2

Table 5.6.: Debug stream events after different selection steps

choice of the lower bound of Σp_{T} can be seen. Due to the ambiguity of the control region choice a systematic uncertainty of 10% is assigned.

Debug Stream

As described in Section 3.2.5, a thorough check of the events stored in the debug stream is necessary for a search analysis to ensure that no interesting event is missed due to trigger problems. For this reason the debug stream events for the whole data taking period are analysed. The results are summarised in Table 5.6.

Here it is assumed that all debug stream events in the control and signal region are correctly reconstructed. The effect of the 13 events in the control region on the background normalisation can be neglected. Due to the 2 events in the signal region an additional uncertainty of 1% is assigned.

PDF Uncertainty

A different parton distribution function (PDF) leads to changes in the cross section and the shape of distributions for certain processes. Different PDF sets are available. Since their predictions vary using different sets will introduce an uncertainty on the estimations coming from Monte Carlo samples. A PDF set delivers the probabilities for a parton to carry a certain momentum fraction of the proton (denoted by the Bjorken variable x) while taking part in an interaction at a certain energy scale (referred to as Q^2). This scale is defined as follows:

$$Q^2 = \alpha \sum p_{\perp}^2 \quad (5.6)$$

where the sum runs over all final state partons after the hard process and $\alpha = 1$ is a scaling coefficient.

Monte Carlo events are generated using one particular PDF set. In order to estimate the effect from using different PDF sets, events are reweighted according to their parton type, momentum fraction and the scale of both partons in the interaction. The weight is derived as follows:

$$w = \frac{f_n(\text{ID}_1, x_1, Q^2) f_n(\text{ID}_2, x_2, Q^2)}{f_o(\text{ID}_1, x_1, Q^2) f_o(\text{ID}_2, x_2, Q^2)} \quad (5.7)$$

where $f_{n,o}$ denotes the probability calculated with the original (o) and new (n) PDF set. Comparing the results of the analysis with different PDF sets allows to determine the uncertainty due to the PDF choice.

For a PDF set with an associated error set the resulting intrinsic uncertainty can be calculated using an established method. As described in detail in Ref. [106], an error set holds n pairs of associated PDF sets, S_k^\pm . The uncertainties on a quantity F , which can be the PDF set or a derived quantity like a cross section, are then calculated as follows:

$$(\Delta F)_+ = \sqrt{\sum_{k=1}^n \left\{ \max [F(S_k^+) - F(S_0), F(S_k^-) - F(S_0), 0] \right\}^2} \quad (5.8)$$

$$(\Delta F)_- = \sqrt{\sum_{k=1}^n \left\{ \max [F(S_0) - F(S_k^+), F(S_0) - F(S_k^-), 0] \right\}^2} \quad (5.9)$$

with S_0 denoting the central PDF set. For each pair the biggest positive and negative deviation from the central value is used to determine the uncertainty. Applying the above to the background MC samples allows the estimation of an uncertainty due to PDF variations.

For this analysis three different PDF sets are used, CTEQ6L1 [85], MRST2007 [107] and CTEQ6.6 [108]. The latter one has an associated error set and is therefore used to determine the intrinsic uncertainty. In Figure 5.12 the invariant mass spectrum of the background samples is shown for different PDF sets. The normalisation in the control region is done for every PDF set individually. In Table 5.4 the event numbers in control and signal region for the different PDF sets are shown. Additionally the combined results for the error set of CTEQ6.6 are listed. The deviations of MRST2007 and CTEQ6.6 from the reference CTEQ6L1 are in the order of $\pm 6\%$. The intrinsic uncertainty calculated from the error set

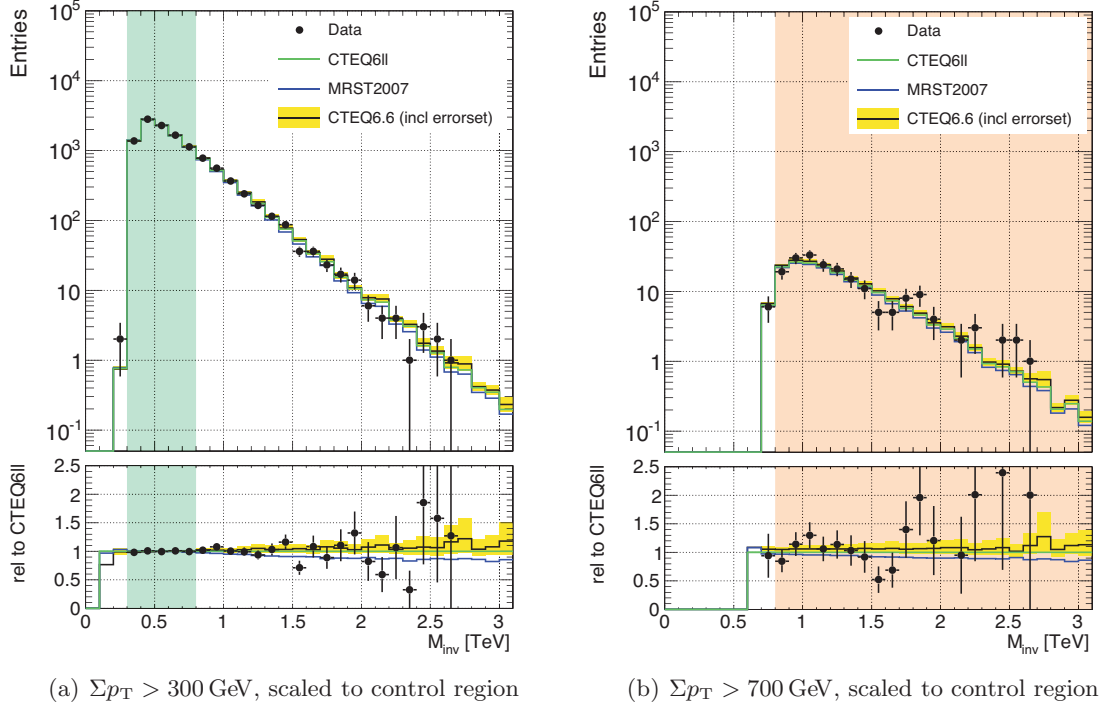


Figure 5.12.: Invariant mass distributions for PYTHIA samples with different PDF sets (CTEQ611, CTEQ6.6, MRST2007). For the PDF set CTEQ6.6 the associated error set is used and displayed.

of CTEQ6.6 is $+7.4\%$ and -5.8% . Both results are taken as an uncertainty due to the PDF choice and uncertainties.

Q^2 Scale Uncertainty

The choice of the Q^2 scale as defined in Eq. 5.6 has a direct influence on the weights calculated from the PDF sets. To estimate the uncertainty due to the scale choice two PYTHIA MC samples with $\alpha = 0.5, 2$ are used. The scale variation has an impact on the overall cross section of the sample. A raised scale value leads to a decrease in the cross section prediction. Nevertheless, due to the normalisation to a control region, this analysis is only sensitive to changes in the shape of the mass distributions. Figure 5.13 illustrates that this leads to a smaller effect than the PDF choice. Taking the numbers displayed in Table 5.4, the uncertainty due to the Q^2 scale choice is 5.2% .

Jet Energy Scale

As described in Section 3.3.1 the energy of jets is corrected by a factor to the jet energy scale (JES). This factor is determined from global cell weighting and is η and p_T dependent. Due to the dominant role of jets in the data sample an uncertainty on this calibration factor is expected to have a strong impact on this analysis. Extensive studies on the JES uncertainty

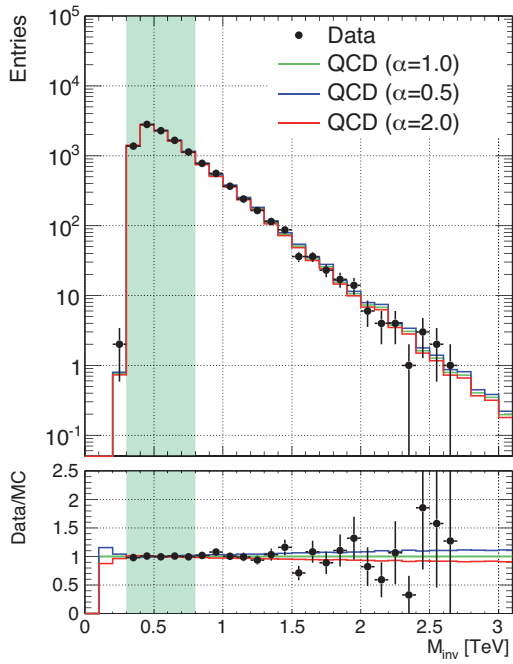
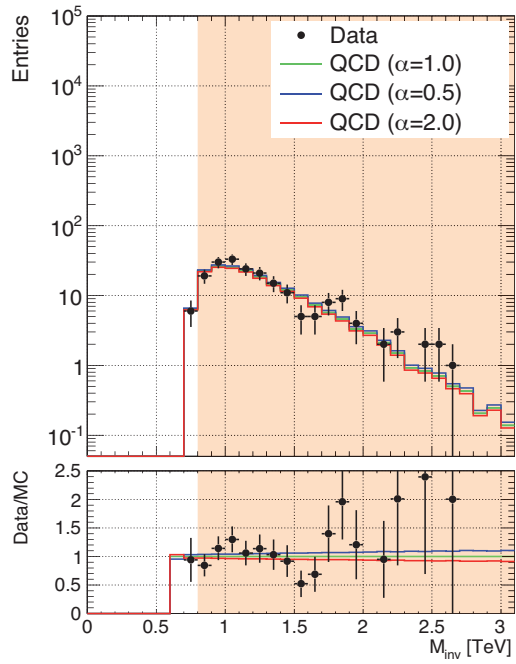
(a) $\Sigma p_T > 300$ GeV, scaled to control region(b) $\Sigma p_T > 700$ GeV, scaled to control region

Figure 5.13.: Invariant mass distributions for PYTHIA samples with different interaction scales ($\alpha = 1.0, 2.0, 0.5$).

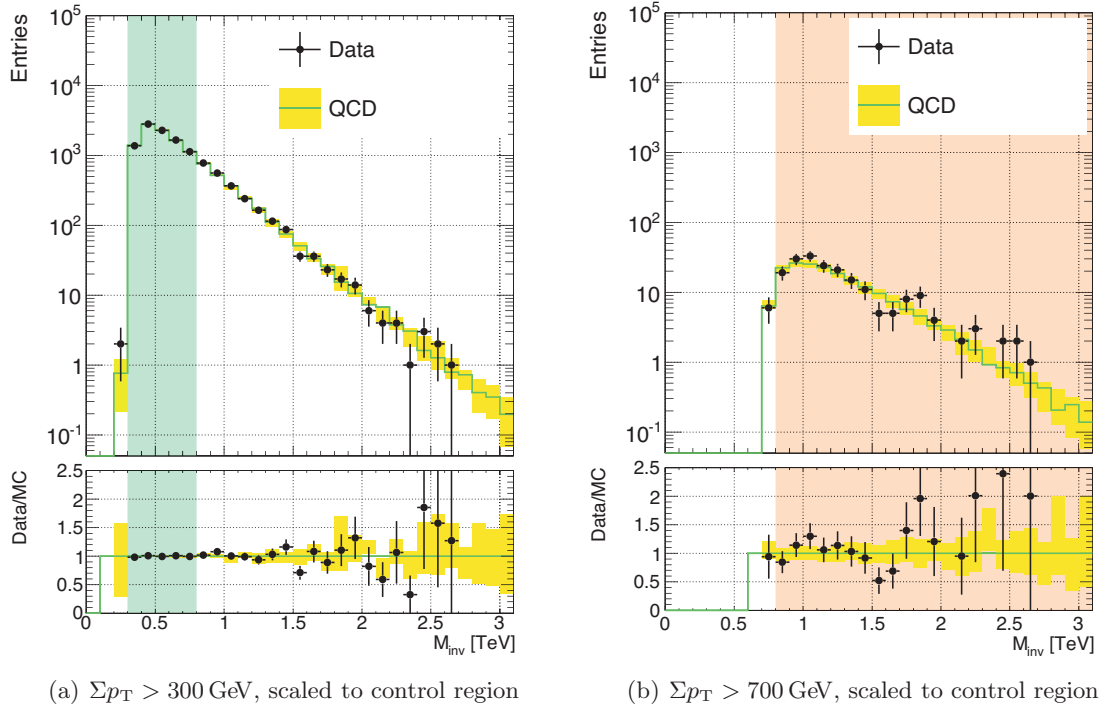


Figure 5.14.: Invariant mass distributions for data and PYTHIA events with a variation of the jet energy scale.

can be found in [64] and are outlined in Chapter 3.

It is shown that for a multi-jet environment the jet energy scale does not only depend on η and p_T but also on the distance to the closest jet neighbour. Therefore the uncertainty is calculated individually for every jet. The results from Ref. [64] are available for jets with $20 \text{ GeV} \leq p_T \leq 1000 \text{ GeV}$ and $|\eta| < 2.8$. For jets at a higher p_T the average uncertainty of 7% is assumed, since the according uncertainty is found to be decreasing with p_T [64]. To estimate the effect of the jet energy uncertainty on this analysis, the transverse momentum of every jet in the background MC sample is varied upwards and downwards according to its uncertainty. A propagation to the missing transverse energy due to the changed energies of jets in an event is done as well. The resulting invariant mass distributions are shown in Figure 5.14. As expected, the influence of the jet energy scale is large. Especially for high masses the shape change of the distribution leads to an increased uncertainty. The number of events in the control and signal region for a variation of the jet energy scale is shown in Table 5.4. The difference in signal region prediction is +15.8% and -14.7%. This is taken as an uncertainty due to the jet energy scale.

Jet Energy Resolution

The jet energy resolution depends on both the intrinsic resolution of the calorimeters as well as on statistical shower fluctuations and dead material effects (see also Section 3.3.1). To determine the influence on this analysis the jet energy is varied according to the results from

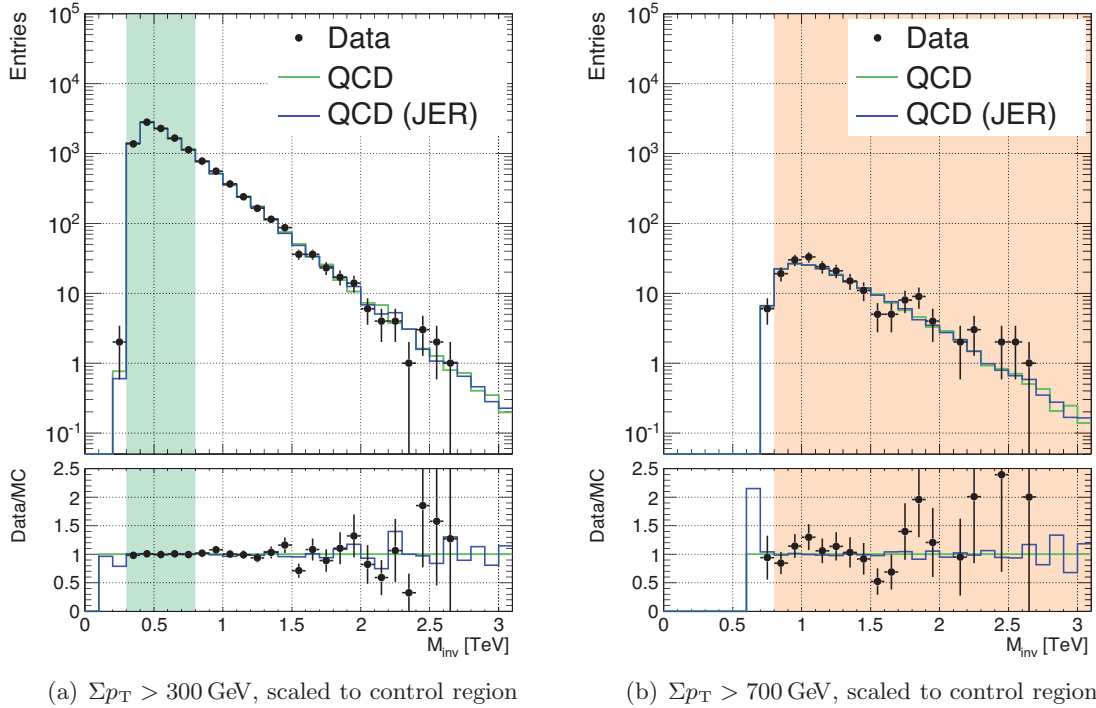


Figure 5.15.: Invariant mass distributions for data and PYTHIA events with a smearing of the jet energy according to the jet energy resolution uncertainty.

Ref. [65], which are also summarised in Chapter 3. The jet energy and jet transverse momentum of the background MC sample are smeared with a Gaussian distribution, which has a width corresponding to the η and p_T dependent resolution. As can be seen in Figure 5.15 the influence of the energy resolution compared to the original MC prediction is small. Following the numbers listed in Table 5.4 an uncertainty on the background prediction of 0.3% is assigned.

5.6. Results

Table 5.7 shows a summary of all studied uncertainties. The impact on the invariant mass distributions is shown in Figure 5.16. It is clearly visible that the Standard Model prediction and the result from the data analysis agree within the uncertainties. In the analysed data sample with an integrated luminosity of $\mathcal{L} = 297 \text{ nb}^{-1}$ a total of 194 ± 14 events are found in the signal region after all selections. Taking into account all aforementioned uncertainties, the background prediction is $183 \pm 1(\text{stat.}) + 80(\text{syst.})$. Hence, the number of data events is compatible with the Standard Model prediction within the uncertainties. This is also displayed in the invariant mass distributions of Figure 5.16, including all systematic uncertainties. A Bayesian credibility interval is set by the determination of a posterior probability distribution from the likelihood function for the cross section times acceptance of possible signal processes. A prior constant in this observable is used. Integration of the posterior

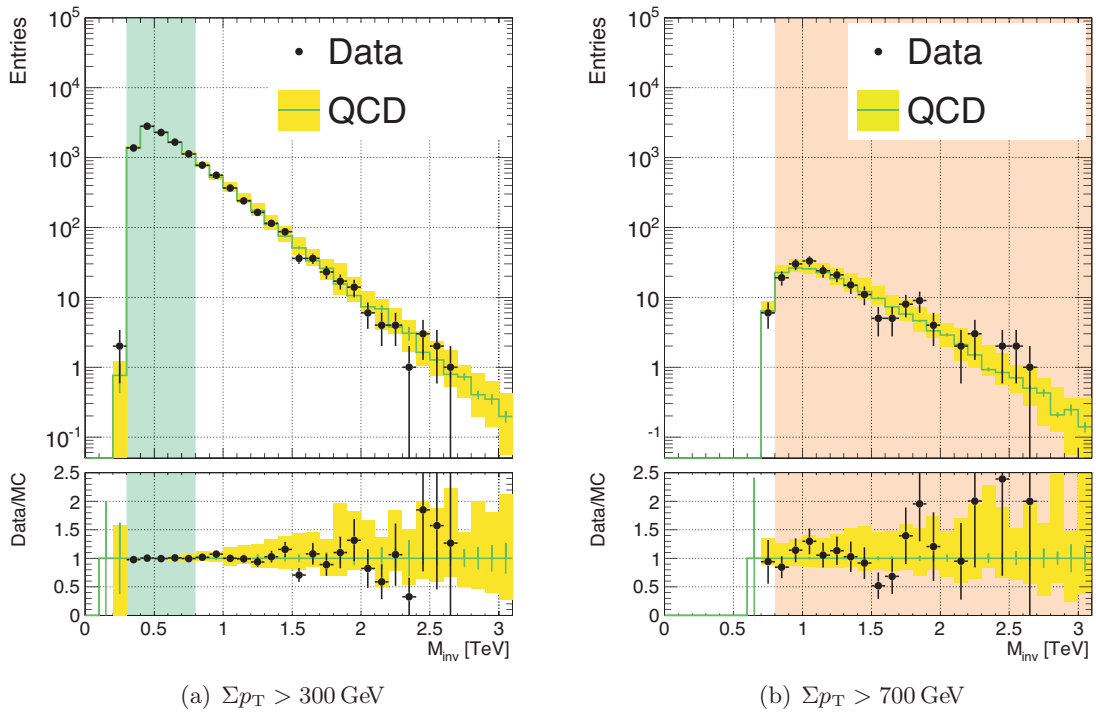


Figure 5.16.: Invariant mass distributions for data and background events as predicted by PYTHIA. The error band includes all systematic uncertainties added in quadrature, while the error bars depict the statistical uncertainty. The background distributions are normalised to the control region.

Study	Events	Uncertainty
Pythia	183	1 (stat.)
QCD jet production		+37.8 %
PDF choice		± 6.1 %
PDF errorset		+7.4 %
Q^2 scale		-5.8 %
Q^2 scale		+5.2 %
Q^2 scale		-4.2 %
Jet Energy Scale		+15.8 %
Jet Energy Scale		-14.7 %
Jet Energy Resolution		± 0.3 %
Other background processes		± 1 %
Including e, γ, μ		± 0.6 %
Control Region		± 10 %
Debug Stream		+1 %
Combined Uncertainty	+80	+43.6 %
	-37	-20.2 %

Table 5.7.: Summary of uncertainties for the background prediction

yields a 95 % credibility level (CL) upper limit on $\sigma \times A < 0.46$ nb. Details on this statistical approach can be found in Ref. [2]. To illustrate the acceptance of possible signal processes, an acceptance study with different signal samples is presented in the following.

5.7. Acceptance

For an estimation of the acceptance for a potential signal, signal samples at different parameter points are studied. Nine black hole samples are generated using CHARYBDIS with $N_{\text{FB}} = 3, 4, 5$ as fixed number of final burst particles and a mass threshold of 0.8, 1.0, 1.2 TeV for $M_{\text{th}} = M_{\text{D}}$. Another black hole sample is generated using BLACKMAX, with $M_{\text{th}} = 0.8$ TeV and a variable number of final burst particles. The choice of the final burst behaviour is an important parameter in the event generation for this study. Since the black holes are generated with masses close to M_{D} , and both generators use the final burst approach for the Planck phase of the decay, the dominant fraction of the emission is governed by the final burst mechanism.

Table 5.8 lists the acceptance for the different signal samples. A strong influence of the chosen threshold mass on the acceptance is visible, while the number of final burst particles leads only to minor variations. This threshold dependence comes from the sharp cut-off during event generation. The further away from the signal region border of $M_{\text{inv}} = 0.8$ TeV the threshold is, the higher the acceptance due to the later rise and peak of the distribution. For $M_{\text{th}} = 1.2$ TeV the highest acceptance with $A > 85$ % is determined. The average acceptance for the samples with $M_{\text{th}} = 0.8$ TeV is 57 %.

$M_D = M_{\text{th}}$ [TeV]	CHARYBDIS			BLACKMAX
	1.2	1.0	0.8	0.8
$N_{\text{FB}} = 3$	85.1 %	76.5 %	60.3 %	
$N_{\text{FB}} = 4$	88.3 %	78.6 %	57.4 %	
$N_{\text{FB}} = 5$	88.9 %	78.0 %	53.2 %	
$N_{\text{FB}} = \text{VAR}$				57.7 %

Table 5.8.: Event fraction in the signal region for different signal samples.

Due to known theoretical model uncertainties it is not possible to rule out any model. The influence of detector understanding and SM uncertainties on the signal acceptance can be studied with the available samples nevertheless. The acceptance is altered by changes in the shape or event migrations. In the following, the systematic uncertainties due to the PDF choice, the Q^2 scale, the jet energy scale and the jet energy resolution are used to determine potential effects on the acceptance.

Table 5.9 summarises the results from different systematic studies. The used samples have a threshold mass of $M_{\text{th}} = 0.8$ TeV. The used methods to determine the uncertainties are identical with the earlier systematic study of the SM background. The PDF uncertainty is calculated from the same PDF sets, CTEQ6L1, MRST2007 and CTEQ6.6. The latter is used to determine the intrinsic PDF uncertainty. The result can be seen in Figure 5.17. For simplicity only the BLACKMAX signal sample and the PYTHIA background distribution are displayed. Both are normalised to an integrated luminosity of $\mathcal{L} = 297 \text{ nb}^{-1}$. The other signal samples show a similar behaviour. From the ratio distribution at the bottom of the figure it can be seen that the different PDF sets have only little influence on the shape. Due to the high Q^2 scale the effect of different PDFs and the intrinsic uncertainty on the shape of the invariant mass distribution is negligible. The uncertainty on the acceptance is 0.4 %.

The influence of the Q^2 scale on the acceptance is expected to be small. The reason is that events of signal processes already appear at very high Q^2 scales. In this regime the PDFs are very robust against a variation of the scale. This conclusion can be drawn from Figure 5.18. The BLACKMAX sample is shown for different values of the scaling factor $\alpha = 0.5, 1.0, 2.0$. The variation leads to an increase (decrease) of the number of events for $\alpha = 0.5$ (2.0). The distribution shape stays unaltered, as can be seen in the ratio in the lower part of the figure. The influence on the acceptance is < 0.5 %.

A change in the jet energy scale leads to a strong migration of jets in the transverse momentum distribution, hence also influencing the shape of the Σp_T and M_{inv} distributions and thus the acceptance. Figure 5.19 shows this effect. Again, only the BLACKMAX and the PYTHIA sample are displayed. Due to the normalisation to $\mathcal{L} = 297 \text{ nb}^{-1}$, the uncertainty is smallest in the bins with the most entries. The shape difference resulting from the energy scale variation thus propagates to higher mass values. The migration of events leads to an uncertainty on the acceptance of up to 13 %.

The effect of the jet energy resolution on the shape of the transverse momentum distributions is expected to be small. Also the influence on the M_{inv} spectrum is minor, as can be seen in Figure 5.20. Here the invariant mass distribution is shown for all studied signal

generator	3		CHARYBDIS 4		5		BLACKMAX variable	
N_{FB}	CR	SR	CR	SR	CR	SR	CR	SR
CTEQ6.6	10.2 %	60.3 %	17.7 %	57.4 %	23.5 %	53.2 %	12.5 %	57.7 %
error up		+0.4 %		+0.4 %		+0.4 %		+0.4 %
error down		-0.3 %		-0.3 %		-0.3 %		-0.3 %
CTEQ6L1	10.2 %	60.5 %	17.7 %	57.6 %	23.3 %	53.5 %	12.4 %	57.9 %
MRST2007	10.3 %	60.1 %	17.8 %	57.2 %	23.4 %	53.1 %	12.4 %	57.5 %
$\alpha = 1.0$	10.2 %	60.3 %	17.7 %	57.4 %	23.5 %	53.2 %	12.5 %	57.7 %
$\alpha = 0.5$	10.1 %	60.1 %	17.5 %	57.8 %	23.2 %	53.5 %	12.4 %	58.0 %
$\alpha = 2.0$	10.4 %	60.6 %	17.9 %	57.1 %	23.8 %	52.8 %	12.7 %	57.5 %
	10.2 %	60.3 %	17.7 %	57.4 %	23.5 %	53.2 %	12.5 %	57.7 %
JES up	5.3 %	69.0 %	10.2 %	67.4 %	14.9 %	64.9 %	7.3 %	66.8 %
JES down	20.0 %	49.4 %	27.8 %	45.1 %	35.6 %	40.8 %	22.2 %	46.7 %
	10.2 %	60.3 %	17.7 %	57.4 %	23.5 %	53.2 %	12.5 %	57.7 %
JER	10.6 %	60.6 %	17.6 %	57.6 %	23.2 %	53.4 %	12.8 %	58.1 %

Table 5.9.: Event fraction in control (CR) and signal (SR) region for different signal samples. The listed systematic studies are performed concerning PDF choice and uncertainty, scale choice, jet energy scale (JES) uncertainty and jet energy resolution (JER) uncertainty.

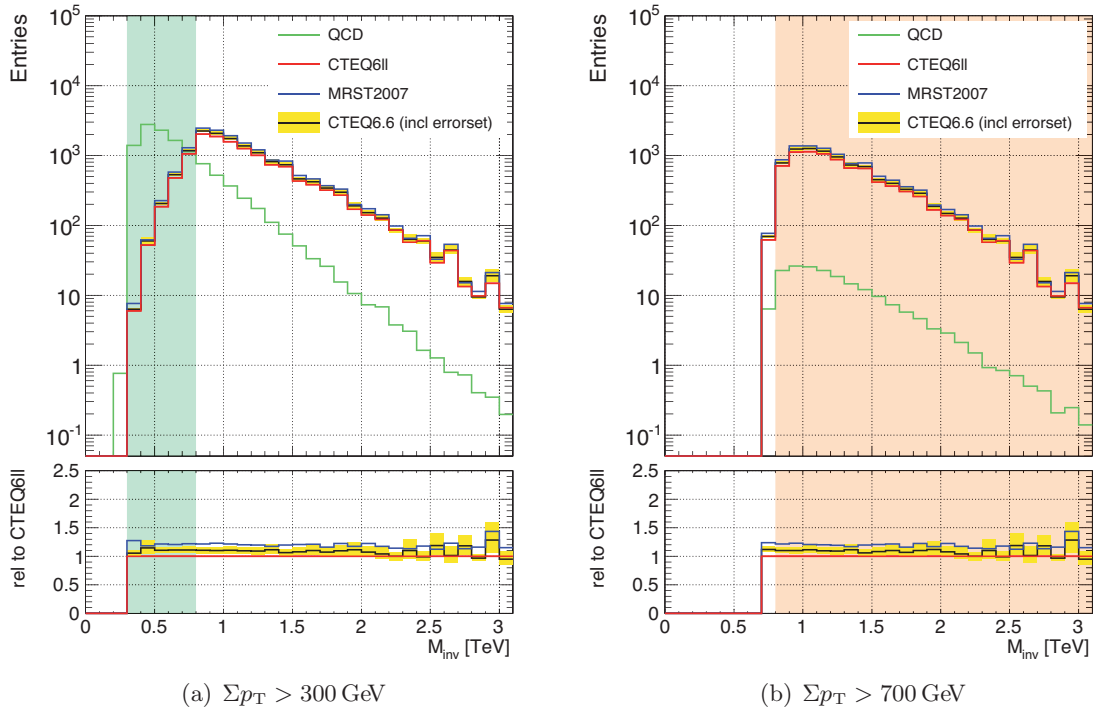


Figure 5.17.: Invariant mass distributions for the BLACKMAX samples with different PDF sets (CTEQ6ll, CTEQ6.6, MRST2007). For the PDF set CTEQ6.6 the associated error set is used and displayed. The samples are normalised to a luminosity of $\mathcal{L} = 297 \text{ nb}^{-1}$.

samples with nominal jet energy resolution (solid line) and with the jet energy resolution uncertainty applied (dashed line). The uncertainty on the acceptance is $< 0.5\%$.

In summary, the acceptance for the signal samples with $M_{\text{th}} = M_{\text{D}} = 0.8 \text{ TeV}$ varies between 53.2% and 60.3% . The highest acceptance is expected for the model with the lowest N_{FB} . On average, the CHARYBDIS samples with a fixed number of final burst particles predict an acceptance of 57.0% , which is in good agreement with the BLACKMAX sample with variable N_{FB} . The study of detector effects and SM uncertainties shows, that the biggest influence on the acceptance is produced by the jet energy scale uncertainty with up to 13% . All other studied systematic uncertainties are well below 1% .

5.8. Summary

This study is using the first $\mathcal{L} = 297 \text{ nb}^{-1}$ of $\sqrt{s} = 7 \text{ TeV}$ data to conduct a search for low-scale gravity effects. To keep the analysis as inclusive as possible within the context of high mass, large multiplicity final states, only basic selection criteria are applied. After requiring $N_{\text{obj}} \geq 3$ a signal region is defined with $\Sigma p_T > 700 \text{ GeV}$ and $M_{\text{inv}} > 800 \text{ GeV}$. The background prediction from PYTHIA MC is normalised to the data in a control region with $\Sigma p_T > 300 \text{ GeV}$ and $300 \text{ GeV} < M_{\text{inv}} < 800 \text{ GeV}$. In data, $194 \pm 14(\text{stat.})$ events are found in the signal region. To estimate the influence of detector understanding and SM uncertainties,

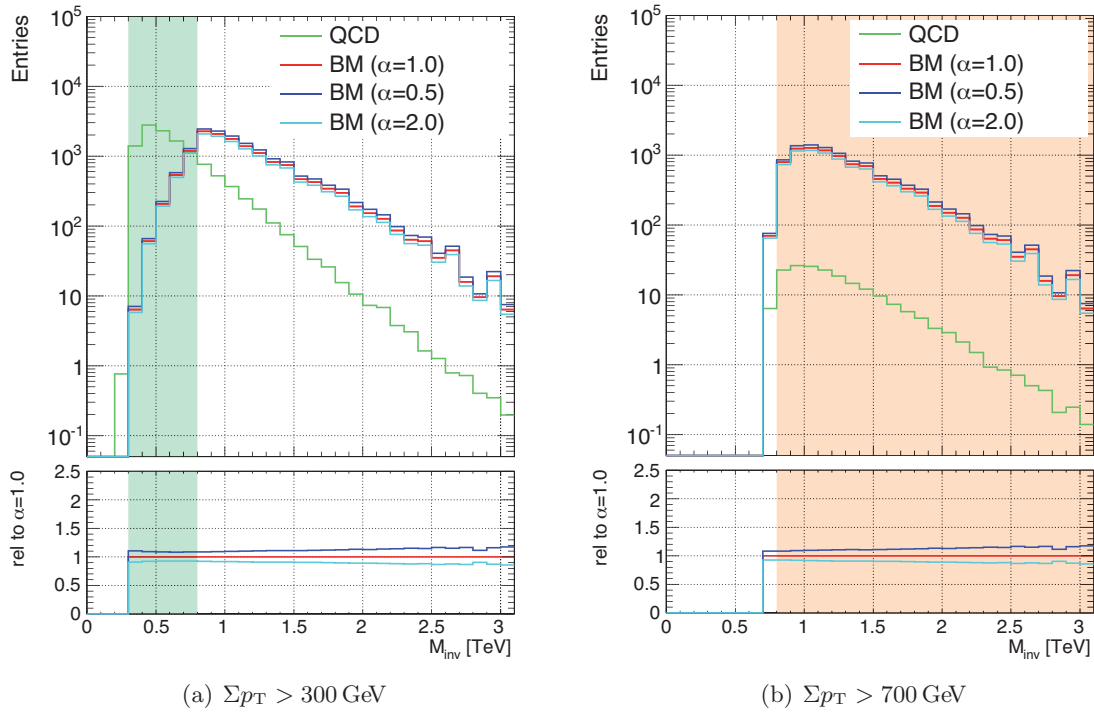


Figure 5.18.: Invariant mass distributions for the BLACKMAX sample with different interaction scales ($\alpha = 1.0, 2.0, 0.5$). The samples are normalised to a luminosity of $\mathcal{L} = 297 \text{ nb}^{-1}$.

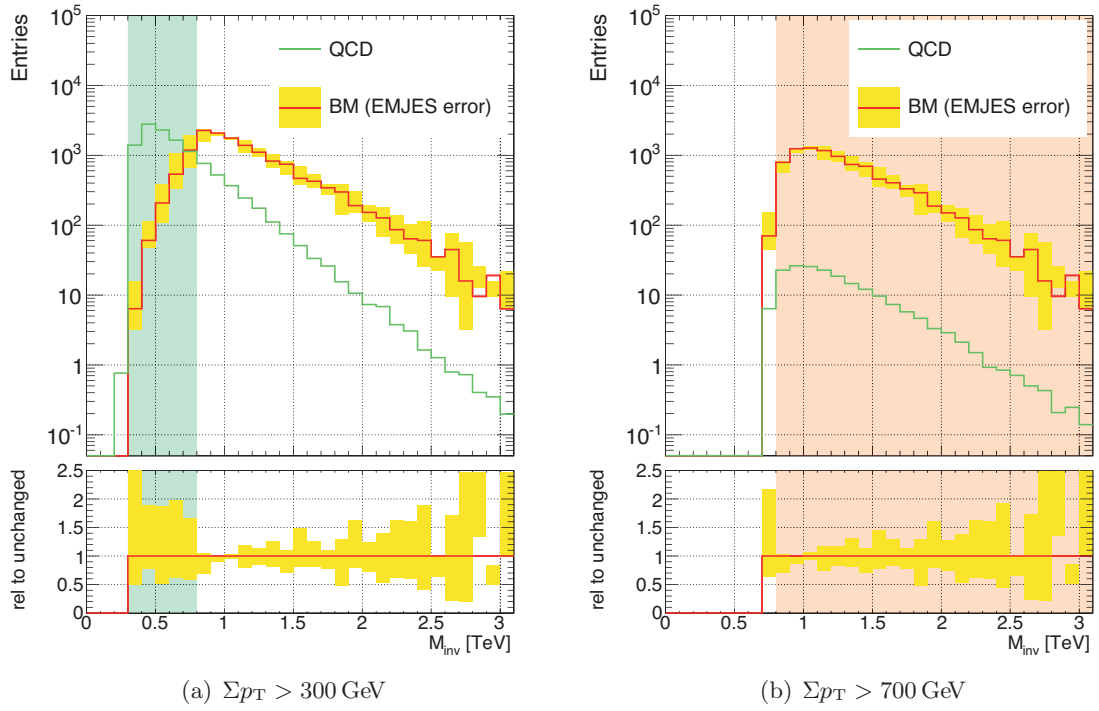


Figure 5.19.: Invariant mass distributions for the BLACKMAX sample with a variation of the jet energy scale. The samples are normalised to a luminosity of $\mathcal{L} = 297 \text{ nb}^{-1}$.

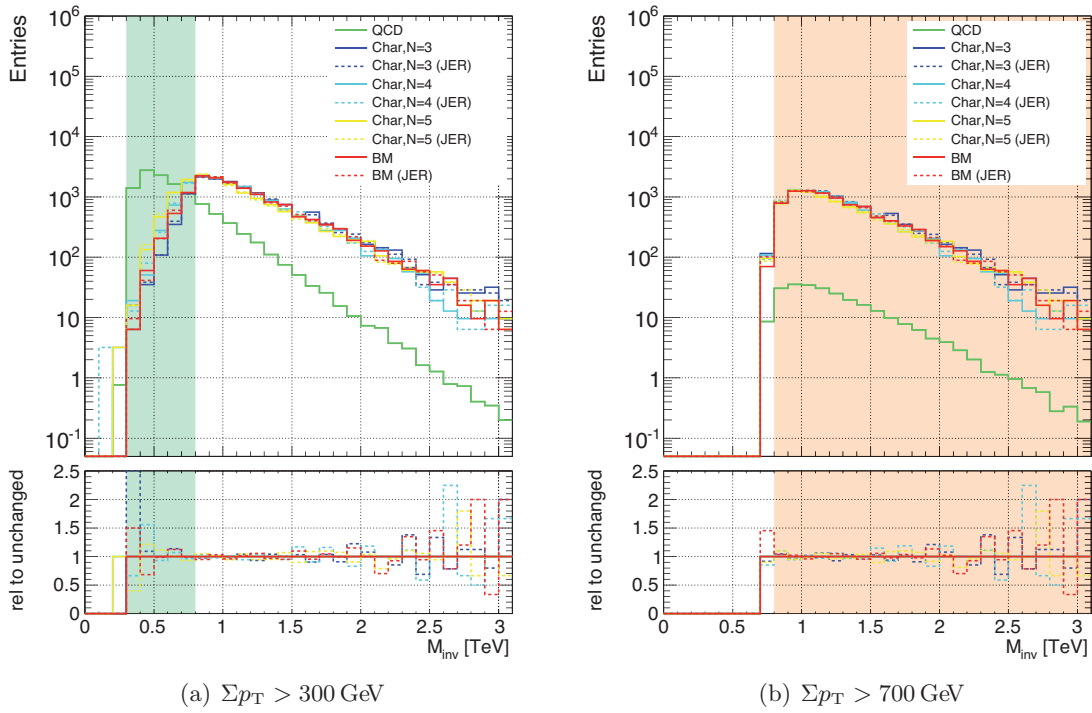


Figure 5.20.: Invariant mass distributions for different signal samples and PYTHIA with a smearing of the jet energy according to the Jet Energy Resolution uncertainty. The samples are normalised to a luminosity of $\mathcal{L} = 297 \text{ nb}^{-1}$.

extensive systematic studies are done. Included detector uncertainties are coming from the jet energy scale and resolution. Studied SM uncertainties are QCD background modelling, PDF choice and Q^2 scale. It is found, that the biggest uncertainty is produced by the choice of the QCD jet production MC. Other important factors are the PDF choice and jet energy scale uncertainty. In total, the predicted number of background events in the signal region is $183 \pm 1(\text{stat.}) + 80(\text{syst.})$. This leads to a limit on the cross section times acceptance for a possible signal of $\sigma \times A < 0.46 \text{ nb}$ at 95 % CL. Comparing the limits to possible production cross sections for gravitational signatures in the order of $\mathcal{O}(10 - 100 \text{ nb})$, this analysis has an impact on low-scale gravity scenarios, in the case that the signal acceptance is not too small.

The signal acceptance is studied using different samples generated with CHARYBDIS and BLACKMAX. For the samples with the lowest considered threshold mass, $M_{\text{th}} = 0.8 \text{ TeV}$, the acceptance is about 57 %. The influence of detector understanding and SM uncertainties is studied using the same methods as for the background. The considered influences are the PDF choice, the Q^2 scale, the jet energy scale and the jet energy resolution uncertainty. Except for the jet energy scale uncertainty, all other influences are negligible. The systematic effect on the acceptance from non-signal related sources is 13 %.

A similar analysis was presented by the ATLAS collaboration [109]. Control and signal region as well as the background normalisation are the same. In the course of this work contributions were made with studies on triggering, the control region choice and the jet energy scale. The main difference to the analysis presented here is the choice of the QCD background Monte Carlo. In this work, emphasis was put on the agreement in the jet p_{T} and η spectrum, and the resulting mass spectrum. Hence, PYTHIA was chosen here for QCD jet production. Due to historical reasons and the more stable behaviour under a variation of the control region, the ALPGEN sample was chosen in the other analysis. To cover the control region stability, an uncertainty of 10 % is assigned in both analyses. Compared to the published results, additional studies were made in this work on the Q^2 scale dependence and systematics for signal acceptance.

Figure 5.21 shows the invariant mass distribution for data and ALPGEN including all covered systematic uncertainties. The background prediction is $254 \pm 18(\text{stat.}) \pm 84(\text{syst.})$ in the ALPGEN study. Due to the higher background prediction, a stricter limit is placed on the cross section times acceptance for a possible signal of $\sigma \times A < 0.34 \text{ nb}$ [109]. In this work, the background prediction is lower and closer to the result in data, leading to a more conservative limit.

The analysis presented in this work is aimed at the very early data. It has the advantage of a signal region starting at low Σp_{T} and M_{inv} . It is optimised for low integrated luminosities and does not scale with an increasing amount of data. Due to significant background contributions to the signal region, an increase of the integrated luminosity does not lead to a comparable improvement of the limit. Nevertheless, the inclusive approach helped to conduct this early search and place a first limit on the cross section times acceptance.

The CMS collaboration recently presented limits on the cross section times acceptance for comparable final states, using 35 pb^{-1} of data [110]. The upper limit is determined depending on $S_{\text{T}} \equiv \Sigma p_{\text{T}} + E_{\text{T}}^{\text{miss}}$. The observed limit is $\sigma \times A < 9 \text{ pb}$ at 95 % CL for $S_{\text{T}} > 1 \text{ TeV}$ and $N_{\text{obj}} \geq 3$.

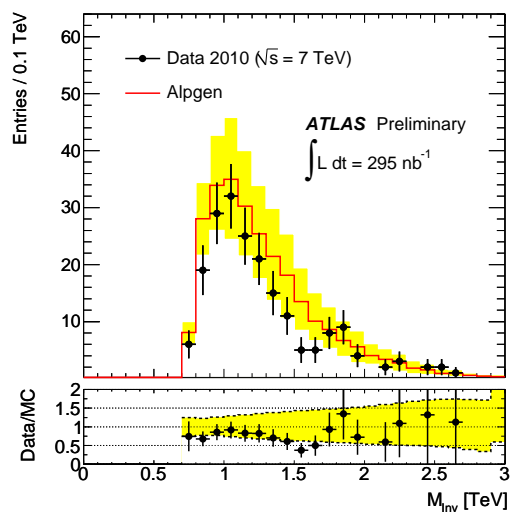


Figure 5.21.: Invariant mass distribution for an identical study with ALPGEN as QCD jet production background. The shown distribution has a requirement of $\Sigma p_T > 700$ GeV and shows data and the ALPGEN sample including all covered systematic uncertainties for a luminosity of $\mathcal{L} = 295 \text{ nb}^{-1}$ [109].

6. Conclusion and Outlook

In the first half of 2010, the LHC started colliding protons with $\sqrt{s} = 7$ TeV. This enables the LHC experiments to investigate a kinematic regime that has not been explored before. The multi-TeV range is expected to strengthen the Standard Model knowledge and to reveal new physics scenarios.

The ATLAS experiment is a general purpose detector designed to study a broad range of physics signatures at the LHC. Presented in this work are the main building blocks of the detector: An efficient tracking system, a highly granular and hermetic calorimeter system, all enclosed by a muon system with a dedicated air toroidal magnet system and a read-out steered by a reliable trigger system. A timing update of the L1Calo system is presented which leads to a performance improvement of the Level-1 trigger. The performance with early data is summarised for important systematic studies of the jet energy scale and resolution. This shows the level of detector understanding and thus the ability to discover new phenomena.

This work focuses on one scenario of physics beyond the Standard Model: Large Extra Dimensions. Models with large extra dimensions address the hierarchy problem and predict a fundamental Planck scale M_D of the order $\mathcal{O}(1 \text{ TeV})$. This low-scale gravity has an impact on particle physics and allows new processes to take place. One distinct prediction is the production of black holes in particle collisions. The search for these microscopic black holes with the ATLAS experiment is the main topic of this work.

The production and decay of black holes are a key signature for low-scale gravity. This is modelled in Monte Carlo generators like BLACKMAX, which was implemented and validated for the collaboration. A high creation mass well above the fundamental Planck mass M_D is necessary to ensure the validity of the semi-classical description resulting in a decay via Hawking radiation. This leads to final states with a high multiplicity of objects with large transverse momentum and high scalar sum of the transverse momenta of all objects. A study is conducted analysing the dependence of the kinematic properties on model parameters like brane tension, brane splitting and the rotation of the black hole. Selection strategies requiring a high p_T lepton, which were established for $\sqrt{s} = 14$ TeV, allow for an early discovery. In this context the trigger behaviour of microscopic black holes is studied. It is shown that a single jet trigger with a threshold of up to 400 GeV is fully efficient for black hole events. The proposed selection strategies are inefficient for scenarios with lepton suppression, therefore a different search strategy is developed. For $\sqrt{s} = 10$ TeV, a selection on $\Sigma p_T > 3.5$ TeV and $p_T^{(5)} > 200$ GeV is efficient for all covered model scenarios and is an improvement compared to previous selections. An optimisation of the study for $\sqrt{s} = 7$ TeV with a slightly different approach leads to a selection on $\Sigma p_T > 3$ TeV and $p_T^{(5)} > 150$ GeV. The required integrated luminosity for a discovery exceeds 1 fb^{-1} , corresponding to the expected data amount recorded until the end of 2011. Hence, for a search with early data, a different strategy has to be pursued.

The search strategy deployed for the analysis of the first data taken with $\sqrt{s} = 7$ TeV

follows a model independent approach in the context of low-scale gravity by counting the events in a signal region defined by $N_{\text{obj}} \geq 3$, $\Sigma p_T > 700$ GeV and $M_{\text{inv}} > 800$ GeV. The background prediction is normalised to data in a control region. The number of data events in the signal region is compared to the background prediction from PYTHIA, looking for a deviation from the Standard Model. Extensive studies of the systematic uncertainties are conducted. Explicitly, this means studying the effects of the level of detector understanding, namely the jet energy scale and resolution, and the effects of Standard Model uncertainties, in the form of PDF choice, Q^2 scale and the modelling of QCD jet production. The latter, being determined from a comparison of PYTHIA and ALPGEN MC, is found to give the largest contribution (+37.8%). In the data sample corresponding to the first 297 nb^{-1} , a total of $194 \pm 14(\text{stat.})$ events are found in the signal region. The background prediction is $183 \pm 1(\text{stat.}) + 80(\text{syst.})$ events, including all systematic uncertainties. The result is compatible with the observation. A limit on cross section times acceptance of $\sigma \times A < 0.46$ nb at 95% CL is determined using a Bayesian approach with a flat prior. Since the cross section predictions of low-scale gravity effects close to the fundamental Planck scale are of the order $\mathcal{O}(10 - 100 \text{ nb})$, this analysis has an impact on such models in the case of a sufficient signal acceptance. No sound theories for quantum gravity effects close to the fundamental Planck scale exist, thus a reliable cross section prediction for such processes cannot be given. Hence, no limit on model parameters is calculated. Nevertheless, using black hole MC simulations with $M_D = M_{\text{th}} = 0.8 \text{ TeV}, 1.0 \text{ TeV}, 1.2 \text{ TeV}$, an acceptance study is conducted to determine illustrative acceptances. The lowest acceptance for the considered samples is 53%. The effect of detector understanding and SM uncertainties on the signal acceptance is studied as well. Considered sources are the jet energy scale and resolution, the choice of PDFs and the Q^2 scale. The uncertainty is dominated by the contribution from the jet energy scale. An uncertainty on the acceptance of $\pm 13\%$ is found. The result is compared to a similar study, which was presented by the ATLAS collaboration and to which contributions were made in the course of this work.

For early data the most promising search strategy was an inclusive approach, model independent in the context of low-scale gravity. With rapidly increasing instantaneous luminosity, the recorded amount of data will soon allow for more model dependent searches at the LHC, which provide sensitivity on parameters of both the black hole and the extra dimensions model. The discovery potential for low-scale gravity effects is high and fascinating signatures can be studied. Already the first years of data taking provide the chance to discover new and exciting physics, and the LHC era has only just begun.

A. Production of a Black Hole

In $n + 4$ dimensional space-time a black hole is formed if the impact parameter b of two colliding particles is smaller than the twice the event horizon radius r_h :

$$b < 2r_h(n, M_{\text{BH}}, J), \quad (\text{A.1})$$

where M_{BH} and J are the mass and the angular momentum of the black hole. It is useful to write the metric of a rotating black hole in Boyer-Lindquist coordinates.¹

It is given as [20]:

$$\begin{aligned} ds^2 = & \left(1 - \frac{\mu}{r^{n-1}\Sigma}\right) dt^2 - \sin^2 \theta \left(r^2 + a^2 + \frac{a^2 \mu \sin^2 \theta}{r^{n-1}\Sigma}\right) d\phi^2 \\ & + 2a \sin^2 \theta \frac{\mu}{r^{n-1}\Sigma} dt d\phi - \frac{\Sigma}{\Delta} dr^2 - \Sigma d\theta^2 - r^2 \cos^2 \theta d\Omega_n^2, \end{aligned} \quad (\text{A.2})$$

where

$$\begin{aligned} \Delta &= r^2 + a^2 - \frac{\mu}{r^{n-1}} \\ \Sigma &= r^2 + a^2 \cos^2 \theta, \end{aligned} \quad (\text{A.3})$$

and $d\Omega_n^2$ is the metric on an n -sphere. The black hole mass M_{BH} is related to the parameter μ as

$$M_{\text{BH}} = \frac{(n+2)A_{n+2}}{16\pi G_{\text{D}}}\mu \quad (\text{A.4})$$

with A_{n+2} as the area of an $(n+2)$ dimensional unit sphere, given as

$$A_{n+2} = \frac{2\pi^{\frac{n+3}{2}}}{\Gamma\left(\frac{n+3}{2}\right)}.$$

The angular momentum J is connected to the spin parameter a via

¹The Boyer-Lindquist coordinates r, θ, ϕ are related to Cartesian coordinates x, y, z as follows:

$$\begin{aligned} x &= \sqrt{r^2 + a^2} \sin \theta \cos \phi \\ y &= \sqrt{r^2 + a^2} \sin \theta \sin \phi \\ z &= r \cos \theta \end{aligned}$$

with a the parameter of the spin.

$$J = \frac{2}{n+2} M_{\text{BH}} a.$$

It can be shown [111] that the horizon occurs for $\Delta = 0$. From this the horizon radius r_{h} can be derived:

$$r_{\text{h}} = \left[\frac{\mu}{1 + \left(\frac{a}{r_{\text{h}}}\right)^2} \right]^{\frac{1}{n-1}} = \frac{r_{\text{s}}}{\left[1 + \left(\frac{a}{r_{\text{h}}}\right)^2 \right]^{\frac{1}{n-1}}} \quad (\text{A.5})$$

The Schwarzschild radius $r_{\text{s}} \equiv \mu^{1/(n+1)}$ is the event horizon radius for a non-rotating black hole. Equation A.4 can now be rewritten as

$$M_{\text{BH}} = \frac{2\pi^{\frac{n+3}{2}} (n+2) M_{\text{D}}^{n+2}}{\Gamma\left(\frac{n+3}{2}\right) 2(2\pi)^n r_{\text{s}}^{n+1}} \quad (\text{A.6})$$

For the collision of two massless particles with a centre-of-mass energy $\sqrt{s} = E = M_{\text{BH}}$ and an impact parameter b the angular momentum J in the centre-of-mass frame is

$$J = b M_{\text{BH}} / 2 \quad (\text{A.7})$$

Using equations A.1, A.5, A.7 gives the maximum impact parameter b_{max} :

$$\begin{aligned} b < b_{\text{max}} &\equiv 2r_{\text{h}}(n, M_{\text{BH}}, bM_{\text{BH}}/2) \\ &= 2r_{\text{s}} \left[1 + \left(\frac{n+2}{2}\right)^2 \right]^{-\frac{1}{n+1}} \end{aligned}$$

and thus the cross section for the formation of a black hole[111]:

$$\sigma = 4\pi r_{\text{h}}^2 = 4\pi r_{\text{s}}^2 \left[1 + \left(\frac{n+2}{2}\right)^2 \right]^{-\frac{2}{n+1}}. \quad (\text{A.8})$$

B. Blackmax Parameters

```
Number_of_simulations
5000
incoming_particle(1:pp_2:ppbar_3:ee+)
1
Center_of_mass_energy_of_incoming_particle
7000.
M_pl(GeV)
1000
definition_of_M_pl:(1:M_D_2:M_p_3:M_DL_4:put_in_by_hand)
1
if_definition==4
1.
Choose_a_case:(1:tensionless_nonrotating_2:tension_nonrotating\
_3:rotating_nonsplit_4:Lisa_two_particles_final_states)
3
number_of_extra_dimensions
7
number_of_splitting_dimensions
0
size_of_brane(1/Mpl)
0.0
extradimension_size(1/Mpl)
10.
tension(parameter_of_deficit_angle:1_to_0)
1.0
choose_a_pdf_file(200_to_240_cteq6)Or_>10000_for_LHAPDF
200
Chose_events_by_center_of_mass_energy_or_by_initial_black_hole_mass\
(1:center_of_mass_2:black_hole_mass)
2
Minimum_mass(GeV)
5000
Maxmum_mass(GeV)
7000.
Include_string_ball:(1:no_2:yes)
1
String_scale(M_s)(GeV)
1000.
string_coupling(g_s)
0.4
The_minimum_mass_of_a_string_ball_or_black_hole(in_unit_Mpl)
1.
fix_time_step(1:fix_2:no)
2
time_step(1/GeV)
1.e-5
other_definition_of_cross_section(0:no_1:yoshino_2:pi*r^2_3:4pi*r^2)
2
calculate_the_cross_section_according_to\
(0:the_radius_of_initial_black_hole_1:centre_of_mass_energy)
1
calculate_angular_eigen_value(0:calculate_1:fitting_result)
0
Mass_loss_factor(0~1.0)
```

```
0.
momentum_loss_factor(0~1.0)
0.
Angular_momentum_loss_factor(0~1.0)
0.
turn_on_graviton(0:off_1:on)
1
Seed
923589541
Write_LHA_Output_Record?_0=NO_1=Yes_2=More_Detailed_output
2
L_suppression(1:none_2:delta_area_3:anular_momentum_4:delta_angular_momentum)
1
angular_momentum_suppression_factor
1
charge_suppression(1:none_2:do)
2
charge_suppression_factor
1
color_suppression_factor
20
split_fermion_width(1/Mpl)_and_location(from-15to15)(up_to_9extradimensions)
number_of_conservation
3
d,s,b,u,c,t,e,mu,tau,nu_e,nu_mu,nu_tau
1,1,1,1,1,1,0,0,0,0,0,0
1,1,1,1,1,1,-3,-3,-3,-3,-3,-3
0,0,0,0,0,0,1,1,1,1,1,1
0,0,0,0,0,0,0,0,0,0,0,0
0,0,0,0,0,0,0,0,0,0,0,0
0,0,0,0,0,0,0,0,0,0,0,0
0,0,0,0,0,0,0,0,0,0,0,0
```

Bibliography

- [1] W. N. Cottingham and D. A. Greenwood, *An Introduction to the Standard Model of Particle Physics*. Cambridge University Press, Mar., 2007.
<http://www.worldcat.org/isbn/0521852498>.
- [2] K. Nakamura and P. D. Group, “Review of Particle Physics,” *Journal of Physics G: Nuclear and Particle Physics* **37** no. 7A, (2010) 075021.
<http://stacks.iop.org/0954-3899/37/i=7A/a=075021>.
- [3] S. P. Martin, “A Supersymmetry Primer,” [arXiv:hep-ph/9709356](https://arxiv.org/abs/hep-ph/9709356).
- [4] G. Nordström, “Über die Möglichkeit, das elektromagnetische Feld und das Gravitationsfeld zu vereinigen,” *Phys. Z.* **15** (1914) 504–506.
- [5] T. Kaluza, “Zum Unitätsproblem in der Physik,” *Preuss. Akad. Wiss. Berlin* (1921) 966–972.
- [6] O. Klein, “Quantentheorie und fünfdimensionale Relativitätstheorie,” *Z. Physik* (1926) 895–906.
- [7] N. Arkani-Hamed, S. Dimopoulos, and G. R. Dvali, “The Hierarchy Problem and New Dimensions at a Millimeter,” *Phys. Lett.* **B429** (1998) 263–272,
[arXiv:hep-ph/9803315](https://arxiv.org/abs/hep-ph/9803315).
- [8] N. Arkani-Hamed, S. Dimopoulos, and G. R. Dvali, “Phenomenology, Astrophysics and Cosmology of Theories with Sub-millimeter Dimensions and TeV Scale Quantum Gravity,” *Phys. Rev.* **D59** (1999) 086004, [arXiv:hep-ph/9807344](https://arxiv.org/abs/hep-ph/9807344).
- [9] G. F. Giudice, R. Rattazzi, and J. D. Wells, “Quantum Gravity and Extra Dimensions at High-Energy Colliders,” *Nucl. Phys.* **B544** (1999) 3–38,
[arXiv:hep-ph/9811291](https://arxiv.org/abs/hep-ph/9811291).
- [10] S. B. Giddings and S. D. Thomas, “High Energy Colliders as Black Hole Factories: The End of Short Distance Physics,” *Phys. Rev.* **D65** (2002) 056010,
[arXiv:hep-ph/0106219](https://arxiv.org/abs/hep-ph/0106219).
- [11] S. Dimopoulos and G. L. Landsberg, “Black Holes at the LHC,” *Phys. Rev. Lett.* **87** (2001) 161602, [arXiv:hep-ph/0106295](https://arxiv.org/abs/hep-ph/0106295).
- [12] D. J. Kapner *et al.*, “Tests of the Gravitational Inverse-Square Law Below the Dark-Energy Length Scale,” *Phys. Rev. Lett.* **98** (2007) 021101,
[arXiv:hep-ph/0611184](https://arxiv.org/abs/hep-ph/0611184).

- [13] **CDF** Collaboration, T. Aaltonen *et al.*, “Search for Large Extra Dimensions in Final States Containing one Photon or Jet and Large Missing Transverse Energy Produced in $p\bar{p}$ Collisions at $\sqrt{s} = 1.96$ TeV,” *Phys. Rev. Lett.* **101** (2008) 181602, [arXiv:0807.3132](#) [[hep-ex](#)].
- [14] **DO** Collaboration, V. M. Abazov *et al.*, “Search for Large Extra Dimensions via Single Photon plus Missing Energy Final States at $\sqrt{s} = 1.96$ TeV,” *Phys. Rev. Lett.* **101** (2008) 011601, [arXiv:0803.2137](#) [[hep-ex](#)].
- [15] S. Ask, “Search for Extra Dimensions at LEP,” [arXiv:hep-ex/0410004](#).
- [16] C. Hanhart, J. A. Pons, D. R. Phillips, and S. Reddy, “The Likelihood of GODs’ Existence: Improving the SN1987a Constraint on the Size of Large Compact Dimensions,” *Phys. Lett.* **B509** (2001) 1–9, [arXiv:astro-ph/0102063](#).
- [17] S. Hannestad and G. Raffelt, “New Supernova Limit on Large Extra Dimensions,” *Phys. Rev. Lett.* **87** (2001) 051301, [arXiv:hep-ph/0103201](#).
- [18] S. Hannestad and G. Raffelt, “Supernova and Neutron-Star Limits on Large Extra Dimensions Reexamined,” *Phys. Rev.* **D67** (2003) 125008, [arXiv:hep-ph/0304029](#).
- [19] L. A. Anchordoqui, J. L. Feng, H. Goldberg, and A. D. Shapere, “Updated Limits on TeV-Scale Gravity from Absence of Neutrino Cosmic Ray Showers Mediated by Black Holes,” *Phys. Rev.* **D68** (2003) 104025, [arXiv:hep-ph/0307228](#).
- [20] R. C. Myers and M. J. Perry, “Black Holes in Higher Dimensional Space-Times,” *Annals of Physics* **172** no. 2, (1986) 304 – 347. <http://www.sciencedirect.com/science/article/B6WB1-4DDR4P3-10S/2/a1fbd75a303f78e920071755e7c9bd70>.
- [21] E. Eichten, I. Hinchliffe, K. Lane, and C. Quigg, “Supercollider physics,” *Rev. Mod. Phys.* **56** no. 4, (Oct, 1984) 579–707.
- [22] S. R. Coleman, J. Preskill, and F. Wilczek, “Quantum Hair on Black Holes,” *Nucl. Phys.* **B378** (1992) 175–246, [arXiv:hep-th/9201059](#).
- [23] J. Preskill, P. Schwarz, A. D. Shapere, S. Trivedi, and F. Wilczek, “Limitations on the Statistical Description of Black Holes,” *Mod. Phys. Lett.* **A6** (1991) 2353–2362.
- [24] P. Meade and L. Randall, “Black Holes and Quantum Gravity at the LHC,” *JHEP* **05** (2008) 003, [arXiv:0708.3017](#) [[hep-ph](#)].
- [25] S. Dimopoulos and G. Landsberg, “Black Holes at the Large Hadron Collider,” *Phys. Rev. Lett.* **87** no. 16, (Sep, 2001) 161602.
- [26] S. Hawking, “Particle Creation by Black Holes,” *Communications in Mathematical Physics* **43** (1975) 199–220. <http://dx.doi.org/10.1007/BF02345020>.
10.1007/BF02345020.
- [27] D.-C. Dai *et al.*, “BlackMax: A Black-Hole Event Generator with Rotation, Recoil, Split Branes and Brane Tension,” *Phys. Rev.* **D77** (2008) 076007, [arXiv:0711.3012](#) [[hep-ph](#)].

- [28] M. Casals, S. R. Dolan, P. Kanti, and E. Winstanley, “Brane Decay of a $(4+n)$ -dimensional Rotating Black Hole. III: Spin-1/2 Particles,” *JHEP* **03** (2007) 019, [arXiv:hep-th/0608193](#).
- [29] D. Ida, K. Oda, and S. C. Park, “Rotating Black Holes at Future Colliders. III: Determination of Black Hole Evolution,” *Phys. Rev.* **D73** (2006) 124022, [arXiv:hep-th/0602188](#).
- [30] M. Casals, P. Kanti, and E. Winstanley, “Brane Decay of a $(4+n)$ -dimensional Rotating Black Hole. II: Spin-1 Particles,” *JHEP* **02** (2006) 051, [arXiv:hep-th/0511163](#).
- [31] G. Duffy, C. Harris, P. Kanti, and E. Winstanley, “Brane Decay of a $(4+n)$ -dimensional Rotating Black Hole: Spin-0 Particles,” *JHEP* **09** (2005) 049, [arXiv:hep-th/0507274](#).
- [32] C. M. Harris and P. Kanti, “Hawking Radiation from a $(4+n)$ -dimensional Rotating Black Hole,” *Phys. Lett.* **B633** (2006) 106–110, [arXiv:hep-th/0503010](#).
- [33] N. Arkani-Hamed, Y. Grossman, and M. Schmaltz, “Split Fermions in Extra Dimensions and Exponentially Small Cross-Sections at Future Colliders,” *Phys. Rev.* **D61** (2000) 115004, [arXiv:hep-ph/9909411](#).
- [34] N. Kaloper and D. Kiley, “Exact Black Holes and Gravitational Shockwaves on Codimension-2 Branes,” *JHEP* **03** (2006) 077, [arXiv:hep-th/0601110](#).
- [35] J. A. Frost *et al.*, “Phenomenology of Production and Decay of Spinning Extra-Dimensional Black Holes at Hadron Colliders,” *JHEP* **10** (2009) 014, [arXiv:0904.0979 \[hep-ph\]](#).
- [36] J. D. Bekenstein and V. F. Mukhanov, “Spectroscopy of the Quantum Black Hole,” *Phys. Lett.* **B360** (1995) 7–12, [arXiv:gr-qc/9505012](#).
- [37] B. Koch, M. Bleicher, and S. Hossenfelder, “Black Hole Remnants at the LHC,” *JHEP* **10** (2005) 053, [arXiv:hep-ph/0507138](#).
- [38] H. Stoecker, “Stable TeV - Black Hole Remnants at the LHC: Discovery through Di-jet Suppression, Mono-jet Emission and a Supersonic Boom in the Quark-Gluon Plasma,” *Int. J. Mod. Phys.* **D16** (2007) 185–205, [arXiv:hep-ph/0605062](#).
- [39] F. Scardigli, “Glimpses on the Micro Black Hole Planck Phase,” [arXiv:0809.1832 \[hep-th\]](#).
- [40] T. A. Collaboration, “The ATLAS Experiment at the CERN Large Hadron Collider,” *J. Instrum.* **3** (2008) S08003. 437 p. Also published by CERN Geneva in 2010.
- [41] “ATLAS Homepage.” <http://www.atlas.ch>.
- [42] **LEP Working Group for Higgs boson searches** Collaboration, R. Barate *et al.*, “Search for the Standard Model Higgs Boson at LEP,” *Phys. Lett.* **B565** (2003) 61–75, [arXiv:hep-ex/0306033](#).

- [43] J. M. Campbell, J. W. Huston, and W. J. Stirling, “Hard Interactions of Quarks and Gluons: A Primer for LHC Physics,” *Rept. Prog. Phys.* **70** (2007) 89, arXiv:hep-ph/0611148.
- [44] A. Yamamoto, Y. Makida, R. Ruber, Y. Doi, T. Haruyama, F. Haug, H. ten Kate, M. Kawai, T. Kondo, Y. Kondo, J. Metselaar, S. Mizumaki, G. Olesen, O. Pavlov, S. Ravat, E. Sbrissa, K. Tanaka, T. Taylor, and H. Yamaoka, “The ATLAS Central Solenoid,” *Nuclear Instruments and Methods in Physics Research Section A: Accelerators, Spectrometers, Detectors and Associated Equipment* **584** no. 1, (2008) 53 – 74. <http://www.sciencedirect.com/science/article/B6TJM-4PVPVHG-2/2/7bef321f21f1d2784dbd7f62b7a025cc>.
- [45] A. Foussat, H. H. J. Kate, B. Levesy, C. Mayri, Y. Pabot, V. Petrov, M. Raymond, Z. Sun, and P. Vedrine, “Assembly Concept and Technology of the ATLAS Barrel Toroid,” *Applied Superconductivity, IEEE Transactions on* **16** no. 2, (June, 2006) 565 –569.
- [46] T. A. Collaboration, “The ATLAS Inner Detector Commissioning and Calibration,” *ArXiv e-prints* (Apr., 2010) , arXiv:1004.5293.
- [47] G. Aad *et al.*, “ATLAS Pixel Detector Electronics and Sensors,” *Journal of Instrumentation* **3** no. 07, (2008) P07007. <http://stacks.iop.org/1748-0221/3/i=07/a=P07007>.
- [48] A. Ahmad *et al.*, “The Silicon Microstrip Sensors of the ATLAS Semiconductor Tracker,” *Nuclear Instruments and Methods in Physics Research Section A: Accelerators, Spectrometers, Detectors and Associated Equipment* **578** no. 1, (2007) 98 – 118. <http://www.sciencedirect.com/science/article/B6TJM-4NMWPRH-1/2/876aef58f2c94cc682482449f54c560f>.
- [49] T. A. T. Collaboration, “The ATLAS Transition Radiation Tracker (TRT) Proportional Drift Tube: Design and Performance,” *Journal of Instrumentation* **3** no. 02, (2008) P02013. <http://stacks.iop.org/1748-0221/3/i=02/a=P02013>.
- [50] *ATLAS Liquid-Argon Calorimeter: Technical Design Report*. Technical Design Report ATLAS. CERN, Geneva, 1996.
- [51] *ATLAS Tile Calorimeter: Technical Design Report*. Technical Design Report ATLAS. CERN, Geneva, 1996.
- [52] S. Palestini, “The Muon Spectrometer of the ATLAS Experiment,” *Nuclear Physics B - Proceedings Supplements* **125** (2003) 337 – 345. <http://www.sciencedirect.com/science/article/B6TVD-4BNJNFW-26/2/164a78c9b36baf31bf492a4564855343>.
- [53] J. Wotschack, “ATLAS Muon Chamber Construction Parameters for CSC, MDT, and RPC Chambers,” Tech. Rep. ATL-MUON-PUB-2008-006. ATL-COM-MUON-2008-008, CERN, Geneva, Apr, 2008. Back-up document for the ATLAS Detector Paper.

- [54] “The TGC Parameter Book.” <https://edms.cern.ch/document/906796>.
- [55] R. Achenbach *et al.*, “The ATLAS Level-1 Calorimeter Trigger,” *Journal of Instrumentation* **3** no. 03, (2008) P03001.
<http://stacks.iop.org/1748-0221/3/i=03/a=P03001>.
- [56] P. Jenni and M. Nessi, “ATLAS Forward Detectors for Luminosity Measurement and Monitoring,” Tech. Rep. CERN-LHCC-2004-010. LHCC-I-014, CERN, Geneva, Mar, 2004.
- [57] S. van der Meer, “Calibration of the Effective Beam Height in the ISR,” Tech. Rep. CERN-ISR-PO-68-31. ISR-PO-68-31, CERN, Geneva, 1968.
- [58] W. Lampl, S. Laplace, D. Lelas, P. Loch, H. Ma, S. Menke, S. Rajagopalan, D. Rousseau, S. Snyder, and G. Unal, “Calorimeter Clustering Algorithms: Description and Performance,” Tech. Rep. ATL-LARG-PUB-2008-002. ATL-COM-LARG-2008-003, CERN, Geneva, Apr, 2008.
- [59] M. Cacciari, G. P. Salam, and G. Soyez, “The Anti- k_t Jet Clustering Algorithm,” *JHEP* **04** (2008) 063, [arXiv:0802.1189](https://arxiv.org/abs/0802.1189) [hep-ph].
- [60] M. Aharrouche *et al.*, “Measurement of the Response of the ATLAS Liquid Argon Barrel Calorimeter to Electrons at the 2004 Combined Test-Beam,” *Nuclear Instruments and Methods in Physics Research Section A: Accelerators, Spectrometers, Detectors and Associated Equipment* **614** no. 3, (2010) 400 – 432.
<http://www.sciencedirect.com/science/article/B6TJM-4Y35TDM-1/2/397a6ac1f62ad2ba22cfc4ef293b4728>.
- [61] E. Abat *et al.*, “Response and Shower Topology of 2 to 180 GeV Pions Measured with the ATLAS Barrel Calorimeter at the CERN Test-Beam and Comparison to Monte Carlo Simulations,” Tech. Rep. ATL-CAL-PUB-2010-001, CERN, Geneva, May, 2010.
- [62] “Response of the ATLAS Calorimeters to Single Isolated Hadrons Produced in Proton Proton Collisions at a Center of Mass Energy of $\sqrt{s} = 900$ GeV,” Tech. Rep. ATLAS-CONF-2010-017, CERN, Geneva, Jul, 2010.
- [63] “Properties of Jets and Inputs to Jet Reconstruction and Calibration with the ATLAS Detector Using Proton-Proton Collisions at $\sqrt{s} = 7$ TeV,” Tech. Rep. ATLAS-CONF-2010-053, CERN, Geneva, Jul, 2010.
- [64] “Jet Energy Scale and its Systematic Uncertainty for Jets Produced in Proton-Proton Collisions at $\sqrt{s} = 7$ TeV and Measured with the ATLAS Detector,” Tech. Rep. ATLAS-CONF-2010-056, CERN, Geneva, Jul, 2010.
- [65] “Jet Energy Resolution and Selection Efficiency Relative to Track Jets from In-situ Techniques with the ATLAS Detector Using Proton-Proton Collisions at a Center of Mass Energy $\sqrt{s} = 7$ TeV,” Tech. Rep. ATLAS-CONF-2010-054, CERN, Geneva, Jul, 2010.

- [66] “Data-Quality Requirements and Event Cleaning for Jets and Missing Transverse Energy Reconstruction with the ATLAS Detector in Proton-Proton Collisions at a Center-of-Mass Energy of $\sqrt{s} = 7$ TeV,” Tech. Rep. ATLAS-CONF-2010-038, CERN, Geneva, Jul, 2010.
- [67] “Electron and Photon Reconstruction and Identification in ATLAS: Expected Performance at High Energy and Results at 900 GeV,” Tech. Rep. ATLAS-CONF-2010-005, CERN, Geneva, Jun, 2010.
- [68] **ATLAS** Collaboration, “Measurement of the $W \rightarrow \ell\nu$ and $Z/\gamma^* \rightarrow \ell\ell$ Production Cross Sections in Proton-Proton Collisions at $\sqrt{s} = 7$ TeV with the ATLAS Detector,” [arXiv:1010.2130](https://arxiv.org/abs/1010.2130) [[hep-ex](https://arxiv.org/abs/1010.2130)].
- [69] “Evidence for Prompt Photon Production in p p Collisions at $\sqrt{s} = 7$ TeV with the ATLAS Detector,” Tech. Rep. ATLAS-CONF-2010-077, CERN, Geneva, Jul, 2010.
- [70] “Muon Reconstruction Performance,” Tech. Rep. ATLAS-CONF-2010-064, CERN, Geneva, Jul, 2010.
- [71] “Performance of the Missing Transverse Energy Reconstruction and Calibration in Proton-Proton Collisions at a Center-of-Mass Energy of 7 TeV with the ATLAS Detector,” Tech. Rep. ATLAS-CONF-2010-057, CERN, Geneva, Jul, 2010.
- [72] “ATLAS Level-1 Calorimeter Trigger: Timing Calibration with 2009 LHC Beam Splashes,” Tech. Rep. ATLAS-DAQ-PUB-2010-001, CERN, Geneva, Apr, 2010.
- [73] R. Achenbach *et al.*, “Testing and calibrating analogue inputs to the ATLAS level-1 calorimeter trigger,”. ATL-DAQ-PROC-2008-003.
- [74] J.-P. Seidler, “Synchronisationsstudien am ATLAS-Trigger,” diploma thesis, Universität Heidelberg, 2009.
- [75] B. Gosdzik, “Offline Comparison of TileCal Signals and Trigger Signals,” diploma thesis, Universität Heidelberg, 2007.
- [76] V. Lang, “Präzisionssynchronisierung des Level-1-Kalorimeter-Triggers am ATLAS-Experiment,” diploma thesis, Universität Heidelberg, 2010.
- [77] “Luminosity Determination Using the ATLAS Detector,” Tech. Rep. ATLAS-CONF-2010-060, CERN, Geneva, Jul, 2010.
- [78] T. L. W. Group, “Updated Luminosity Determination in pp Collisions at $\sqrt{s} = 7$ TeV using the ATLAS Detector,” Tech. Rep. ATLAS-COM-CONF-2011-034, CERN, Geneva, Feb, 2011.
- [79] S. Agostinelli *et al.*, “Geant4 – A Simulation Toolkit,” *Nuclear Instruments and Methods in Physics Research Section A: Accelerators, Spectrometers, Detectors and Associated Equipment* **506** no. 3, (2003) 250 – 303.

- [80] T. Sjostrand, S. Mrenna, and P. Z. Skands, “PYTHIA 6.4 Physics and Manual,” *JHEP* **05** (2006) 026, arXiv:hep-ph/0603175.
- [81] X. Artru and G. Mennessier, “String Model and Multiproduction,” *Nuclear Physics B* **70** no. 1, (1974) 93 – 115. <http://www.sciencedirect.com/science/article/B6TVC-473DN4P-YY/2/383ffc95149dba5aecf28b33ef456fe5>.
- [82] M. G. Bowler, “Production of Heavy Quarks in the String Model,” *Zeitschrift für Physik C Particles and Fields* **11** (1981) 169–174. <http://dx.doi.org/10.1007/BF01574001>. 10.1007/BF01574001.
- [83] B. Andersson, G. Gustafson, and B. Söderberg, “A General Model for Jet Fragmentation,” *Zeitschrift für Physik C Particles and Fields* **20** (1983) 317–329. <http://dx.doi.org/10.1007/BF01407824>. 10.1007/BF01407824.
- [84] B. Andersson, G. Gustafson, and B. Söderberg, “A Probability Measure on Parton and String States,” *Nuclear Physics B* **264** (1986) 29 – 59. <http://www.sciencedirect.com/science/article/B6TVC-472T73B-2NS/2/a3a9517dc83894bcc264d728aa29af11>.
- [85] J. Pumplin *et al.*, “New Generation of Parton Distributions with Uncertainties from Global QCD Analysis,” *JHEP* **07** (2002) 012, arXiv:hep-ph/0201195.
- [86] M. R. Whalley, D. Bourilkov, and R. C. Group, “The Les Houches Accord PDFs (LHAPDF) and Lhaglu,” arXiv:hep-ph/0508110.
- [87] G. Corcella *et al.*, “HERWIG 6.5: An Event Generator for Hadron Emission Reactions with Interfering Gluons (Including Supersymmetric Processes),” *JHEP* **01** (2001) 010, arXiv:hep-ph/0011363.
- [88] G. Marchesini and B. R. Webber, “Simulation of QCD Jets Including Soft Gluon Interference,” *Nuclear Physics B* **238** no. 1, (1984) 1 – 29. <http://www.sciencedirect.com/science/article/B6TVC-4719H0J-5N/2/0216805950dbf3b1dd69b0dc87e921cb>.
- [89] J. M. Butterworth, J. R. Forshaw, and M. H. Seymour, “Multiparton Interactions in Photoproduction at HERA,” *Z. Phys.* **C72** (1996) 637–646, arXiv:hep-ph/9601371.
- [90] M. L. Mangano, M. Moretti, F. Piccinini, R. Pittau, and A. D. Polosa, “ALPGEN, a Generator for Hard Multiparton Processes in Hadronic Collisions,” *JHEP* **07** (2003) 001, arXiv:hep-ph/0206293.
- [91] J. Alwall *et al.*, “Comparative Study of Various Algorithms for the Merging of Parton Showers and Matrix Elements in Hadronic Collisions,” *Eur. Phys. J.* **C53** (2008) 473–500, arXiv:0706.2569 [hep-ph].
- [92] S. Frixione and B. R. Webber, “Matching NLO QCD Computations and Parton Shower Simulations,” *JHEP* **06** (2002) 029, arXiv:hep-ph/0204244.

-
- [93] S. Frixione, P. Nason, and B. R. Webber, “Matching NLO QCD and Parton Showers in Heavy Flavour Production,” *JHEP* **08** (2003) 007, [arXiv:hep-ph/0305252](#).
- [94] C. M. Harris, P. Richardson, and B. R. Webber, “CHARYBDIS: A Black Hole Event Generator,” *JHEP* **08** (2003) 033, [arXiv:hep-ph/0307305](#).
- [95] D.-C. Dai *et al.*, “Manual of BlackMax, a Black-Hole Event Generator with Rotation, Recoil, Split Branes, and Brane Tension,” [arXiv:0902.3577 \[hep-ph\]](#).
- [96] M. Henke, “BlackMax 2 Implementation in ATHENA,” May, 2009.
<https://twiki.cern.ch/twiki/bin/view/AtlasProtected/BlackMaxForAtlas>.
- [97] M. Henke, “BlackMax 2 Validation.” Presentation in the ATLAS MC Workgroup, Dec, 2009.
- [98] J. Alwall *et al.*, “A Standard Format for Les Houches Event Files,” *Comput. Phys. Commun.* **176** (2007) 300–304, [arXiv:hep-ph/0609017](#).
- [99] G. Aad *et al.*, *Expected Performance of the ATLAS Experiment: Detector, Trigger and Physics*. CERN, Geneva, 2009.
- [100] G. Heuermann, “Auf der Suche nach mikroskopischen schwarzen Löchern am LHC;” diploma thesis, Universität Heidelberg, 2009.
- [101] G. Heuermann, M. Henke, V. Lendermann, and H.-C. Schultz-Coulon, “Lepton-independent Search Strategy for Semi-classical Black Holes at the LHC,” Tech. Rep. ATL-COM-PHYS-2010-252, CERN, Geneva, May, 2010.
- [102] E. Richter-Was, D. Froidevaux, and L. Poggioli, “ATLFAST 2.0 a Fast Simulation Package for ATLAS,” Tech. Rep. ATL-PHYS-98-131, CERN, Geneva, Nov, 1998.
- [103] “Measurement of Jet Production in Proton-Proton Collisions at 7 TeV center-of-mass Energy with the ATLAS Detector,” Tech. Rep. ATLAS-CONF-2010-050, CERN, Geneva, Jul, 2010.
- [104] “Measurements of Multijet Production Cross Sections in Proton-Proton Collisions at 7 TeV center-of-mass energy with the ATLAS Detector,” Tech. Rep. ATLAS-CONF-2010-084, CERN, Geneva, Oct, 2010.
- [105] D. Casadei, “Efficiency Measurement: A Bayesian Approach,” *ArXiv e-prints* (Aug, 2009) , [arXiv:0908.0130 \[physics.data-an\]](#).
- [106] A. D. Martin, W. J. Stirling, R. S. Thorne, and G. Watt, “Parton Distributions for the LHC,” *Eur. Phys. J.* **C63** (2009) 189–285, [arXiv:0901.0002 \[hep-ph\]](#).
- [107] A. Sherstnev and R. S. Thorne, “Parton Distributions for LO Generators,” *Eur. Phys. J.* **C55** (2008) 553–575, [arXiv:0711.2473 \[hep-ph\]](#).
- [108] P. M. Nadolsky *et al.*, “Implications of CTEQ Global Analysis for Collider Observables,” *Phys. Rev.* **D78** (2008) 013004, [arXiv:0802.0007 \[hep-ph\]](#).

-
- [109] “Search for new physics in multi-body final states at high invariant masses with ATLAS,” Tech. Rep. ATLAS-CONF-2010-088, CERN, Geneva, Oct, 2010.
- [110] CMS Collaboration, V. Khachatryan *et al.*, “Search for Microscopic Black Hole Signatures at the Large Hadron Collider,” *Phys. Lett.* **B697** (2011) 434–453, [arXiv:1012.3375 \[hep-ex\]](#).
- [111] D. Ida, K. Oda, and S. C. Park, “Rotating Black Holes at Future Colliders: Greybody Factors for Brane Fields,” *Phys. Rev.* **D67** (2003) 064025, [arXiv:hep-th/0212108](#).

Danksagung

Verglichen mit einem Sportereignis, ist eine Doktorarbeit ein Marathonlauf. An dieser Stelle soll den Menschen gedankt werden, die zum Gelingen beigetragen haben.

Die Idee, überhaupt diesen Lauf aufzunehmen, kam von Prof. Hans-Christian Schultz-Coulon. Ich möchte mich für die Möglichkeit bedanken, diese Doktorarbeit bei ihm durchzuführen. Seine engagierte, fundierte und ehrliche Art zu betreuen, sein Bestreben, die Arbeitsgruppe auch auf sozialer Ebene besonders zu machen, und so manches Motivationsgespräch, wenn die Beine schwer wurden, haben dazu geführt, dass die Zielgerade in einem angenehmen und inspirierenden Umfeld erreicht wurde. Auch möchte ich Prof. André Schöning für die Bereitschaft danken, als Zweitgutachter zur Verfügung zu stehen und dem Zieleinlauf beizuwohnen.

Desweiteren sei der ATLAS Kollaboration und im Speziellen der TeV-Scale Gravity Group gedankt, die als Veranstalter dieses Laufs die Grundvoraussetzung dafür geschaffen haben, diese Arbeit mit Inhalt zu füllen.

Andere Teilnehmer und Betreuer bei so einem Lauf machen ihn erst zu etwas Besonderem. Ich möchte hier die Arbeitsgruppen ATLAS, H1 und ILC am Kirchhoff-Institut für Physik erwähnen, die diese 42.195 km zum Erlebnis haben werden lassen. Unsere Trainingsgruppe ist mittlerweile leider zu groß, um alle namentlich zu nennen, daher erfolgt an dieser Stelle nur eine, zu kleine, Auswahl. Am Anfang eines Laufes ist die Streckenanalyse wichtig. Das fundierte Wissen von Victor Lendermann war hilfreich, um einen guten Start für diese Arbeit zu erwischen. Rainer Stamen ist der vielleicht wichtigste Betreuer des Teams. Er hält die Laufgruppe nicht nur mit Fachwissen und Engagement zusammen, er hat auch immer ein offenes Ohr und ein gutes Gespür für Probleme und eine angenehm ehrliche Art, die mir immer viel Spaß gemacht hat. Die Betreuung der talentierten Nachwuchsläufer Ion Stroescu, Bernd Amend, Geertje Heuermann und Heiko Laier habe ich menschlich genossen, sie hat mich aber auch fachlich weitergebracht. Thorsten Dietzsch, Eva Hennekemper, Michael Herbst, Julia Hofmann und Veit Scharf haben im Saunabüro als Mitbewohner oder regelmäßige Besucher dafür gesorgt, dass kein Meter langweilig war, und auch auf der Zielgeraden in langen Nächten noch genügend Schwung vorhanden war.

Die Verpflegungsstationen waren hervorragend besetzt mit meinen Mitbewohnern Hansi Heyderich und Desiree Rupp, die gerade in der Schlussphase dafür gesorgt haben, dass dieses Projekt nicht an Unterernährung gescheitert ist.

Es gibt Menschen, die einen beim Laufenlernen begleiten. Stellvertretend sei hier der Laufgruppe David, Mira und Tobi sowie Bene, Daniel, Maike, Stroti und Volker gedankt, die, wenn mittlerweile auch in viele verschiedene Richtungen gelaufen, im Zweifelsfall immer da sind, wenn Orientierung von Nöten ist und man wissen will, warum man eigentlich läuft.

Es gibt auch Menschen, die man erst während des Laufs kennen und schätzen lernt, und mit denen man sich vorstellen kann, noch viele Läufe zu bewältigen. Anne, Bille, Felix und Patrick, danke für Nachtwachen, Tatorte, time and again und Weltverstehensbiere.

Manch unangenehme Steigung gibt es bei so einem Lauf. Meine Schwester Suse schafft es immer wieder, dass man selbst dort noch ein Lächeln im Gesicht trägt.

Der abschließende Dank gilt meinen Eltern. Sie gaben mir die Füße zum Laufen, sowie den Charakter und Willen, diesen Marathon erfolgreich zu meistern.

Ohne Euch, und all jene, die hier zu Unrecht unerwähnt geblieben sind, wäre diese Doktorarbeit wohl nicht möglich gewesen. Was soll ich sagen, die Ziellinie liegt vor mir, es ist fast geschafft, Danke.